ISBN 91-628-3187-9

LUNFD6/(NFFL-7160)1998

Luminosity Measurement for the 1995 Z^0 scan with the Very Small Angle Tagger of DELPHI

September 10, 1998

Thesis Submitted for the Degree of
Filosofie Licentiat
by

Christina Jarlskog
Physics Department
Lund University
Sweden

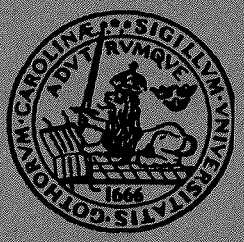

ERRATA

- page 22, (3.10) instead of (3.13), (3.11) instead of (3.14), (3.6) instead of (3.9), (3.7) instead of (3.10), (3.9) instead of (3.12).
- page 26, (3.19) instead of (3.22), (3.22) instead of (3.25).
- page 35, footnote: 20 GeV
- page 58, Table 7.1:

Pull	2.59	-2.15	0.41	-0.05

ISBN 91-628-3187-9

LUNFD6/(NFFL-7160)1998

Luminosity Measurement for the 1995 Z^0 scan with the Very Small Angle Tagger of DELPHI

September 10, 1998

Thesis Submitted for the Degree of
Filosofie Licentiat
by

Christina Jarlskog
Physics Department
Lund University
Sweden

To my parents,
Varvara and Petros

Contents

Abstract

This report presents analysis of LEP1 data from the Very Small Angle Tagger (VSAT) of the DELPHI detector at LEP. The VSAT is an electromagnetic sampling calorimeter consisting of four modules placed symmetrically at 7.7 m from the DELPHI origin. The process under study is Bhabha scattering at small polar angles (5-7 mrad). We discuss the beam parameter analysis for the 1995 Z^0 scan data. The detector simulation procedure is described in connection with the relative luminosity determination for the same period. The application of this measurement to the extraction of the hadronic lineshape parameters of the Z^0 particle is also presented.

Preface

In this report, we describe the analysis of data from the DELPHI VSAT detector at Z^0 energies with the purpose to obtain beam parameter information and the relative luminosity measurement that is used for the lineshape studies. The organisation of the report is as follows:

Chapter 1 contains a general description of the LEP ring and the components of the DELPHI detector with emphasis put on the VSAT detector.

Chapter 2 gives a short discussion on obtaining online and offline luminosity while chapter 3 discusses the theoretical fundamentals of the process used for the latter measurement, i.e. the Bhabha scattering.

Chapter 4 describes the offline procedure for collecting Bhabha events. Energy measurement, background subtraction, acceptance cuts and removal of corrupted events for 1995 scan data are discussed in detail.

Chapter 5 deals with the determination of beam parameters such as beamspot and acollinearity through the dependence of the detector's measures on those parameters.

Chapter 6 describes the detector simulation and the correction of the cross section due to beam parameter variations in terms of quantities directly measured by the detector.

Finally, in chapter 7, we combine the Bhabha sample obtained in chapter 4 with the cross section corrections derived in chapter 6 to calculate the integrated relative luminosity for the 1995 scan data taking. This result is then used for the DELPHI precision measurement of the Z^0 resonance parameters, which is described in Appendix A.

Chapter 1

LEP and DELPHI

1.1 The Large Electron-Positron storage ring

LEP started to operate in August 1989 and it is the largest accelerator yet built. It accelerates electrons and positrons in opposite directions in a vacuum pipe inside a retaining ring of magnets, before inducing them to collide head-on. Four detectors have been constructed to study the products of these collisions: ALEPH, L3, OPAL and DELPHI.

1.1.1 The beginning of LEP

The early development of the LEP ring can be highlighted by the following extracts of Sir John Adams' Annual Reports to the CERN Council in 1979 and 1980 [1]:

'Studies of the design of the LEP machines started at CERN in 1976 and the first practical design was published in 1978. This machine had a cost-optimized energy of 70 GeV per beam and measured 22 km in circumference. After extensive discussions during the autumn of 1978 it was decided to embark on the design of a somewhat larger machine, 30 km in circumference, with a cost-optimized energy of about 90 GeV per beam. The energy of both these machines could be extended, by using superconducting RF cavities, when these become available, to 100 and 130 GeV respectively.'

'Studies of the 30 km machine were completed during 1979 and a design report was issued in August.... The basic feature of the present LEP design is a large machine circumference in which the machine will be installed in stages corresponding to the new physics events that are predicted by the unified theory of weak and electromagnetic interactions. The first predicted event is the ... Z^0 at an energy of 90 GeV. Since these bosons can be produced singly, the LEP machine energy is about 50 GeV per beam, giving 100 GeV in the centre of mass. The next predicted event is the production of pairs of the charged intermediate bosons (W^+W^-) at an energy of about 180 GeV which requires LEP energies of about 90 GeV per beam.... The latest development of the LEP Project is to use the PS and SPS machines as the injectors for LEP.'

1.1.2 The tunnel

The most impressive part of the collider is the 26.67 km Main Ring tunnel. The remainder of the underground structure consists of the four experimental caverns, 18 pits, 3 km of secondary tunnel, and some 60 chambers and alcoves. The plane of the tunnel has been inclined by 1.4 % so that all underground caverns and the main part of the tunnel would be located in solid rock.

The guidance of the tunnelling machines on their desired trajectory was performed with a precision of about 1 cm and the alignment of the collider components within the LEP tunnel was done to a short-range relative precision of less than about 0.1 mm. The first precise measurements with beams indicated that the LEP circumference was in fact more than twice as precise as predicted: better than 1 cm in 26.67 km.

1.1.3 The magnet and power-converter systems

The electromagnetic guide field system of LEP consists of dipoles, quadrupoles, sextupoles, horizontal and vertical dipole correctors, rotated quadrupoles, and finally electrostatic dipole deflectors. About three quarters of the LEP circumference is occupied by 'standard cells'. Each of the eight arcs composing the ring contains 31 of these standard cells, which are comprised of magnets in the following order: a defocusing quadrupole, a vertical orbit corrector, a group of six bending dipoles, a focusing sextupole, a focusing quadrupole, a horizontal orbit corrector, a second group of six bending dipoles, and finally a defocusing sextupole. The length of a standard cell is 79.11 m.

The electrons and positrons are bent in a piecewise circular trajectory by the strings of dipole magnets. The bending field of these dipoles has been made unusually low (about 0.1 T) so as to increase the bending radius and thereby reduce the amount of synchrotron radiation. The quadrupole magnets, which produce fields linear with the transverse position, act as magnetic lenses and focus the beam to be comfortably contained within the vacuum chamber. The alternating polarity of the quadrupoles in the standard cells produces alternating-gradient focusing or 'strong' focusing. The cell sextupoles produce a field which is quadratic in transverse displacement, and they are used to compensate the dependence of the focusing strength on the beam energy ('chromaticity'). The small horizontal and vertical correctors are individually powered so as to allow 'steering' of the beam through the centre of the LEP aperture.

Each experimental collision point in LEP is surrounded by a large solenoidal magnet used for particle identification. The bunches of each beam must be tightly focused ('squeezed') to very small dimensions in the centre of these detectors in order to increase the luminosity or particle production rate. This is accomplished by a set of superconducting quadrupoles with very strong field gradients that focus the transverse beam dimensions to about 10 μm and 250 μm in the vertical and horizontal planes respectively. The solenoidal detector magnets produce another effect, however: they cause the horizontal oscillations to be 'coupled' into the vertical plane; if this were uncompensated it would greatly increase the vertical beam size and cause a reduction in the luminosity. For this reason, rotated quadrupoles are installed around each solenoid to compensate this magnetic coupling. These quadrupoles are similar to conventional quadrupoles but rotated about their axis by 45 degrees.

The strengths of all magnets in the LEP ring are very accurately adjusted by controlling the current flowing in their coils. This is accomplished by the use of more than 750 precisely stabilized d.c. power supplies ranging from less than 1 kW to a maximum of 7 MW. The specifications for these power supplies are extremely tight, both in their individual operation and, during energy ramping, in their precise synchronization. For the main dipole and quadrupole supplies, absolute accuracies down to 2 parts in 10^5 have been achieved with a resolution typically three times better.

Each magnet has its own cooling circuit. For the majority, the cooling is provided by demineralized water circuits, which are connected to a total of 10 cooling towers with a capacity of 10 MW each. Some of the small corrector magnets are air-cooled, whilst the superconducting quadrupoles and the superconducting experimental solenoids are cooled by liquid helium at 4.2 K from the cryogenics installation.

1.1.4 The acceleration system

The RF acceleration system installed at present includes 128 five-cell copper cavities powered by sixteen 1 MW klystrons via a complex of waveguides and circulators. Each accelerating cavity is coupled to a spherical low-loss storage cavity in such a way that the electromagnetic power continuously oscillates between the two sets of cavities. The coupling is arranged so that the power is at its peak in the acceleration cavities at the instant of the passage of the beam bunches. In this way, the bunches receive the maximum possible accelerating gradient, but the power loss due to heating of the copper cavity walls is greatly reduced since the electromagnetic power spends half of its time in the very-low-loss storage cavities. The operating frequency is 352.21 MHz, which corresponds to 31,320 times the revolution frequency of a beam circulating in LEP. The present system allows for a peak RF voltage of 400 MV per revolution.

The sinusoidal electric field that is generated in each accelerating cavity cell produces a 'potential well', inside which each particle of each bunch can perform stable oscillations with respect to the particle at the centre of the bunch, i.e. the synchronous particle. These oscillations are around the energy of the synchronous particle and, in azimuthal distance, ahead of or behind this particle. When represented in a phase-plane plot of normalized energy as a function of normalized distance, the trajectories form circles for the case of small oscillation amplitudes while the maximum stable oscillation possible inside

the potential well forms a closed contour (the RF bucket). There can possibly be as many synchronous particles and hence stable regions (buckets) as there are RF oscillations in the revolution time of LEP. As previously stated, this means a total of 31,320 buckets for LEP, with the possibility of stable oscillations in each. However, in order that the e^+e^- bunches collide at the centres of the experimental detectors, they must be injected and accumulated in precisely the correct buckets. This is achieved by a very precise synchronization system between the RF systems of LEP and its injector, the SPS.

1.1.5 The beam instrumentation

The LEP beam instrumentation system is used to observe the position, shape, or other relevant properties (such as polarization or electrical current) of the beam. A simple way to observe the beam is by placing a monitor directly in the path of the primary beam: an example of this is the luminescent screen that is used to observe the position and shape of the injected beam. The beam particles interact with the chromium in the screen and produce a luminescent image of the cross section of the beam which is transmitted as a television signal to the control room. The beam electrical current is measured in LEP as in other accelerators by current transformers placed around the vacuum chamber. These transformers are capable of measuring the current of a single injection or of a steady circulating beam. In the latter case the beam lifetime can be evaluated by accurate measurement of the current as a function of time.

When charged particles are bent in a circular trajectory they radiate photons. Consequently, the beams can be 'seen' by measuring this flux in the ultraviolet (UV) frequency range. Four UV monitors are used in LEP to measure the transverse dimensions of both beams at two different locations. The images are transmitted to the control room to give a real-time view of the beam, while the digital signals are processed to provide numerical values for the beam sizes.

The synchrotron radiation results in another problem: background originating from the high-energy spectrum of the photon emissions. In order to reduce this background, collimators are installed around each experimental point. Each of these collimators consists of remotely movable jaws of tungsten and copper, which can intercept and absorb the high-energy photons. Since these collimators can be placed very close to the beam, they were designed to accommodate, inside each horizontal jaw, a mini-calorimeter consisting of tungsten absorbers and silicon detectors. These mini-calorimeters are used to measure the relative luminosity in each experimental point by counting the number of Bhabha events at very small angles to the beam trajectory. In addition, other collimators are located far from all the experiments: these define the LEP aperture and remove any beam halo that might otherwise end up in one of the detectors. The system of collimators has proved invaluable in LEP and has resulted in low background conditions in the detectors practically from the first physics run.

1.1.6 The vacuum system

The duration of a typical operation to fill LEP with particles for a physics run is 12 hours. During this time each of the 10^{12} particles in the beams will have traversed the complete 26.67 km of the LEP vacuum chamber about 500 million times. In order to minimize particle losses due to collisions with residual gas molecules, the whole vacuum chamber must be pumped down to very low pressures. The achieved static pressure for LEP is $8 \cdot 10^{-12}$ *Torr* whereas in the presence of beam the pressure rises to about 10^{-9} *Torr*. This pressure rise is due to gas desorption from the inner vacuum-chamber wall, provoked by the synchrotron radiation of the circulating beam.

The two main components of the vacuum system are the vacuum chamber itself and the pumping system. Of the 27 km of LEP vacuum chamber, a length of about 22 km passes through the dipole and quadrupole magnets, and is subject to the heating due to synchrotron radiation. Although this heating represents a mere 100 W/m for phase 1, it rises to more than 2000 W/m for phase 2. Therefore the chambers need water-cooling channels and are constructed from aluminium because of its good thermal conductivity. However, only about half the radiated power would be absorbed by the aluminium; the remainder would normally escape into the tunnel, which would produce highly corrosive nitric acid in the presence of humid air. For this reason, the aluminium chamber is covered with a lead cladding of a thickness varying between 3 and 8 mm, which greatly reduces the radiation that escapes into the tunnel during operation. Other types of chambers are used in special regions such as the injection, RF, electrostatic separators, and the detector regions. For the main part these are made of stainless steel except for the detector regions where, for reasons of transparency to particles, they are fabricated from beryllium, thin-walled aluminium, or carbon-fibre composites.

For reasons of reliability the 26.7 km of the LEP vacuum system is subdivided into smaller 'vacuum sectors' with a maximum length of 474 m. During shutdown periods, when there is no circulating beam and work is often going on in the tunnel, these vacuum sectors are isolated from each other by full-aperture gate vacuum 'sector valves'. Consequently, if an accident occurs, only 474 m of vacuum will be affected and not the full 26.7 km.

1.1.7 Injectors and pre-injectors

The LEP storage ring is the last accelerator in a chain of five, each of which handles the same electrons and positrons generated on every pulse by the electron gun and the positron converter (fig. 1.1).

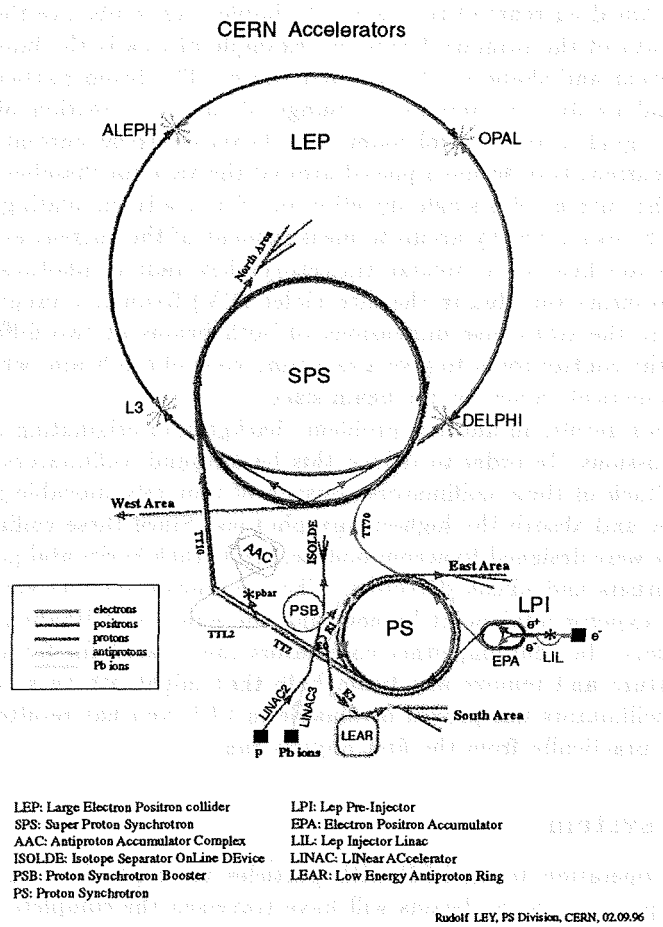

Figure 1.1: *The CERN accelerator system*

The LEP injectors consist of two linacs of 200 MeV and 600 MeV followed by a 600 MeV Electron-Positron Accumulator (EPA), which injects into the CERN Proton Synchrotron (PS) operating as a 3.5 GeV e^+e^- synchrotron. The PS then injects into the CERN Super Proton Synchrotron (SPS), which operates as a 20 GeV electron-positron injector for LEP. The decision to use the two already existing CERN proton synchrotrons (the SPS and the PS) and all the infrastructure associated with them, resulted in significant economies both in cost and in time. The PS, originally designed for 28 GeV protons and commissioned in 1959, was modified to allow acceleration of electrons and positrons from 600 MeV to 3.5 GeV. The SPS, designed to accelerate protons to 450 GeV and first brought into operation in 1976, was modified to accept electrons and positrons from the PS at 3.5 GeV, accelerate them to 20.0 GeV, and finally transfer them to the LEP collider. In order to serve LEP with electrons and positrons, both the PS and the SPS operate in multicycle mode. In this mode, a supercycle is used which incorporates four cycles of electrons/positrons followed by one cycle of protons. Consequently, owing to the fact that the electrons/positrons are accelerated in the dead-time between the proton cycles, the filling of LEP has had little or no effect on the 450 GeV SPS stationary-target physics, which runs in parallel.

1.2 The DEtector with Lepton, Photon and Hadron Identification

The electrons and positrons accelerated by LEP are allowed to meet in the center of DELPHI. This is a general purpose detector with special emphasis on particle identification, three-dimensional information and precise vertex determination. It is placed in a cavern 100 m below ground. It consists of a central cylindrical (or 'barrel') section and two end-caps (or 'forward' sections) (fig. 1.2). The radius is about 5 m and the length is over 10 m. The inner components are enclosed by a superconducting coil, providing a uniform 1.2 T magnetic field.

A description of the subdetectors is given below, where we address the components that are relevant to this analysis more extensively.

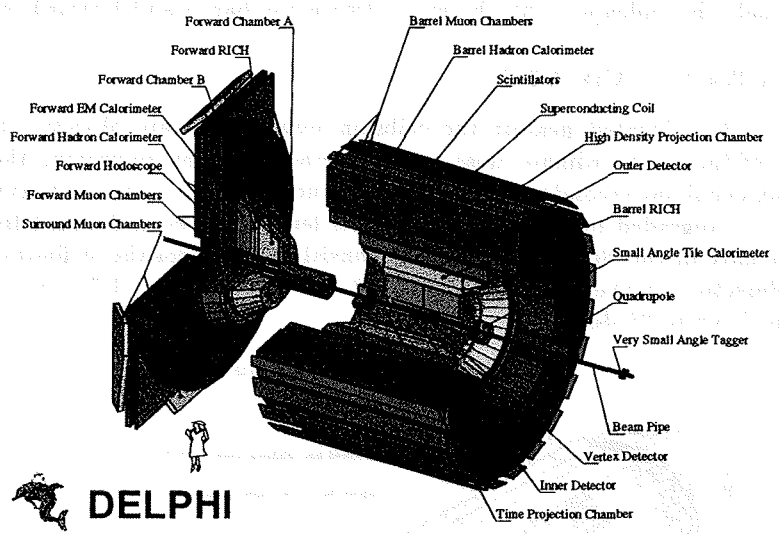

Figure 1.2: *The DELPHI detector.*

1.2.1 Tracking

Apart from the Silicon Tracker and the Time Projection Chamber, that we describe below, the tracking system of DELPHI comprises the following components:

- the Inner Detector (ID): it is shown as the smallest green cylinder in fig. 1.2. It is located between the Vertex Detector and the Time Projection Chamber and provides intermediate precision position and trigger information. It consists of two parts: the JET chamber and the Trigger Layers (TL). The JET chamber is a drift chamber subdivided into 24 sectors of 15 degrees in ϕ. It provides up to 24 $R\phi$ points per track between radii of 12 and 23 cm. The polar angle coverage extends down to 15 degrees. The TL consists of five cylindrical multiwire proportional chambers giving fast trigger information and z-information for charged tracks. The JET chamber accuracy is of the order 40 μm in $R\phi$ and 1.2 $mrad$ in ϕ.

- the Outer Detector (OD): it is shown as the narrow dark blue cylinder in fig. 1.2. It consists of 24 modules containing five layers of drift tubes located between radii of 197 and 206 cm. The active length of the detector corresponds to polar angles from 42 to 138 degrees. The detector is important for the precision of the momenta of charged particles measured by the TPC. It provides three space points plus two $R\phi$ points per track. For each tube in the detector, the drift distance of the produced electrons is derived from their drift time. All the tubes in the 3 internal layers give a z value. The precision over the measure of the $R\phi$ coordinate is 100 μm per track. The accuracy of the z measurement is of 4.4 cm. The detector is also used for trigger information. ID and OD correlated trigger data are used in order to reduce the rate due to cosmic and beam gas events.

- the Forward Chambers (FCA and FCB): the FCA is shown as the smaller blue component in the forward part in fig. 1.2. It is distant from the interaction point of about 160 cm in z. It provides

tracking and trigger information at polar angles from 11 to 32 degrees and from 148 to 169 degrees. The FCB is shown as the bigger blue component in the forward part in fig. 1.2. It is a drift chamber at an average distance of 275 *cm* from the interaction point. The sensitive area of the chamber corresponds to polar angles from 11 to 36 degrees and from 144 to 169 degrees.

- the Muon Chambers (Barrel, Forward and Surrounding): they are farthest the collision point, since muons are the only charged particles that can traverse the lead and iron of both calorimeters essentially unaffected. Most muons of momenta above 2 *GeV* are expected to penetrate to the Muon Chambers. Muon identification is achieved by comparing the extrapolations of the reconstructed tracks with the hits in the Barrel (MUB, which covers polar angles from 53 to 89 degrees and from 91 to 127 degrees) and Forward (MUF, which covers polar angles from 20 to 42 degrees and from 138 to 160 degrees) muon drift chambers. In 1994 a layer of Surrounding Muon Chambers (SMC) was installed outside the endcaps to fill the gap between the barrel and forward regions.

1.2.1.1 The Silicon Tracker (VD, VFT)

The Vertex Detector (VD) is located nearest the collision point. Its main objective is to provide an accurate measurement of the $R\phi$ coordinate close to the interaction point, improving the reconstruction of the primary vertex and enabling secondary vertices reconstructions from decays of heavy quark flavours.

The old VD has been upgraded for LEP200: the barrel length has been doubled from 24 to 48 *cm* and is now the barrel part of the Silicon Tracker. It consists of tree coaxial cylindrical layers of AC coupled silicon strip detectors at average radii of 6.3, 9.0 and 10.9 *cm* (fig. 1.3). At present the polar angle coverage extends down to 25 degrees.

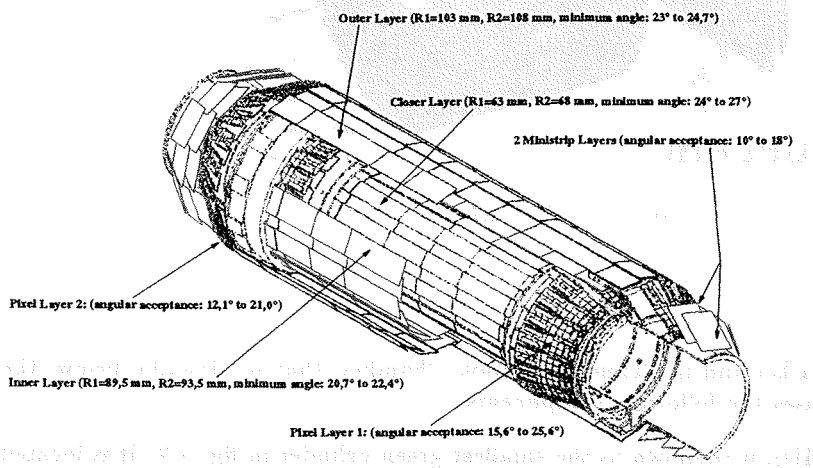

Figure 1.3: *The Silicon Tracker of DELPHI.*

The Very Forward Tracker (VFT) is located on both sides A and C of the new 1996 vertex detector. On each side it is built from two layers of mini strip and two layers of pixel detectors. It covers the polar angle from 10 to 25 degrees and from 155 to 170 degrees. The VFT is the forward part of the Silicon Tracker.

1.2.1.2 The Time Projection Chamber (TPC)

The Time Projection Chamber is shown as the big blue cylinder in fig. 1.2. It is the principal tracking device of DELPHI. It also helps in charged particle identification by measuring the dE/dX. It is a cylinder of 2x130 *cm* situated between the radii 29 *cm* and 122 *cm* (fig. 1.4). The detector provides points per particle trajectory at radii from 40 to 110 cm between polar angles from 39 to 141 degrees. At least three pad rows are crossed down to polar angles from 20 to 160 degrees.

The two drift volumes are separated by a HV (20 kVolts) plate producing an electric field of 150 $Volts/cm$. A charged particle crossing the TPC produces by ionisation around 70 electrons per cm of gas (80 % Ar and 20 % CH_4). Under the action of the electric field these primary electrons drift in the direction of the proportional chambers (6 at each TPC extremity). Each of 2x6 TPC sectors have 16 raws of pads, allowing the reconstruction of 16 space points per track. In front of the pads plates there

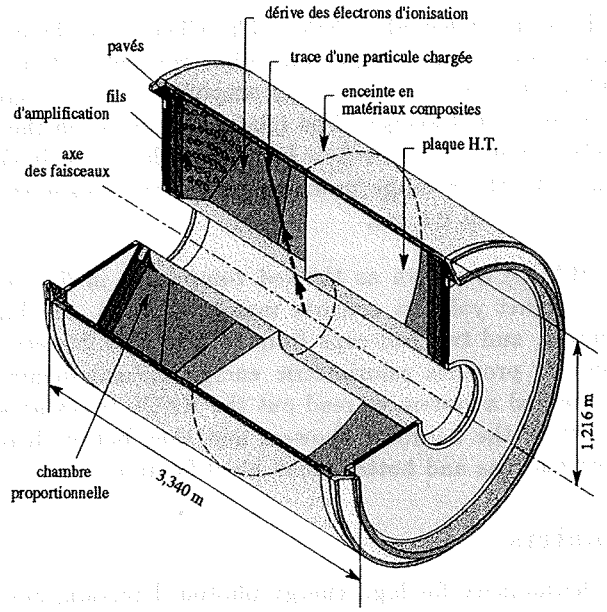

Figure 1.4: *The Time Projection Chamber of DELPHI.*

are 3 levels of grid. The one closest to the pad (the anode at a HV of 1430 Volts) contains 192 "active" wires (sensitive wires) per sector performing the dE/dx measurement.

The precision over the measure of the $R\phi$ coordinate is 250 μm per point. The accuracy of the z measurement is of 900 μm per point.

1.2.2 Electromagnetic calorimeters

Electron and photon identification is provided primarily by the electromagnetic calorimetry system. It is composed of a barrel calorimeter (HPC), a forward calorimeter (FEMC) and two very forward calorimeters, the Small angle TIle Calorimeter (STIC), which replaced the Small Angle Tagger (SAT) in April 1994, and the Very Small Angle Tagger (VSAT). The latter two are used mainly for luminosity measurements and are described in section 1.2.5.

- the High-density Projection Chamber (HPC): it is shown as the big green cylinder in fig. 1.2. Its length is 2x254 cm and it is situated between the radii 208 cm and 260 cm. The polar angle coverage is from 43 to 137 degrees. The granularity is 1 degree in ϕ, 4 mm in z and 9 samples in R. It consists of 144 independent modules, arranged in 6 rings of 24 modules each. Each HPC module is a trapezoidal box with a width ranging from 52 to 64 cm and a height of 47 cm. The length is 90 cm, except for modules in the first and last rings which are somewhat shorter. The box is filled with 41 layers of lead separated by gas gaps (8 mm each, filled with 80% argon and 20% methane). An electromagnetic particle showers in the lead and ionizes the gas. The charge drifts to one end of the box, where it is collected by a proportional chamber. The electric and magnetic fields are precisely aligned by adjusting the orientation of each box, making it possible for the ionization electrons to spiral all the way to the readout chamber. With a drift speed around 5.5 $cm/\mu s$, the maximum drift time is 16 μs. The 10th sampling gap at about 4.5 radiation lengths (shower maximum) is filled with a scintillator plane instead of gas. It is used for the first level trigger.

- the Forward ElectroMagnetic Calorimeter (FEMC): it is shown as the green disk component in the forward part in fig. 1.2. It consists of two 5 m diameter disks made of 4532 Cherenkov lead glass blocks. The front faces are placed at $z = \pm 284$ cm, covering the polar angles from 8 to 35 degrees and from 145 to 172 degrees. The operation of lead-glass Cherenkov counters is based on the collection of Cherenkov light emitted by the charged tracks of a shower. If n is the refractive index of the medium traversed by a particle and β its speed in units $c = 1$, part of the light emitted by excited atoms appears in the form of a coherent wavefront at fixed angle with respect to the trajectory $(cos(\theta) = 1/(\beta * n), \beta > 1/n)$. The pulse height is related to the number of photoelectrons knocked

out of the photocathode by the Cherenkov light. The Cherenkov signal induced by the charged particles in the shower is read out by a single stage photomultiplier designed to operate inside the DELPHI magnetic field, coupled to a low noise preamplifier. The average yield of photoelectrons is about 1000 per GeV of deposited energy. The relative precision on the measured energy can be parametrised as : $\sigma(E)/E = 0.03 + (0.12/\sqrt{E}) + (0.11/E)$, where E is in GeV. For neutral showers of energy larger than 2 GeV, the average precision on the reconstructed hit position in x and y projected to $z = \pm 284\ cm$ is about 0.5 cm.

The hadron calorimeter (HACL) is shown as the red component in fig. 1.2. It is a sampling gas detector incorporated in the magnet yoke (it consists mainly of iron), the barrel part covering polar angles from 42.6 to 137.4 degrees, and two end-caps from 11.2 to 48.5 degrees and from 131.5 to 168.8 degrees. The hadron calorimeter provides calorimetric energy measurements of charged and neutral hadrons. In addition is implemented a system to read out the HACL tubes as well as the pads, in order to give a more detailed picture of the hadronic showers and thus better distinction between showers caused by neutral and charged hadrons and better muon identification.

1.2.3 Scintillator counters

In order to achieve complete hermeticity for high energy photon detection, additional scintillators have been installed in the cable duct regions (between the barrel and each endcap, and between the HPC modules), the HERmeticity detectors (HER). In addition the DELPHI has in the barrel part the Time Of Flight (TOF) and in the forward part the HOrizontal Flight tagger (HOF). The scintillator counters are also fast trigger for beam events and cosmic radiation.

1.2.4 Particle identification

The identification of charged hadrons in DELPHI relies on the specific ionization energy loss per unit length (dE/dX) in the TPC and on the RICH detectors. The RICH technique is based on the detection of Cherenkov light emitted by the particle. The DELPHI RICH contains two radiators of different refractive indices. The liquid radiator is used for particle identification in the momentum range from 0.7 to 9 GeV. The gas radiator is used from 2.5 to 25 GeV. The full solid angle coverage is provided by two independent detectors, one in the endcap regions (Forward RICH), and one in the the barrel regions (Barrel RICH).

The Barrel RICH Detector (Barrel-RICH) is shown in yellow in fig. 1.2. It is located between the Time Projection Chamber and the Outer Detector. It is a 350 cm long cylinder with inner radius 123 cm and outer 197 cm, divided into two halves by a central support wall, 6.4 cm thick. It covers polar angles between 40 and 140 degrees.

The Forward RICH Detector (Forward-RICH) is shown as the yellow disk component in the forward part in fig. 1.2. It is located between 1.7 $m < |z| < 2.7\ m$ and covers polar angles between 15 and 35 degrees.

1.2.5 Luminosity measurement

At e^+e^- colliders, luminosity is measured by counting the number of events of a process with a clear experimental signature, with high statistics and with a cross section which can be calculated theoretically with high precision. This process is Bhabha scattering at small angles, which proceeds almost entirely through the exchange of a photon in the t-channel. In DELPHI there are two luminometers: the Small angle TIle Calorimeter (STIC) and the Very Small Angle Tagger (VSAT).

1.2.5.1 The Small angle TIle Calorimeter (STIC)

At the beginning of 1994 the DELPHI collaboration installed a new electromagnetic calorimeter named STIC (Small angle TIle Calorimeter) [2], [3], [4], [5] with the aim of providing a luminosity measurement with an accuracy of 0.1 % at LEP1.

The luminometer consists of two lead-scintillator cylindrical calorimeters of shashlik type, read out by wavelength-shifting fibers. These are located on either side of the interaction point at a distance of 2.2 m. They cover the angular region between 29 and 185 $mrad$ in polar angle (fig. 1.5).

Each of the calorimeters is equipped with two planes of silicon-strip detectors with which the direction of a shower can be measured. The purpose of this tracking device is to improve the rejection of off-energy

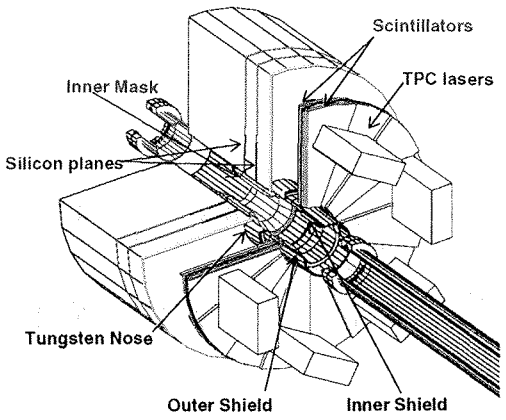

Figure 1.5: *The Small angle TIle Calorimeter.*

electron background. A veto system consisting of two layers of scintillators is mounted in front of each arm of STIC. This veto system is part of the neutral trigger. This trigger is aimed at selecting single-photon events in STIC. It provides $e-\gamma$ separation by requiring an energy deposit in one of the two STIC calorimeters in conjuction with an absence of signals in the scintillator planes in front of the calorimeters.

Several tungsten masks and shields are mounted on and near STIC. A so-called tungsten nose is mounted on the front face of the calorimeter on side C (but not on side A) and is used to define the acceptance for Bhabha electrons in luminosity measurements. A synchrotron radiation mask is mounted underneath each arm of STIC, inside the beam pipe, and these masks protect the DELPHI TPC from synchrotron radiation. Furthermore, a 'tungsten shield', mounted on the tungsten nose, provides additional radiation protection to the TPC.

Each calorimeter is divided into 10 radial rings and 16 azimuthal sectors, thus giving a total of 160 towers which point to the interaction region.

The energy resolution at 45 GeV is 3%. The spatial resolution of the calorimeter alone is 1.5 degrees in ϕ and from 300 μm to 1 mm in radius. The resolution of the silicon strips (1.7 mm pitch) over the measure of radial coordinate is 400 μm.

1.2.5.2 The Very Small Angle Tagger (VSAT)

The VSAT [6] is shown as the small green boxes in fig. 1.2. It is a sampling calorimeter consisting of four rectangular modules placed symmetrically at about 7.7 m from the DELPHI origin, around a short elliptical section of the beam pipe downstream the low beta superconducting quadrupoles (SCQ) as shown in fig. 1.6. The distance between two neighbouring modules is about 12 cm, corresponding to the smaller beam pipe dimension in that region. Since the physical process studied for the luminosity measurement is Bhabha scattering, where electrons and positrons are emitted back to back, we use the coincidences of signals between a module in the forward region and a module in the backward region, thus defining two diagonals for the trigger: diagonal 1 (modules F1-B2) and diagonal 2 (modules F2-B1).

Each VSAT module contains 12 tungsten absorbers ($X_0 = 0.38$ cm) interspaced with 12 silicon planes (Full Area Detectors, (FAD)) for energy measurement (fig. 1.7). The dimensions of the calorimeters are 3 cm in the transverse horizontal direction (x), 5 cm in the vertical direction (y) and 24 radiation lengths (about 10 cm) along the beam direction (z). The center of the electromagnetic shower is given by three silicon strip planes with 1 mm pitch placed close to the shower maximum at 5, 7 and 9 r.l.; the second plane is used for the y coordinate measurement and the other two planes for the x coordinate measurement. The angular acceptance of a module is 5-7 mrad in polar angle and $\pm$ 50 degrees in azimuth.

Due to the very small emission angle of the Bhabha events accepted in the VSAT, the accepted Bhabha cross section is very large (about 500 nb). This allows to monitor with high statistics, besides the luminosity, also the beam background and the variation of beam parameters.

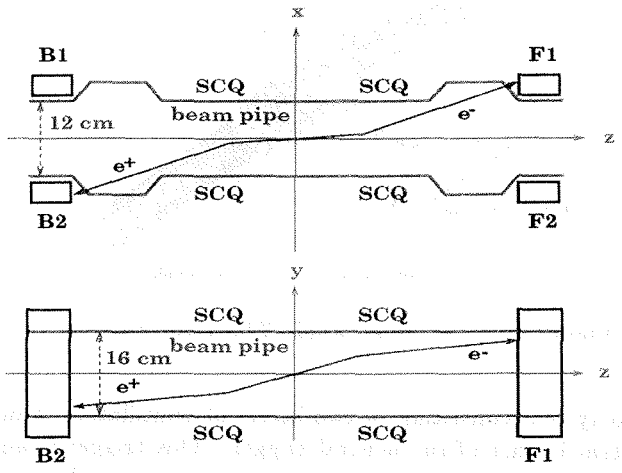

Figure 1.6: *Layout of the position of the VSAT modules in the (x,z) and (y,z) planes.*

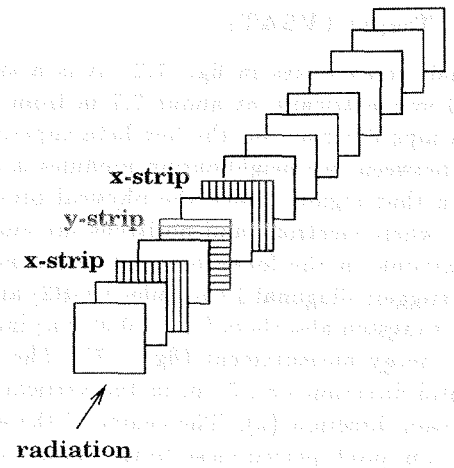

Figure 1.7: *Structure of the VSAT modules.*

Chapter 2

Luminosity

After the beam energy, the most important parameter at a colliding beam facility is the counting rate [7]. This is usually expressed by the term luminosity, which we define below. We will also discuss the expressions which allow the collider builder to know what the luminosity will be in terms of his machine parameters. Once the machine is built and operating the high energy physicist needs to know the machine luminosity in order to be able to normalize his measurements and he usually requires a more accurate value than what can be obtained directly from machine parameters. We will therefore also discuss an indirect method of measuring luminosity.

2.1 Definition of luminosity

For simplicity we first consider the interaction of a beam with a target of length l and particle number density n_2, as sketched in fig. 2.1.

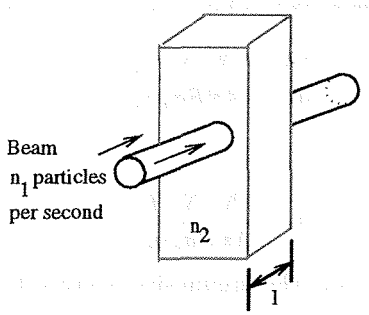

Figure 2.1: *Schematic of a particle beam of n_1 particles per second incident on a stationary target with n_2 particles per unit volume.*

The number of interactions, R, per beam particle is proportional to $n_2 \cdot l$, the total number of particles it can collide with and the constant of proportionality is defined as the cross section q for the type of interaction concerned

$$R = qn_2l$$

where q has the dimension cm^2. The transverse dimensions of the beam and target do not enter as the target is assumed to be wider than the beam. If the beam consists of n_1 particles per second, the rate of interactions will be

$$\frac{dR}{dt} = qn_1n_2l.$$

All the characteristics of the incident beam and target can be combined into a single term defined as the luminosity L by writing

$$\frac{dR}{dt} = qL \tag{2.1}$$

where $L = n_1 n_2 l$ and has the dimensions $cm^{-2}s^{-1}$. Hence luminosity is simply the interaction rate per unit cross section.

2.2 Luminosity of a single-ring collider

In a colliding beam machine the expression for L is more complicated because the target is moving and we cannot always assume that the target is wider than the beam.

We consider an electron-positron collider with $N_-, +$ particles per beam. The number of positrons one electron encounters in one turn of the machine, assuming the beams follow identical paths, is

$$\frac{q}{A} N_+$$

where q is the effective cross section of the electron and A is the cross sectional area of the beams. With N_- electrons in the beam and a revolution frequency of f, the interaction rate will be

$$\frac{dR}{dt} = \frac{q}{A} N_+ N_- f$$

If we have B bunches in each beam, the interaction rate per crossing is given by

$$\frac{dR}{dt} = \frac{N_+ N_- f q}{BA}$$

In most storage rings the transverse particle distribution is gaussian or bell shaped and since only the core of the beam contributes significantly to the luminosity we may define standard beam sizes for all kinds of particles [8]. For a gaussian particle distribution the effective beam cross section is

$$A = 4\pi\sigma_x\sigma_y$$

supposing that the beams have equal r.m.s. radii of σ_x (horizontal) and σ_y (vertical). Then

$$\frac{dR}{dt} = \frac{N_+ N_- f q}{4\pi B\sigma_x\sigma_y}$$

and the luminosity

$$L = \frac{N_+ N_- f}{4\pi B\sigma_x\sigma_y} \tag{2.2}$$

In terms of the currents, $I_{+,-} = N_{+,-} e f$, the luminosity is given by:

$$L = \frac{I_+ I_-}{4\pi e^2 B\sigma_x\sigma_y f}.$$

The transverse dimensions of the beams (σ_x and σ_y) can be expressed in terms of two machine parameters: the emittance, $\epsilon_{x,y}$, which is a measure of the area of the phase space ellipse occupied by the beam and $\beta_{x,y}$, reflecting the strength of the machine optics, through the relations

$$\sigma_{x,y} = \sqrt{\epsilon_{x,y}\beta_{x,y}}$$

$$k = \frac{\epsilon_y}{\epsilon_x}$$

where k is the coupling between the vertical and horizontal emittance. Thus

$$L = \frac{I_+ I_-}{4\pi e^2 B\sqrt{k\beta_x\beta_y}\epsilon_x f}. \tag{2.3}$$

With typical LEP conditions [9]

$$N_{+,-} = 1.3 \cdot 10^{12}$$

$$f = 11.25\ kHz$$

$$B = 4$$

$$\beta_x = 175\ cm$$

$$\beta_y = 7.5\ cm$$

$$k = 0.05$$

$$\epsilon_x = 35\ nm,$$

the LEP luminosity becomes $L \approx 10^{31}\ cm^{-2}s^{-1}$.

For a given experiment one defines also the integrated luminosity

$$\overline{L} = \int L dt$$

which depends upon the life-times of the beams, the filling time and the duration of the experiment [10].

The recipe for high luminosity is clearly to maximize the beam intensity and to minimize the beam cross section. This approach, however, is limited by two phenomena: the synchrotron radiation and the beam-beam effect.

2.2.1 Synchrotron radiation

Under the circular acceleration, an electron emits synchrotron radiation, the energy radiated per particle per turn being [11]

$$\Delta E = \frac{4\pi}{3}\frac{e^2\beta^2\gamma^4}{\rho}$$

where ρ is the bending radius, β is the particle velocity and $\gamma = (1-\beta^2)^{-1/2}$.

The loss of momentum due to the emission of photons is parallel and opposite to the direction of the particle momentum [12]. Since the particles perform betatron oscillations, the momentum loss can be split into a transverse and longitudinal component. The accelerating fields, on the other hand, provide a compensation of the lost momentum only in the longitudinal direction. In total the emission of synchrotron radiation eventually leads to a continuous loss of transverse momentum, which in turn sets a limit on the number of particles available in a bunch.

2.2.2 Beam-beam effect

The beam-beam [8] effect consists in the interaction between the beams and the electromagnetic fields created by them in the vacuum envelope. It has two consequences: first, it sets a maximum to the number of allowable particles in the bunches; second, it imposes a minimum to the beam cross section.

The limitation on the amount of beam that can be brought into collision stems from the tune shift caused by the beam-beam interation. For two counter rotating beams of particles and antiparticles there is a vertical beam-beam force of

$$F_y = -\frac{e(1+\beta^2)2\lambda}{\sigma_y(\sigma_x+\sigma_y)}y.$$

This force is attractive and therefore focusing, equivalent to that of a quadrupole of length

$$k = -\frac{F_y/y}{c^2\beta^2\gamma m}$$

causing a vertical tune shift of

$$\delta\nu_y = \frac{1}{4\pi}\int_{coll}\beta_y k ds.$$

Integrating over the collision length which is equal to half the bunch length l because colliding beams move in opposite directions, we note that the linear charge density is $\lambda = eN/B/l$, where n is the total

number of particles per beam and B the number of bunches per beam. With these replacements the beam-beam tune shift becomes finally

$$\delta\nu_y = \frac{r_0 N \beta_y}{2\pi B \sigma_y(\sigma_x + \sigma_y)},$$

where r_0 is the classical particle radius of that particle which is being disturbed. Obviously, the tune shift scales linearly with particle intensity or particle beam current and inversely with the beam cross section.

2.3 Online measurement of the luminosity

The ability to get a good estimate of the achieved luminosity at run time is essential both for the experiment and for the accelerator [13]. The VSAT detector uses the so called MIG scalers to evaluate the online luminosity [14]. For this purpose the ungated Bhabha and false Bhabha counters are used:

$$L = const \cdot (BHUNG1 - FBUNG1 + BHUNG2 - FBUNG2)$$

The constant contains information about the accepted Bhabha cross section, which varies with the running conditions. For the online luminosity, the statistical fluctuations during the short time intervals, i.e. 15 seconds, used to evaluate the trigger rate are more significant and instead an average value of the accepted cross section is used. The measurement is also normalized to the STIC online luminosity. This normalization usually has to be redone every year due to shifts in the geometry, which affect the relative accepted cross section in a non negligible way. The VSAT online luminosity is displayed together with the STIC values as a traceplot in the DELPHI control room. We give an example plot of LEP luminosity for a fill taken on 14/09/97 at 183 GeV. The accuracy of the calculation is a few percent.

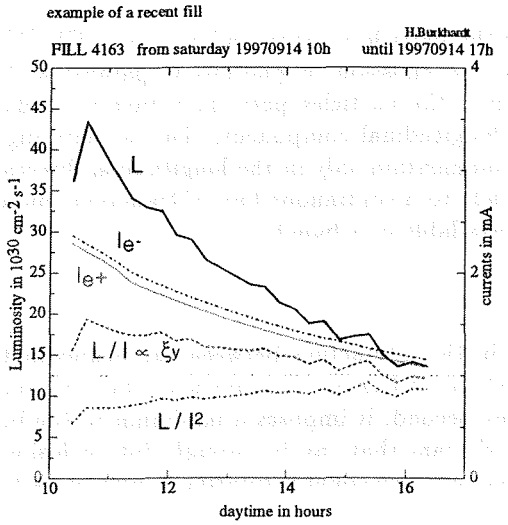

Figure 2.2: *Online luminosity for LEP. The values are averages for the four experiments.*

2.4 Offline measurement of the luminosity

In principle, eq. (2.3) implies that the luminosity is known provided the transverse beam dimensions can be measured [7]. In practice, while machine designers make use of such expressions, at an operating collider the experimenters require a more precise knowledge of the luminosity for normalization purposes and must find other means. At an electron machine the standard technique is to set up a monitor consisting of small-angle electron telescopes to observe elastic (Bhabha) scattering as in fig. 2.3.
This process has a well known cross section σ_B, so that from a measurement of the counting rate the luminosity can be determined using eq. (2.1). The cross section, σ, must of course be calculated for the acceptance of the detector

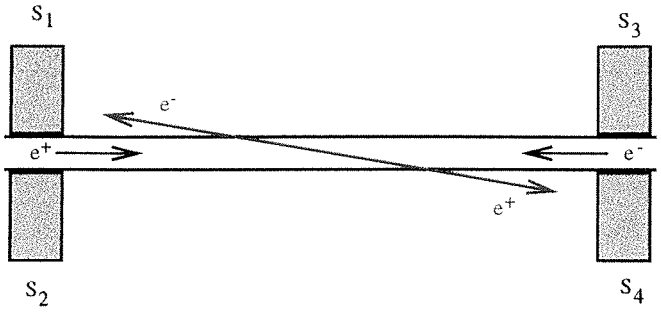

Figure 2.3: *Layout of a typical luminosity monitor to detect Bhabha scattering at electron-positron storage rings.*

$$\sigma = \int_{\theta_{min}}^{\theta_{max}} \frac{d\sigma_B}{d\Omega} d\Omega$$

where θ_{min} and θ_{max} are the minimum and maximum scattering angles accepted by the monitor. We give the expression of the cross section in the next chapter.

Chapter 3

Bhabha Scattering

By elastic Bhabha scattering [15] one means the process

$$e^+e^- \to e^+e^- \tag{3.1}$$

where only an e^+e^- pair is detected in the final state. It is a relevant process at LEP I for luminosity monitoring, line shape and $A^e_{FB} = \frac{\sigma^F - \sigma^B}{\sigma^F + \sigma^B}$ measurements, where σ^F (σ^B) is the Bhabha cross section for the production of an electron with $cos\theta > 0$ ($cos\theta < 0$) and θ is the angle of the outgoing electron with respect to the incident electron direction. In this chapter, we give a general discussion of the process including formulae for the lowest order differential cross section. The electroweak radiative corrections are briefly discussed at one-loop level. Finally, the Born cross section for very small angles is given, i.e. at the polar region covered by the VSAT.

3.1 The 'real' Bhabha scattering

Strictly speaking, the process (3.1) never occurs; as required by classical electrodynamics, a charged particle must emit, when scattered, some amount of electromagnetic radiation, so that in an actual scattering event the final state contains also photons in addition to the electron-positron pair. Such radiation effects become increasingly important as energy increases.

The electromagnetic radiation is emitted within a collinearity cone, whose opening angle shrinks as energy increases as m/E, where m is the electron mass and E its energy. At LEP, $m/E \approx 10^{-5}$ so the photons radiated by the incoming particles remain undetected within the beam pipe.

Like most of the real, detectable LEP processes, a Bhabha event can be depicted as occuring in three steps:

(i) emission of radiation from the initial particles;

(ii) the 'hard', elastic Bhabha scattering;

(iii) emission of radiation from the final particles.

For the purpose of the step (ii) above, the scattering can be considered 'hard' if the scattering angle θ is larger than the collinearity angle m/E, a condition easily fulfilled at LEP (even luminosity monitors will not go to angles less than a few mrad). In such conditions, interference effects between initial and final particles in the emission of radiation can be safely ignored. Also, due to the strong collinearity, step (ii) can be considered as occuring between particles on the mass shell.

As far as the energy-momentum of the radiation emitted in step (iii) by the final particles is not experimentally resolved from the particles themselves, the experimental results must be compared with the theoretical prediction for the process inclusive of the emission of radiation.

In the cms, all four particles involved in a fully elastic Bhabha scattering have the same energy E. Due to step (i), the laboratory is no longer the cms for step (ii) and the process is therefore initiated by particles of non equal energies E_1^0, E_2^0, both smaller than the beam energy E_b, negligable transverse momentum and non vanishing total longitudinal momentum, as in general $E_1^0 \neq E_2^0$ for any specific event. As a consequence, the final observed particles, or rather the two final electromagnetic 'jets', according to step (iii) of the process, are coplanar with the beam direction and have energies E_1, E_2 and scattering angles θ_1, θ_2 satisfying the transverse kinematical constraint

$$E_1 sin\theta_1 = -E_2 sin\theta_2 \tag{3.2}$$

but with

$$E_1 cos\theta_1 \neq -E_2 cos\theta_2. \tag{3.3}$$

As, in general, $E_1 \neq E_2$, one expects $\theta_2 \neq \pi - \theta_1$, i.e. the two particles are not back-to-back in the laboratory. The event corresponds to initial particles for step (ii) with energies

$$E_1^0 = E_1 cos^2\frac{\theta_1}{2} + E_2 sin^2\frac{\theta_2}{2} \tag{3.4}$$

$$E_2^0 = E_1 sin^2\frac{\theta_1}{2} + E_2 cos^2\frac{\theta_2}{2}. \tag{3.5}$$

E_1^0 and E_2^0 cannot be measured directly but must be inferred from E_1, E_2 through eqs. (3.4), (3.5). The probability for step (ii) to be started by particles of energy $E_i^0 = x_i E_b$, with $x_i < 1$, at a total energy squared $s_b = 4E_b^2$ can be described by a distribution $D(x_i, s_b)$, also known as the radiator, which is the same for the electron and the positron.

The observed cross section for a final electron scattered in the laboratory at an angle θ_1 for beam energy E_b can then be written, inclusively on the final electron energy, as

$$d\sigma_{obs}(E_b, \theta_1) = \int dx_1 \int dx_2 D(x_1, s_b) D(x_2, s_b) d\sigma_{lab}(E_1^0, E_2^0, \theta_1). \tag{3.6}$$

Kinematical cuts, such as, say, $E_1 > E_{min}$, are easily imposed by suitably restricting the integration regions of x_1 and x_2.

As mentioned above, in their cms the two particles have equal energies $E_1^* = E_2^* = E$ and scattering angles $\theta_1^* = \theta, \theta_2^* = \pi - \theta$. These are related to the corresponding quantities in the laboratory by

$$s = 4E_1^0 E_2^0 = 4E^2, \qquad E = \sqrt{E_1^0 E_2^0} \tag{3.7}$$

$$t = -2E_1^0 E_1 (1 - cos\theta_1) = -2E^2(1 - cos\theta) \tag{3.8}$$

$$sin^2\frac{\theta}{2} = \frac{E_1^0}{E_1^0 sin^2\frac{\theta_1}{2} + E_2^0 cos^2\frac{\theta_1}{2}} sin^2\frac{\theta_1}{2}. \tag{3.9}$$

If $\overline{|B(s,t)|^2}$ is the square invariant amplitude relevant to Bhabha scattering and s, t are given by eqs. (3.10), (3.11), the differential cross sections in the center of mass and laboratory systems can be written as

$$d\sigma_{cms}(E, \theta) = \frac{1}{8E^2}\overline{|B(s,t)|^2}\frac{dcos\theta d\phi}{8(2\pi)^2}, \tag{3.10}$$

$$d\sigma_{lab}(E_1^0, E_2^0, \theta_1) = \frac{1}{8E_1^0 E_2^0}\overline{|B(s,t)|^2}\frac{E_1^0}{E_1^0 sin^2\frac{\theta_1}{2} + E_2^0 cos^2\frac{\theta_1}{2}}\frac{dcos\theta_1 d\phi}{8(2\pi)^2}. \tag{3.11}$$

In the following, we give the relevant formulae in the standard electroweak theory for eq. (3.13). They apply directly to the observed events only as far as the energy losses of step (i) are within the experimental energy resolution; otherwise one has to use eq. (3.14), for instance in the context of eq. (3.9). E and θ can be evaluated from E_1^0, E_2^0, θ_1 by means of eqs. (3.10), (3.12).

3.2 The lowest order cross section

We give here the formulae for Bhabha scattering lowest order differential cross section on the Z_0 resonance [15]. We take as independent parameters α, M_Z, the Fermi constant, $G_F = 1.16637(2) \cdot 10^{-5}\ GeV^{-2}$ and introduce $\bar{s}_w^2$ related to them through the relation

$$\bar{s}_w^2 \equiv \frac{1}{2}\left\{1 - \left[1 - \frac{4\mu^2}{\rho M_Z^2(1-\Delta\alpha)}\right]^{\frac{1}{2}}\right\}, \tag{3.12}$$

where

$$\mu \equiv \left(\frac{\pi\alpha}{\sqrt{2}G_F}\right)^{\frac{1}{2}} = 37.281\ GeV, \tag{3.13}$$

$\Delta\alpha \simeq 0.06$ is the vacuum polarization correction and

$$\rho = \frac{1}{1-\Delta\rho}, \qquad \Delta\rho = 3\frac{G_F m_t^2}{8\pi^2\sqrt{2}}, \tag{3.14}$$

m_t being the top mass; the following combinations will also be used

$$v_e = -1 + 4\bar{s}_w^2, \qquad \alpha_e = -1, \tag{3.15}$$

$$r_V = \frac{v_e^2}{v_e^2 + \alpha_e^2}, \qquad r_A = \frac{\alpha_e^2}{v_e^2 + \alpha_e^2}. \tag{3.16}$$

The coupling of the electron to the Z_0 occurs through the form factors

$$\chi(s) = \frac{\rho M_Z^2}{16\mu^2}(v_e^2 + \alpha_e^2)\frac{s}{(s - M_Z^2 + is\Gamma_Z/M_Z)}, \tag{3.17}$$

$$\chi'(t) = \frac{\rho M_Z^2}{16\mu^2}(v_e^2 + \alpha_e^2)\frac{1}{2}\frac{s}{(M_Z^2 - t)}, \tag{3.18}$$

where the s-dependent width $\Gamma_Z(s/M_Z^2)$, rather than Γ_Z, has been introduced.

If $s = 4E^2$ and $z = cos\theta$, E and θ being the energy and the scattering angle in the cms, the lowest order differential cross section, corresponding to the graphs of fig. 3.1, can be written as

$$\frac{d\sigma_0}{d\Omega} = \sum_{i=1}^{10}\frac{d\sigma_0^{(i)}}{d\Omega}, \tag{3.19}$$

where the different channels contributions are

$$d\sigma_0^{(1)}[\gamma(s),\gamma(s)] = \left(\frac{\alpha^2}{4s}\right)(1+z^2)d\Omega; \tag{3.20}$$

$$d\sigma_0^{(2)}[\gamma(s),\gamma(t)] = \left(\frac{\alpha^2}{4s}\right)\left[-\frac{2(1+z)^2}{(1-z)}\right]d\Omega; \tag{3.21}$$

$$d\sigma_0^{(3)}[\gamma(t),\gamma(t)] = \left(\frac{\alpha^2}{4s}\right)\frac{2}{(1-z)^2}[(1+z)^2+4]d\Omega; \tag{3.22}$$

$$d\sigma_0^{(4)}[\gamma(s),Z(t)] = \left(\frac{\alpha^2}{4s}\right)[-2\chi'(t)(1+z)^2]d\Omega; \tag{3.23}$$

$$d\sigma_0^{(5)}[\gamma(t),Z(t)] = \left(\frac{\alpha^2}{4s}\right)\frac{4\chi'(t)}{(1-z)}[(1+z)^2 + 4(r_V - r_A)]d\Omega; \tag{3.24}$$

$$d\sigma_0^{(6)}[Z(t),Z(t)] = \left(\frac{\alpha^2}{4s}\right)2[\chi'(t)]^2[(1+z)^2(1+4r_V r_A) + 4(1-4r_V r_A)]d\Omega; \tag{3.25}$$

$$d\sigma_0^{(7)}[Z(s),\gamma(s)] = \left(\frac{\alpha^2}{4s}\right)2[Re\chi(s)][(1+z^2)r_V + 2zr_A]d\Omega; \tag{3.26}$$

$$d\sigma_0^{(8)}[Z(s),\gamma(t)] = \left(\frac{\alpha^2}{4s}\right)\left[-2[Re\chi(s)]\frac{(1+z)^2}{(1-z)}\right]d\Omega; \tag{3.27}$$

$$d\sigma_0^{(9)}[Z(s),Z(t)] = \left(\frac{\alpha^2}{4s}\right)[-2[Re\chi(s)]\chi'(t)(1+z)^2(1+4r_V r_A)]d\Omega; \tag{3.28}$$

$$d\sigma_0^{(10)}[Z(s),Z(s)] = \left(\frac{\alpha^2}{4s}\right)|\chi(s)|^2[(1+z^2)+8zr_V r_A]d\Omega. \tag{3.29}$$

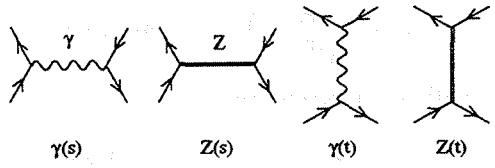

Figure 3.1: *Lowest order graphs for Bhabha scattering with their amplitudes .*

3.3 The radiative corrections

To set the terminology in a way useful to our description, we call electroweak radiative corrections the whole set of radiative corrections [15]. The one-loop corrections can then be subdivided into the following subclasses [15], [17]:

- QED corrections. They are further subdivided into
  - virtual corrections, which consist of those diagrams with an extra photon added to the Born graphs as a virtual photon loop (vertex and box diagrams). They also include the photon self energy (vacuum polarization) graphs [18]. They are depicted in fig. 3.2.
  - bremsstrahlung corrections, which consist of those diagrams with an extra photon added to the Born graphs as a real bremsstrahlung photon (fig. 3.3).
- Weak corrections, which collect all other one-loop diagrams: the subset of diagrams which involve corrections to the vector boson propagators γ, Z (fig. 3.4(a)), box diagrams with two massive boson exchange (fig. 3.4(b), (c)) and the set of vertex corrections (where the virtual photon contributions have been removed) (fig. 3.4(d), (e)). They contribute less than 1 % at most to wide angle Bhabha scattering and are negligible at small angles [20].

Due to the smallness of the electron mass the lowest order Higgs exchange diagram can be neglected. For the same reason also diagrams with Higgs - gauge boson mixing and box diagrams where one or both of the internal vector bosons of fig. 3.4 are replaced by Higgs scalars are negligible. The propagator corrections, however, involve all particles of the model, in particular the Higgs boson and the top quark, and thus depend on M_H and m_t. The vertex corrections of fig. 3.4 contain only W and Z in virtual states.

Theoretical calculations should include the complete electroweak lowest order contributions and first order radiative corrections with the Z_0 on resonance and at least most of the large higher order QED radiative corrections.

The differential cross section with first order virtual and real soft radiative corrections, including the vacuum polarization corrections, can be written as

$$\frac{d\sigma}{d\Omega} = \sum_{i=1}^{10}\frac{d\sigma_0^{(i)}}{d\Omega}(C_{infra}^{(i)} + C_F^{(i)}). \tag{3.30}$$

In the above formula, the coefficient which appears with brackets in the r.h.s. is somewhat arbitrarily split into a part C_{infra}, which depends on the soft cutoff

$$\Delta \equiv \frac{\Delta\omega}{E}, \tag{3.31}$$

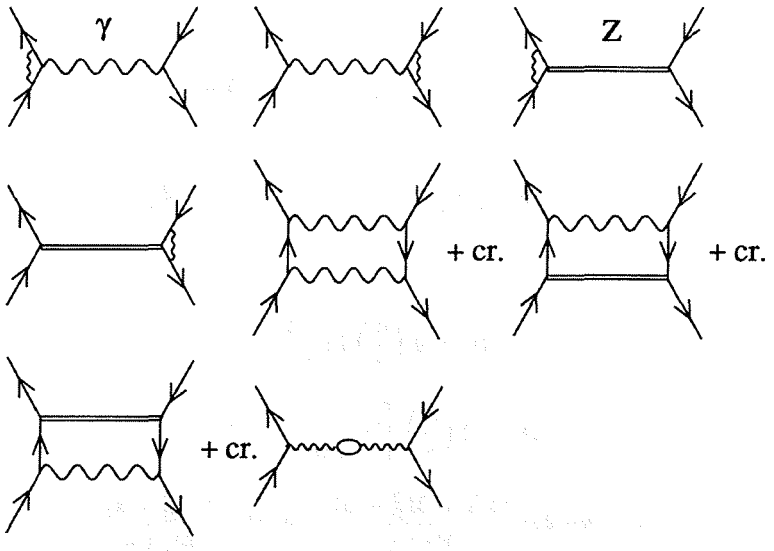

Figure 3.2: *Virtual graphs in the s channel .*

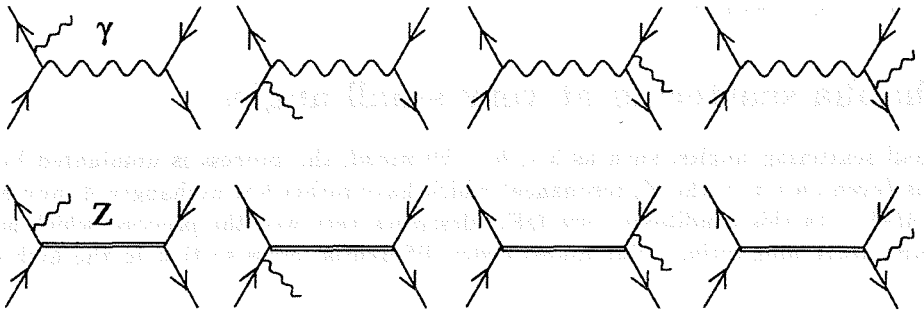

Figure 3.3: *Bremsstrahlung graphs in the s channel .*

the energy $\Delta\omega$ being the separation between the soft (undetected) and the hard (detected) radiation and a leftover part C_F. Analytical expressions for $C^{(i)}_{infra}$ and $C^{(i)}_F$ can be found in [15].

When including also the hard photons emitted collinearly to the final particles, inside a cone of half opening angle δ, one has

$$\frac{d\sigma}{d\Omega} = \sum_{i=1}^{10} \frac{d\sigma_0^{(i)}}{d\Omega}(\tilde{C}^{(i)}_{infra} + \tilde{C}^{(i)}_F). \tag{3.32}$$

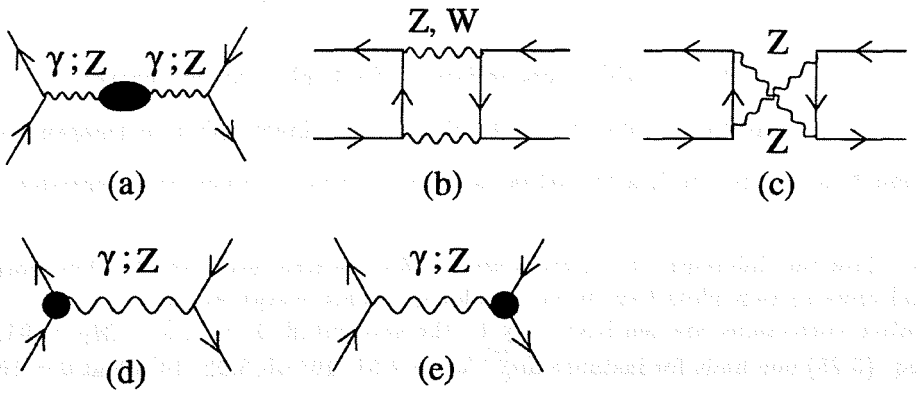

Figure 3.4: *Weak graphs in the s channel .*

At first order,

$$\tilde{C}^{(i)}_{infra} = C^{(i)}_{infra} + (\beta_\delta - \beta_e) ln\Delta \tag{3.33}$$

and

$$\tilde{C}^{(i)}_{F} = C^{(i)}_{F} + \frac{3}{4}(\beta_\delta - \beta_e) + \left(\frac{\alpha}{\pi}\right)\left(3 - \frac{2}{3}\pi^2\right) \tag{3.34}$$

where

$$\beta_\delta = 4\left(\frac{\alpha}{\pi}\right) ln\left(\frac{2}{\delta}\right), \tag{3.35}$$

$$\beta_e = 2\left(\frac{\alpha}{\pi}\right)\left[ln\left(\frac{s}{m_e^2}\right) - 1\right], \tag{3.36}$$

$$\delta = arctan\frac{(s\Delta + M_Z^2 - s)}{M_Z\Gamma_Z} - arctan\frac{(M_Z^2 - s)}{M_Z\Gamma_Z}. \tag{3.37}$$

The above formulae have been implemented in a numerical Fortran program, called bhabha.for, which can be found in the directory vxcern::disk$t3:[caffo.bhabha.bhanum] [16]. We will show distributions from the program in the next section.

3.4 Bhabha scattering at very small angles

For very small scattering angles, such as $5 < \theta < 50$ *mrad*, the process is dominated by the t-channel contributions (even on top of the Z_0 resonance) which have rather low exchanged 4-momentum ($\sqrt{-t} \approx 250 - 2500\ MeV$). In this conditions pure QED describes very well the process, which is therefore well suited for luminosity monitoring. The lowest-order differential cross section in the high-energy limit is [19]

$$d\sigma_0^{QED} = \frac{\alpha^2}{16s}\left(\frac{3+z^2}{1-z}\right)^2 d\Omega. \tag{3.38}$$

where $z = cos\theta$. For very small scattering angles the differential cross section can be simplified to

$$d\sigma_0^{QED} = \frac{4\alpha^2}{s}\frac{1}{\theta^4}d\Omega \tag{3.39}$$

showing the large forward peak, which insures a low statistical error for the measurement.

In fig. 3.5, we plot[1] the differential cross section from eq. (3.22) and eq. (3.25). We see that the γ exchange in the t channel practically coincides with the total cross section. We give the minor, non vanishing term contributions in fig. 3.8 for comparison. In fig. 3.6, we show the integrated $t-\gamma$ cross section from 5 to 7 *mrad* for the tree result (green curve) and for four corrections:

- correction 1: tree result plus first order (virtual and soft) QED radiative corrections (dark blue curve),
- correction 2: as correction 1, with exponentiation of soft photons (red curve),
- correction 3: as correction 1, plus first order final hard collinear photons (magenta curve),
- correction 4: as correction 3, with virtual, soft and hard corrections exponentiated [16] (light blue curve).

In fig. 3.7, we show the differential $t-\gamma$ cross section for the tree result and the four corrections above. All differential cross section plots have been calculated at cms energy 91.1 GeV.

The radiative corrections are sensitive only to the soft cutoff Δ; at $\sqrt{s} = M_Z = 91.1\ GeV$, in the notation of eq. (3.25) one finds for instance $d\sigma_0^{(3)}/d\theta = 2.51 \cdot 10^5\ nb, 3.92 \cdot 10^3\ nb$ at $\theta = 10, 40\ mrad$; due

[1] The plots of figs. 3.5, 3.6, 3.7 and 3.8 have been produced by bhabha.for. The VSAT-modified version of the program together with all output files can be found in the vax directory WSDE99$DKB500:[VSAT.CHRISTINA.BHABHA].

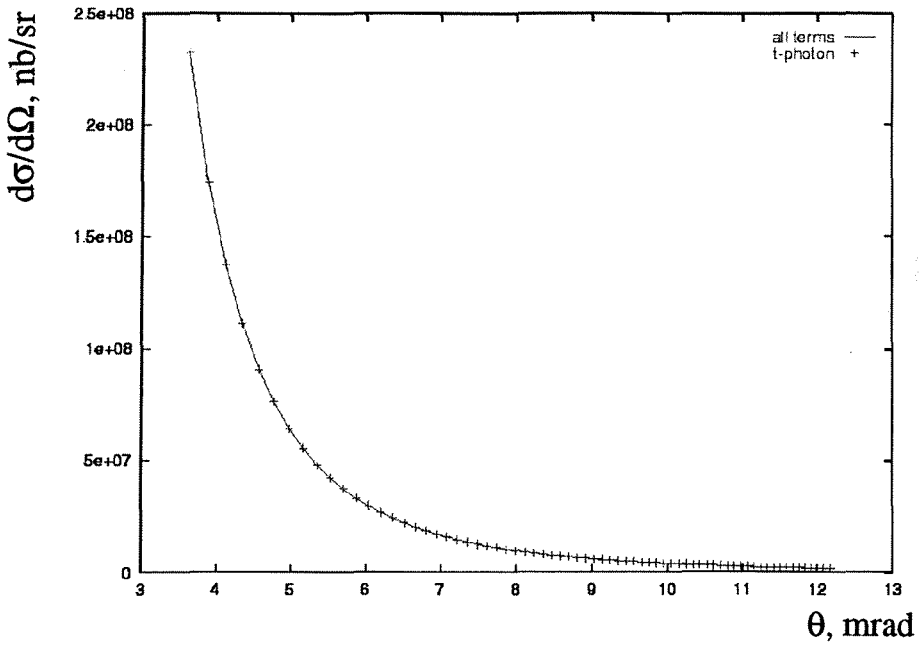

Figure 3.5: *Differential Bhabha cross section for all tree graphs and for $t-\gamma$ exchange .*

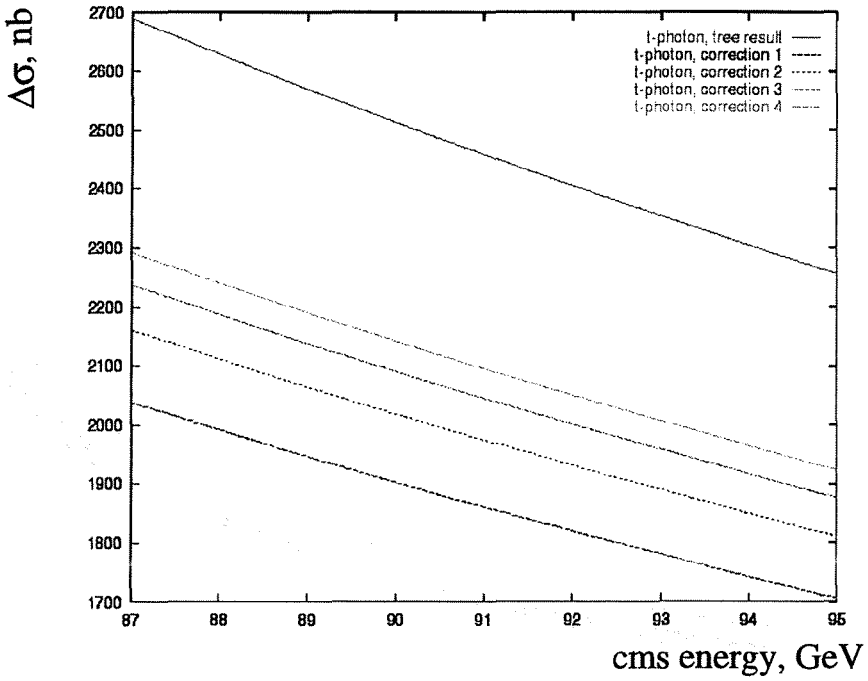

Figure 3.6: *Integrated $t-\gamma$ cross section, tree result and corrections .*

to radiative corrections, those values become $2.15 \cdot 10^5$ *nb*, $3.32 \cdot 10^3$ *nb* at $\Delta = 0.05$ and $2.26 \cdot 10^5$ *nb*, $3.54 \cdot 10^3$ *nb* at $\Delta = 0.10$.

As the scattering angle increases, the electroweak contributions become more important and at $\theta > 0.7$ *rad*, i.e. $\approx 40^0$, the dominant contribution is due to the *s*-channel Z_0 exchange. The process of this kinematical configuration is measured in the central electromagnetic calorimeter. After extraction of the less interesting *t*-channel part, it can give information on the line shape and on the $e - Z^0$ couplings (at variance with the $e^+e^- \rightarrow \mu^+\mu^-$ case, in Bhabha scattering there is a forward-backward asymmetry due to the interference between *t* and *s* channel amplitudes even in pure QED).

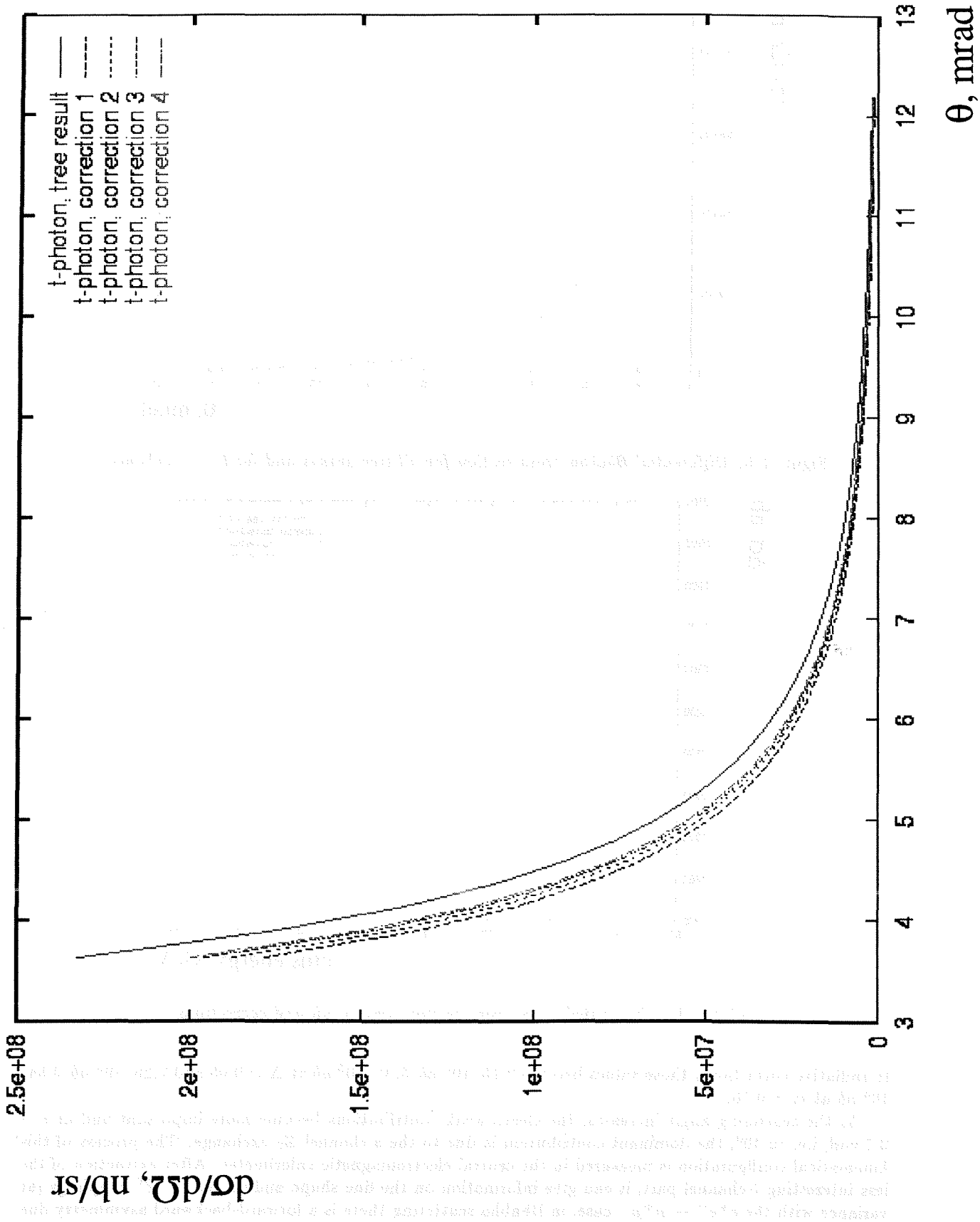

Figure 3.7: *Differential $t-\gamma$ cross section, tree result and corrections .*

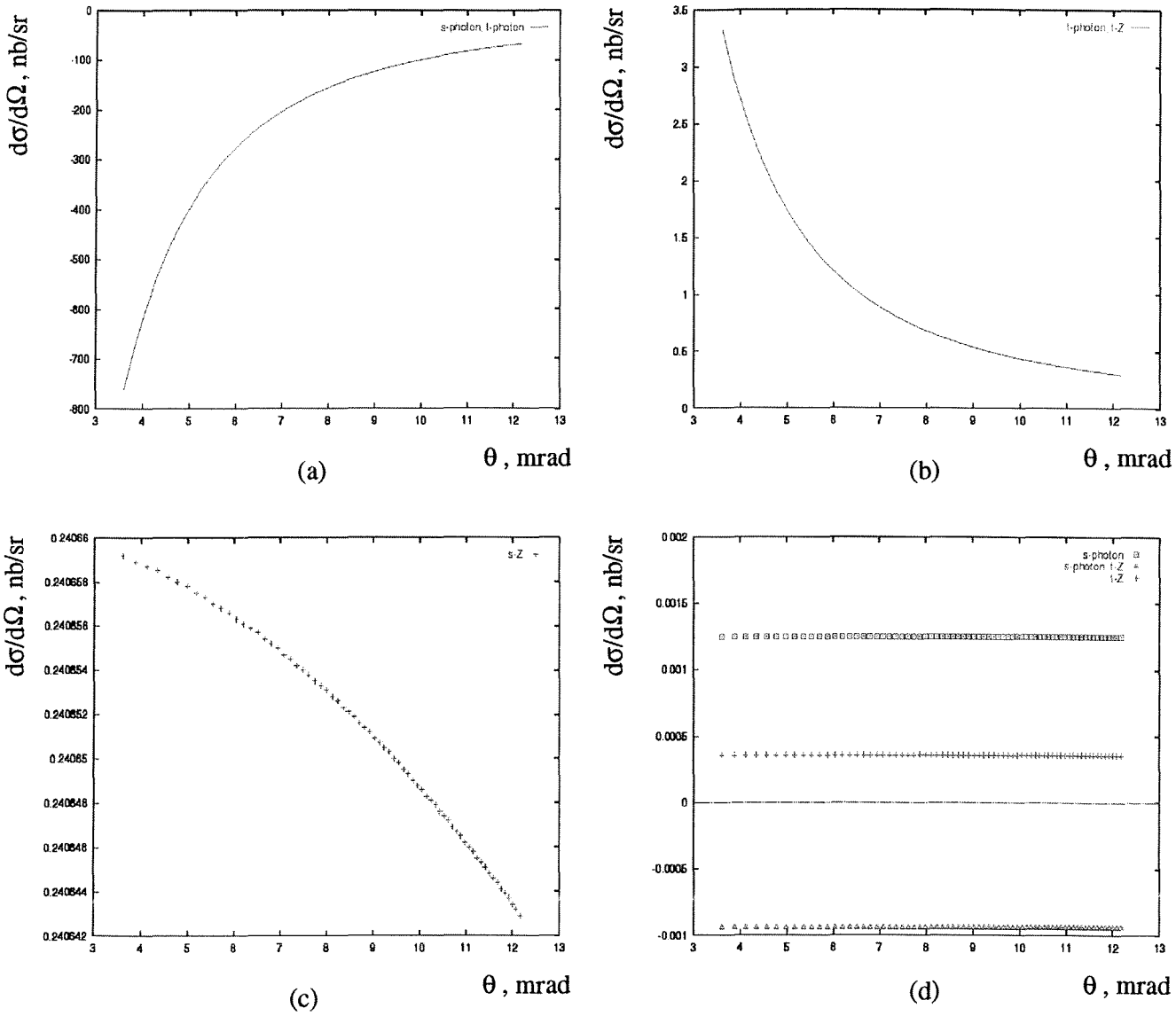

Figure 3.8: *Differential Bhabha cross section for (a) $s-\gamma$, $t-\gamma$ interference, (b) $t-\gamma$, $t-Z$ interference, (c) $s-Z$ exchange and (d) $s-\gamma$ exchange, $s-\gamma$, $t-Z$ interference and $t-Z$ exchange .*

Chapter 4

The Bhabha Measurement

In this chapter, we describe how our data are processed off-line in order to extract the Bhabha sample we need for the luminosity estimation. The procedure is the same for every year, but the additional features of the 95 scan data are also addressed here. The operation of the electronics is briefly explained as well, as its impact on the off-line analysis was of major importance.

4.1 The electronics

For the 1995 scan LEP had modified its previous mode of single bunch operation to a scheme of tightly spaced minibunch-trains, i.e. instead of having only one bunch crossing every 25 μs there were 2 to 4 minibunches within each bunch. The time separation between minibunches was a fraction of a μs. Most of the scan data taking was done with 3 minibunches separated by about 250 ns.

Each VSAT module was equipped with an independent system for reading pulse heights. This allowed for signals from different minibunches to be read in the four modules after the same beam crossing. Fig. 4.1 shows how the readout was done [21]. A fixed time (dt1) after a beam crossing (BCO), a signal from Pandora (WNG1) enables a gate generator. The width of each gate is about 50 ns. During this time a sensor is active and checks whether the sum of the FAD signals is above threshold. If this is the case, a HOLD is sent to the FADs when the gate is closed. A second HOLD is sent to the strips a fixed time later (dt2). If no signal is found above threshold during the gates, another signal from Pandora (WNG2) disables the gate generator after time dt3 and the HOLDs are generated. The minibunch number assigned to the signal is determined by the first gate during which the pulse is above threshold.

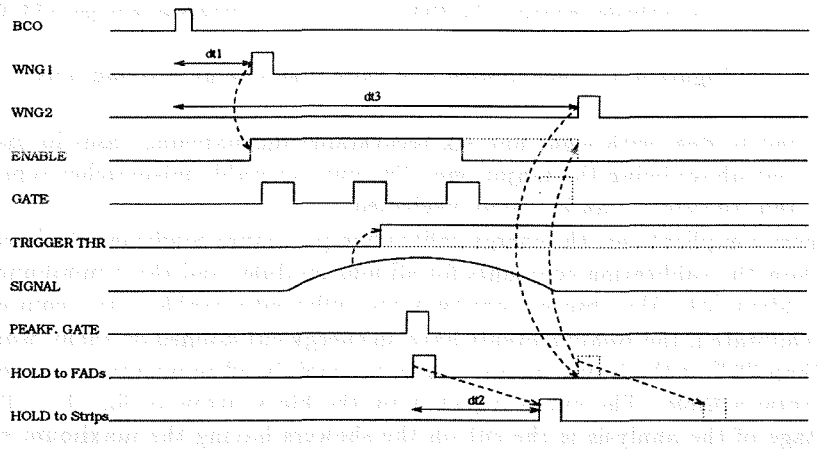

Figure 4.1: *Minibunch scheme signals when there is a hit in the module (full lines) and when there is no hit in the module (dotted lines).*

The independent operation of the modules occasionally resulted in misidentification of the minibunch number. This meant that elaborate off-line corrections had to be applied to the data both for the minibunch number recovering [22] and for the energy calibration [23].

4.2 The energy measurement

One example of mismatched event, i.e. wrong assignment of minibunch number by the electronics, is shown in fig. 4.2. The green pulse is a minibunch three electron. However, its energy is so high that the signal is already above threshold while gate G2 is open. This induces the detector to assign minibunch number two to the electron.

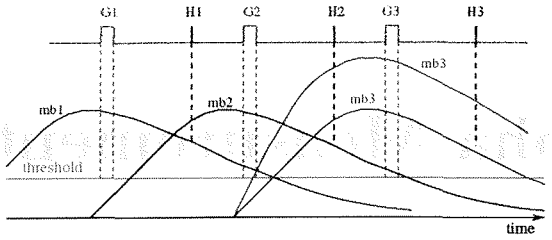

Figure 4.2: *Signals for the three minibunches and for one high energy mismatch.*

The subsequent hold H2 sees a value of the signal which is much higher than the one hold H3 would have seen. The result is that the electron, apart from having wrong minibunch number, it is also assigned an overestimated energy value. Those electrons form the green energy spectrum of fig. 4.3. The remaining minibunch three distribution (magenta curve) is manifestly missing many of its events if we compare its height with this of the minibunch one and two spectra (red and blue curves).

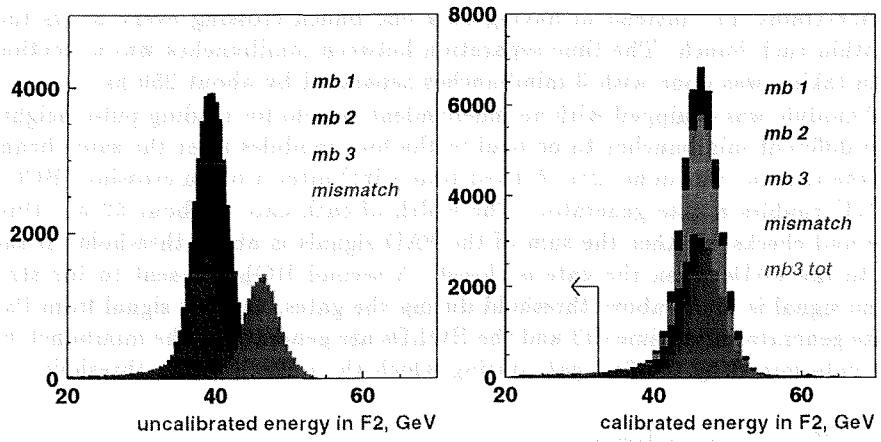

Figure 4.3: *Uncalibrated and calibrated energy distributions.*

In total, we had to deal with eight and six recoverable mismatching cases in diagonal one and two, respectively, the one above being the major one. The unrecoverable mismatches represent less than 0.1% of the data [22] and, therefore, can be safely neglected.

In spite of these complications, the energy calibration procedure confirmed the linearity of the modules. In fig. 4.4, we show the calibration constants for all four modules and three minibunches before and after the radiation accident [24]. We observe that they are sufficiently stable with beam energy.

After being calibrated, the Bhabha events have an energy cut applied on them, which removes particles that have less than 70% of the beam energy. These are mainly off-momentum electrons, representing few percent of the total sample. The cut is depicted by the black arrow in fig. 4.3. The next cut that we apply at this stage of the analysis is the cut on the showers having the maximum energy deposit in the outer x-strips of the detector as the shower may have started outside the module.

Bhabha events thus obtained have a very strong correlation in energy which can be seen in fig. 4.5 as the central aggregation of green points. This feature is considered to be their 'signature' and has played an important role in quality checking and also in the analysis (e.g. for recovering the mismatches). The plot includes also the off-momentum electrons and the radiative Bhabha events; they are the tails spreading over lower energies. The few events at very high energies are in reality pile-ups of off-momentum electrons

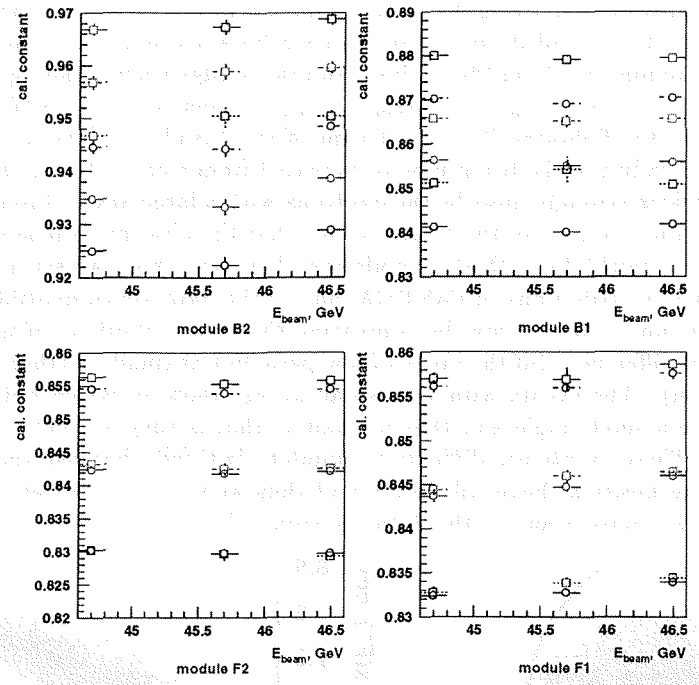

Figure 4.4: *Energy calibration constants for the four modules and minibunch one (red), minibunch two (green) and minibunch three (blue). The boxes (circles) show data before (after) the radiation accident.*

and Bhabha electrons. The reason why they are recorded as one event is that the detector did not have the time to disentangle them.

In order to complete this phase of the analysis we need to remove the accidental coincidences. They are shown as the blue circles of fig. 4.5. Their rate can be estimated and subtracted by tagging one particle in one module and one particle in the diagonal module separated in time by four beam crossings, i.e. after the same bunch has returned to the interaction point. They represent about 2% of the total background.

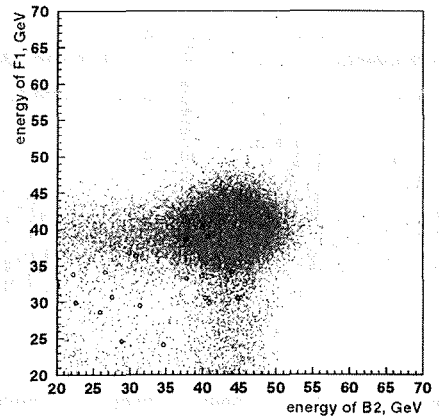

Figure 4.5: *Uncalibrated energy in diagonal 1 showing the Bhabha correlation (green blob) and the accidental Bhabha events (blue circles).*

4.3 The radial cut

After calibrating the energy and removing the background, the next step is to restrict the acceptance of the detector. This is done by the so-called radial cut, which defines a volume with outer edge corresponding to a maximum allowed radius of 7.7 *cm* (fig. 4.6(a)) and inner edge corresponding to a minimum allowed sum of the x positions ($sx = |x_{inner\ module}| + |x_{outer\ module}|$) equal to 13.2 *cm* (fig. 4.6(b)). The reason for the outer edge cut is the following [25]. Upstream of the VSAT modules (at about 6.5 *m* from the interaction point), the x radius of the beam pipe is increased from 6 *cm* to 8 *cm*. In the connection region there is a thick flange which strongly absorbs the electrons with a large angle. From the (x,y) distribution of the impact points of the electrons in the VSAT we see that the absorption is not sharp and also that it is difficult to reproduce it faithfully with the simulation. For this reason we set a cut at the value of the radius for which the (x,y) distributions of FASTSIM and of the data are compatible. A similar argument holds for the cut at the inner edge. Again, by comparing the sx distributions of simulation and data, we see that there are small differences (of the order of few permille) at small sx (there are too many Bhabha events in the simulation). The events with very small sx are those in which both the forward and the backward electron have a small angle and thus a small x, that is they are both close to the inner edge of the VSAT module. These events are difficult to simulate faithfully because they depend critically on many parameters (beam position, beam tilt, etc.) and thus we set an sx cut at the value for which the sx distributions of the simulation and of the data are compatible.

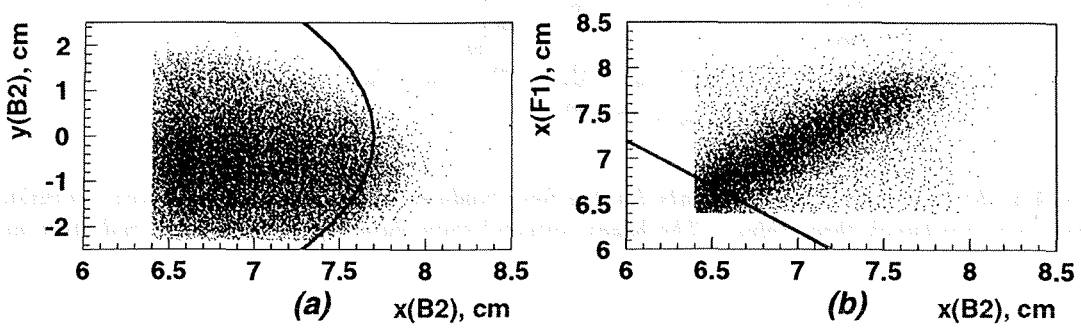

Figure 4.6: *The acceptance cuts; (a) the cut on the outer edge, (b) the cut on the inner edge of the detector.*

In fig. 4.7, we show the distributions of the number of Bhabha events per cassette for the fills of the scan. The mean value for the total volume (i.e. before applying the radial cut) is 3136 events per cassette in diagonal one and 3445 events per cassette in diagonal two. These numbers are reduced by 22% and 28%, respectively, when we apply our acceptance cut.

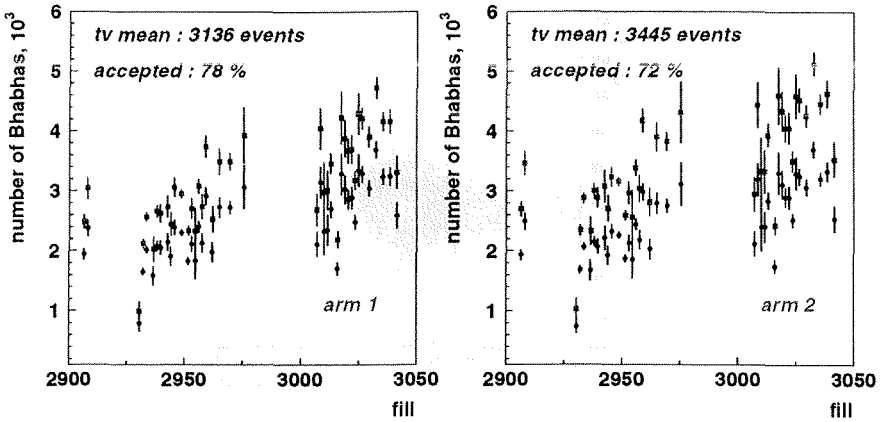

Figure 4.7: *Accepted events in the two diagonals before (red) and after (blue) the radial cut has been applied.*

4.4 Corrupted data

At this stage, we have a Bhabha sample consisting of 1200 cassettes. So far, our cuts have only restricted the number of events within each cassette, but all cassettes of the data taken have been included in the analysis. There are, however, cases where the cassettes are of bad quality and they have to be removed. In order to find out which cassettes are to be discarded we set two limits; first, the number of corrupted Bhabha triggers[1] must be less than 10% and second, the number of corrupted buffers must be less than 1 permille. The reason for applying this cut is that we correct for the corrupted events that we miss using the trigger information which is generally available even if the buffer is corrupted, but this is a correction which has a large uncertainty, so it is valid only if the fraction of corrupted data is small, otherwise it introduces an error larger than the gain in statistics we would have by including the corrupted cassettes [25].

Fig. 4.8 shows the distributions of these two variables and the positions of the cuts. In order to decide on the values of the cuts we try different combinations and we keep the one that gives us the largest number of cassettes possible without allowing the normalized differences between STIC and VSAT luminosities become too large. In total, the two cuts reject 31% of our cassettes.

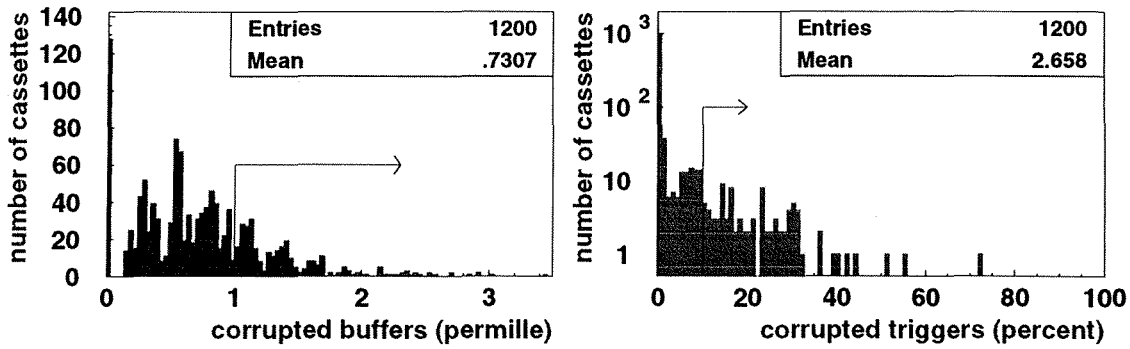

Figure 4.8: *Corrupted buffers and corrupted triggers for all scan data. The arrows show the position of the cuts.*

Fig. 4.9 shows the distributions of Bhabha events in the two diagonals (blue curves) for our final sample. The red curves show the cassettes that have been rejected because of the corrupted Bhabha trigger cut (only this cut would have removed 91 cassettes). The green curves show the cassettes that have been removed because of the corrupted buffer cut. This cut alone removes 307 cassettes. There were 25 cassettes that satisfied both cuts. We will continue the analysis of the remaining 827 cassettes in chapter 7.

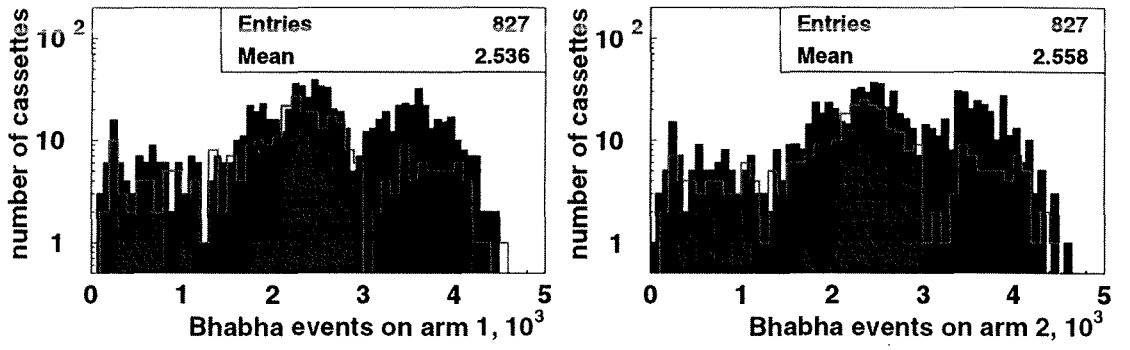

Figure 4.9: *The final Bhabha sample (blue curves). The red (green) distributions show cassettes with too many corrupted triggers (buffers).*

[1] A Bhabha trigger is a coincidence with more than 25 GeV deposited in each module.

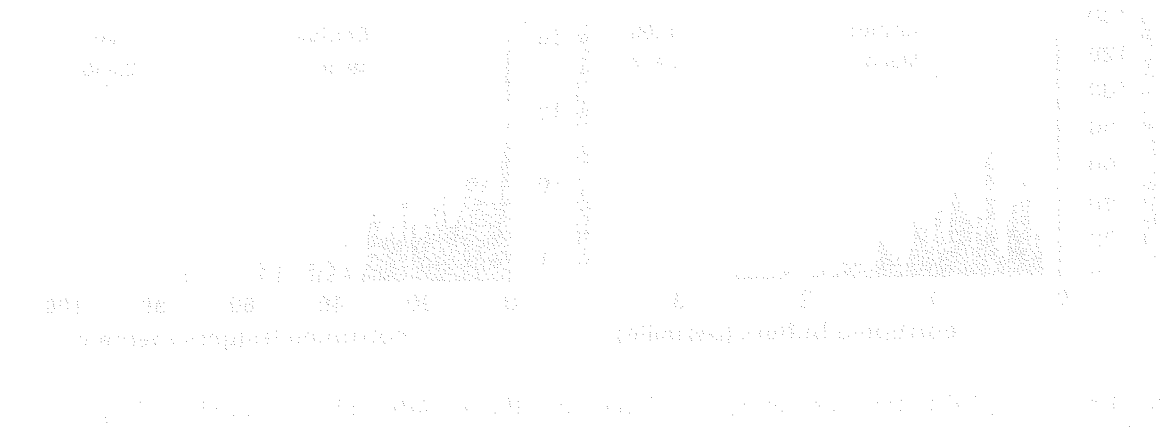

Chapter 5

Beam Parameters

Due to the large accepted Bhabha cross section the VSAT can monitor with high statistics, besides the luminosity and the beam background, the variation of beam parameters as well. In this chapter, we give the results of the beam parameter analysis for the 1995 scan data as it is relevant for the luminosity calculation we will present in chapter 7. The results for 1993 and 1994 data can be found in [26] and [6]. A detailed description of the analysis is given in [27].

5.1 Why do we monitor beam parameters?

The monitoring of the beam parameters is an important task for two reasons.

The first reason is the online cross check of similar measurements done by the general monitoring system of LEP at the DELPHI interaction point. These measurements are used in order to optimize the luminosity, which depends strongly on the beam parameters. Among the DELPHI detectors, the VSAT has the highest accepted cross section and can thus collect sufficient statistics in a time interval ($\approx$ 10 minutes) relevant for online control.

The second reason is the offline estimation of variation of beam parameters. This information is used at different levels in the analysis of DELPHI events. For example, the variations of the beamspot position as well as those of the directions of the incident particles are used to optimize the alignment of the different DELPHI detectors. Furthermore, when it comes to the luminosity measurement done by the VSAT, the beam parameter monitoring provides an important cross check: the Bhabha cross section in the VSAT acceptance depends on the beam parameters and consequently, it has to be corrected for their variations. Fortunately, as shown in [28], such corrections can be done with a high level of accuracy (better than .1%) by using directly quantities measured by the VSAT without any need to know in detail the values of the beam parameters themselves. However, since the correction function is determined by an extensive simulation of different beam conditions done by a fast Monte Carlo program (FASTSIM), it is important to cross check the validity of the model used in FASTSIM by comparing the description of the variations of the beam parameters that we obtain from VSAT data with data from LEP or other DELPHI detectors.

5.2 Beam parameters monitoring with the VSAT

The beam parameters that are relevant for the following discussion are:

- the average values of the coordinates x_b, y_b and z_b of the interaction point;
- the corresponding beam widths σ_x, σ_y and σ_z;
- the average values of the incident positron and electron beam angles at the interaction point, in the (x, z) and in the (y, z) planes (we will call them briefly *tilts*), respectively θ_+^x, θ_-^x, θ_+^y and θ_-^y;
- the beam divergence in the two planes, that is the spread around the above average angles.

The quantities measured with the VSAT which are used to extract information on the beam parameters are the x and y coordinates of the impact points of the scattered leptons in the four modules (fig. 5.1);

the angles of the outgoing particles cannot be measured, which disqualifies the detector for monitoring all the above mentioned parameters.

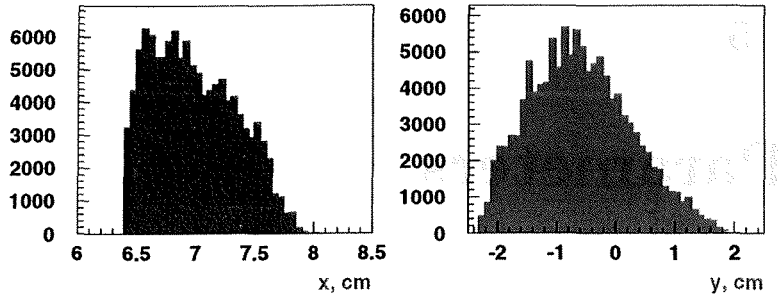

Figure 5.1: *x and y measurement for module F2, fill 3029.*

However, we can extract information on most of the beam parameters by combining the VSAT data with the beamspot measurements done by the VD and TPC. In this section, we will discuss the dependence on the beam parameters of the variables measured by the VSAT.

5.2.1 Beam parameters in the (x,z) plane

Figure 5.2 shows two Bhabha events in the (x,z) plane in the diagonals of the detector for the ideal situation in which the interaction point coincides with the nominal position ($x_b = y_b = z_b = 0$). We have assumed that the trajectories of the incoming particles are along the z-axis, so we also have zero beam tilts.

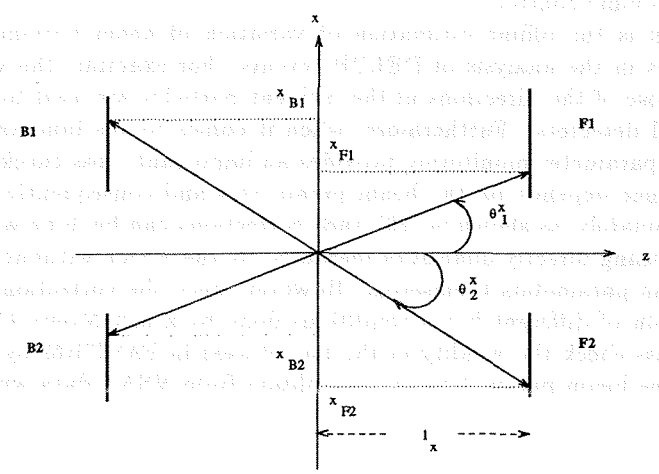

Figure 5.2: *Bhabha events on the two diagonals for zero beam displacement and zero tilts.*

In order to be able to represent the trajectories of the scattered particles as straight lines, we take into account the divergent effect of the superconducting quadrupoles (in first approximation) by moving the modules to an effective distance, l_x=12.6 m, which is assumed to be the same for all modules. The production angle of the Bhabha pair in diagonal i is denoted by θ_i^x and is defined to be always positive. Since those angles are very small we can calculate the x coordinates of the impact points of the particles on the modules as follows:

$$\begin{aligned} x_{F1} &= l_x\theta_1^x \qquad & x_{B2} &= -l_x\theta_1^x \\ x_{B1} &= l_x\theta_2^x \qquad & x_{F2} &= -l_x\theta_2^x \end{aligned} \tag{5.1}$$

However, this ideal condition is rarely the case, since the beams do not usually cross at the nominal position. Fig. 5.3 represents a more realistic situation, in which we have included a nonzero beam displacement in the x direction, x_b. The constant f_x is the amplification factor of the particle trajectories due to the superconducting quadrupoles. It is of the order of 2.1 and it is practically the same for all four modules.

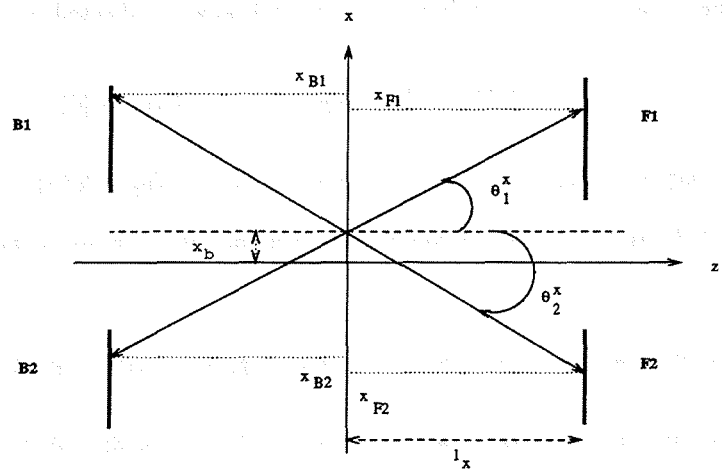

Figure 5.3: *Events on the two diagonals for zero z displacement and zero tilts.*

The emission angles are the same as in fig. 5.2, but the x coordinates of the impact points are now given by

$$x_{F1} = f_x x_b + l_x \theta_1^x \qquad x_{B2} = f_x x_b - l_x \theta_1^x$$
$$x_{B1} = f_x x_b + l_x \theta_2^x \qquad x_{F2} = f_x x_b - l_x \theta_2^x \tag{5.2}$$

The next step is to see how the impact points will be affected by a beam displacement in the z direction. We will therefore include a shift of the interaction point equal to z_b, as shown in fig. 5.4.

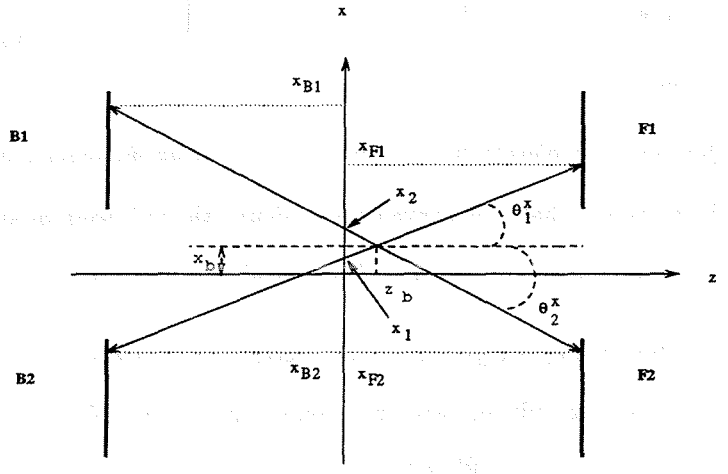

Figure 5.4: *Events on the two diagonals for nonzero beam displacements, x_b and z_b, and zero tilts.*

As evident from fig. 5.4, the effect of the z displacement is equivalent to that of two different x displacements, x_1 and x_2, in the two diagonals taken at z=0:

$$x_1 = x_b - z_b \theta_1^x \qquad x_2 = x_b + z_b \theta_2^x. \tag{5.3}$$

The impact points are thus given by

$$x_{F1} = f_x(x_b - z_b \theta_1^x) + l_x \theta_1^x \qquad x_{B2} = f_x(x_b - z_b \theta_1^x) - l_x \theta_1^x$$

$$x_{B1} = f_x(x_b + z_b\theta_2^x) + l_x\theta_2^x \qquad x_{F2} = f_x(x_b + z_b\theta_2^x) - l_x\theta_2^x. \tag{5.4}$$

We can now consider the case of nonzero tilts. Fig. 5.5 shows events in the two diagonals, where it has been assumed that the positron beam has a positive tilt, θ_+^x, whereas the electron beam has a negative tilt, θ_-^x. The equations for the x impact points will now be affected in terms of the production angle, namely

$$\begin{aligned} x_{F1} &= f_x x_b + l_x(\theta_1^x - |\theta_-^x|) = f_x x_b + l_x(\theta_1^x + \theta_-^x) \qquad x_{B2} = f_x x_b - l_x(\theta_1^x + |\theta_+^x|) = f_x x_b - l_x(\theta_1^x + \theta_+^x) \\ x_{B1} &= f_x x_b + l_x(\theta_2^x - |\theta_+^x|) = f_x x_b + l_x(\theta_2^x - \theta_+^x) \qquad x_{F2} = f_x x_b - l_x(\theta_2^x + |\theta_-^x|) = f_x x_b - l_x(\theta_2^x - \theta_-^x) \end{aligned} \tag{5.5}$$

If we combine eqs. (5.4) and (5.5), we obtain for the general case of nonzero beam displacements and nonzero tilts:

$$\begin{aligned} x_{F1} &= f_x(x_b - z_b(\theta_1^x + \theta_-^x)) + l_x(\theta_1^x + \theta_-^x) \qquad x_{B2} = f_x(x_b - z_b(\theta_1^x + \theta_+^x)) - l_x(\theta_1^x + \theta_+^x) \\ x_{B1} &= f_x(x_b + z_b(\theta_2^x - \theta_+^x)) + l_x(\theta_2^x - \theta_+^x) \qquad x_{F2} = f_x(x_b + z_b(\theta_2^x - \theta_-^x)) - l_x(\theta_2^x - \theta_-^x) \end{aligned} \tag{5.6}$$

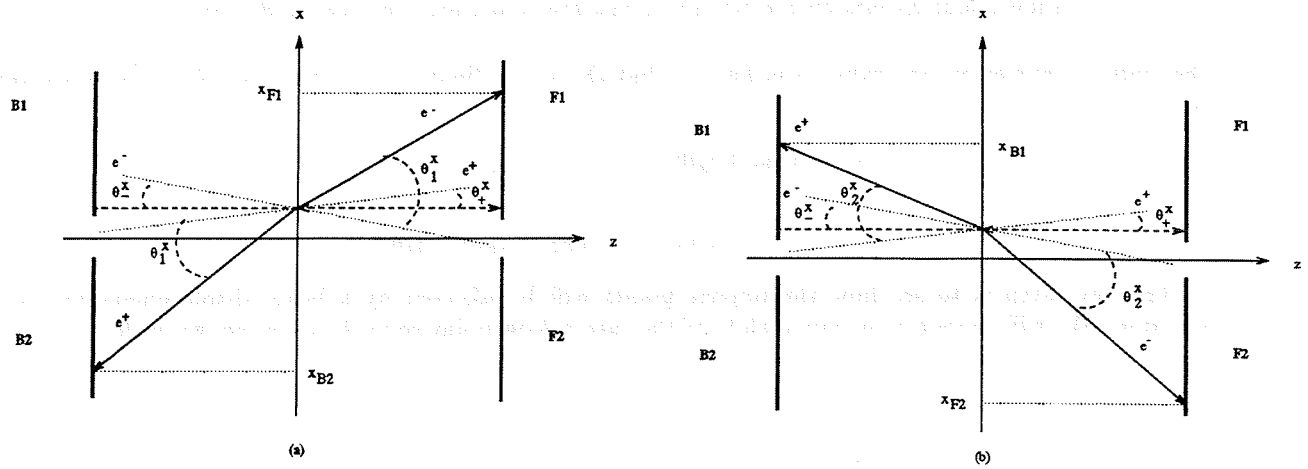

Figure 5.5: *Events for zero z displacement and nonzero tilts (a) on diagonal 1 and (b) on diagonal 2.*

From these equations, we see that it is convenient to define the following quantities:

$$\begin{aligned} \Delta x_1 &= x_{F1} + x_{B2} = 2 \cdot f_x(x_b - z_b(\theta_1^x + \theta_x)) + \epsilon_x l_x \\ \Delta x_2 &= x_{F2} + x_{B1} = 2 \cdot f_x(x_b + z_b(\theta_2^x - \theta_x)) + \epsilon_x l_x \end{aligned} \tag{5.7}$$

where we have defined the average tilt, θ_x, and the acollinearity, ϵ_x, as follows

$$\theta_x = \frac{\theta_+^x + \theta_-^x}{2} \qquad \epsilon_x = \theta_-^x - \theta_+^x \tag{5.8}$$

To better separate the dependence on different beam parameters, we define the following quantities:

$$\Delta x_0 = \frac{\Delta x_1 + \Delta x_2}{2} = 2 \cdot f_x x_b + \epsilon_x l_x + f_x z_b(\theta_2^x - \theta_1^x - 2\theta_x) \tag{5.9}$$

$$\delta x = \Delta x_2 - \Delta x_1 = 2 \cdot f_x z_b(\theta_1^x + \theta_2^x) \tag{5.10}$$

By taking the average over a reasonably long period of time (for this analysis, it is useful to use the time needed to write a cassette, which is about 20 minutes and corresponds to about 3000 events), we can

substitute θ_1^x and θ_2^x with their average values, which are both very close to 5.5 mrad. This shows that δx essentially depends only on the value of z_b. On the contrary, Δx_0 essentially measures the combined effect of the beam x displacement and beam acollinearity in the (x,z) plane, since the third term in eq. (5.9) is completely negligible.

The similarity of the x_b and ϵ_x effects on the impact points is clearly depicted in fig. 5.6, where we have assumed for simplicity that only the electron beam has a nonzero tilt: the full lines correspond to outgoing particle tracks for $x_b = \theta_-^x = \theta_+^x = 0$, whereas the dotted line shows the case of nonzero acollinearity and x_b=0 and the dashed line shows an event with zero acollinearity but nonzero x_b, which has the same impact points on the modules, showing that the ϵ_x and x_b effects are equivalent, and therefore these two parameters cannot be determined separately using the VSAT information alone.

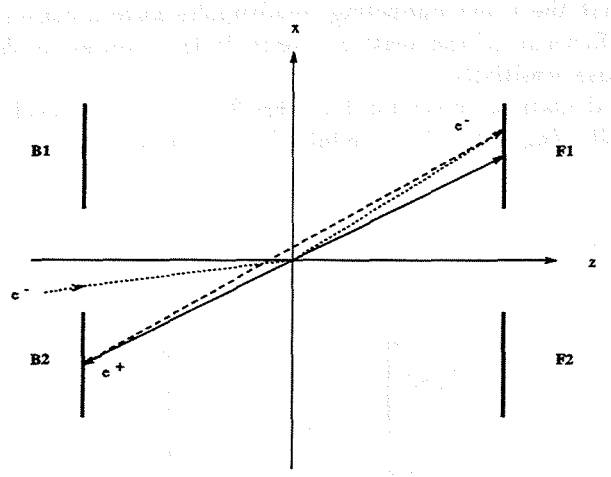

Figure 5.6: *Effects of the acollinearity and the x displacement on the impact points.*

There are two other useful measures that can be done with the VSAT and which are related to the beam tilt and production angles. With a view to this, it is helpful to consider events with equal (positive) beam tilt angles, θ_+^x and θ_-^x, as in fig. 5.7. The figure shows clearly that the (average) production angle on

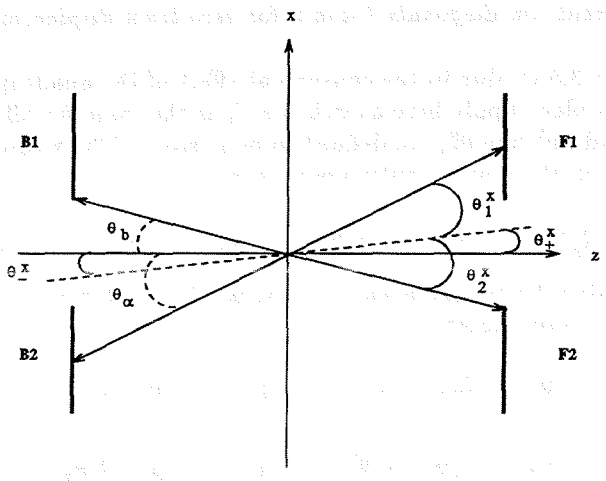

Figure 5.7: *Effect of the beam tilts on the production angles on the two diagonals.*

diagonal 1, θ_1^x, is smaller than in the case of zero tilts, where it would be equal to θ_α. The opposite holds for the production angle on diagonal 2: θ_2^x is larger than θ_b. Due to the rapid decrease of the Bhabha cross section with the angle, this induces an opposite variation of the number of accepted Bhabha events on the two diagonals: the number of events on diagonal 1, N_1, will increase, whereas the number of events on diagonal 2, N_2, will decrease. Therefore, we expect to observe a variation of the variable:

$$A_D = \frac{N_1 - N_2}{N_1 + N_2} \tag{5.11}$$

called diagonal asymmetry. It must be noted, however, that the diagonal asymmetry is only affected by the average tilt angle, θ_x, and not by the separate values of θ_-^x and θ_+^x. By consequence, it cannot be used to extract information on the acollinearity, ϵ_x. The relationship between A_D and θ_x has been determined by FASTSIM [25].

Finally, from eq. (5.9), we see that the average value $R\Delta x_0$ of the combined widths $R\Delta x_1$ and $R\Delta x_2$ of the Δx_1 and Δx_2 distributions is related to the widths σ_x and σ_z of the incident beams at the interaction point and to their divergences in the (x,z) plane.

5.2.2 Beam parameters in the (y,z) plane

The situation in this plane is analogous to what we saw in the previous section for the (x,z) plane, the only difference being that the superconducting quadrupoles have a convergent rather than a divergent effect. This induces a focusing of the scattered particle trajectories in the y direction, which in turn causes the detector to lose sensitivity.

We will repeat the calculations of section 5.2.1 briefly. First, we consider the simple case of no beam displacement and zero tilts (fig. 5.8). The modules have been moved to

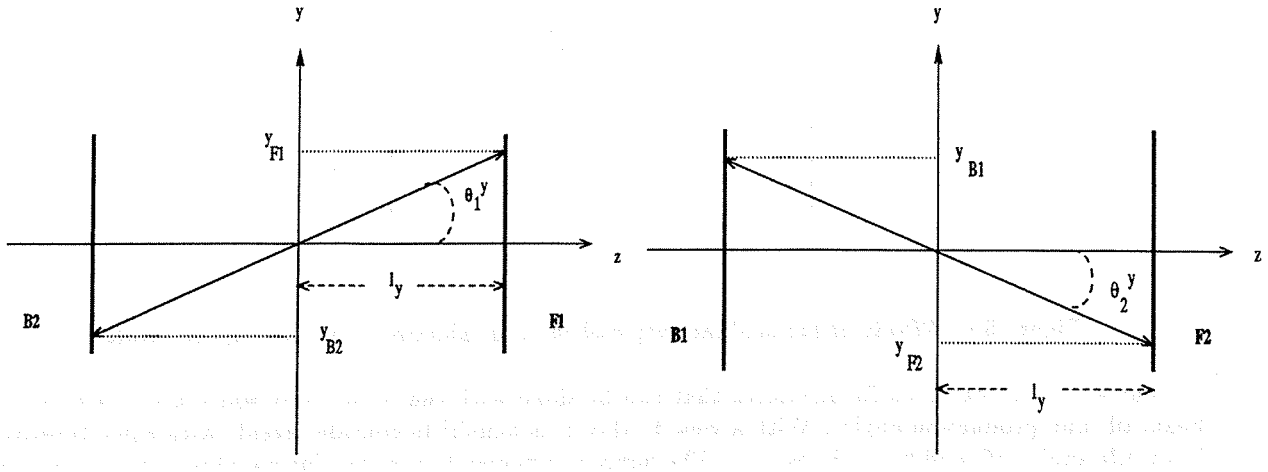

Figure 5.8: *Events on diagonals 1 and 2 for zero beam displacement and zero tilts.*

an effective distance, $l_y = 3.5$ m, due to the convergent effect of the quadrupoles. The same assumptions as in the case of the (x,z) plane apply here as well, i.e. l_y is the same for all modules and the production angles on the two diagonals, θ_1^y and θ_2^y, are defined to be positive. The y coordinates of the impact points of the outgoing particles on the four modules are then given by

$$y_{F1} = l_y\theta_1^y \qquad y_{B2} = -l_y\theta_1^y \qquad y_{B1} = l_y\theta_2^y \qquad y_{F2} = -l_y\theta_2^y \tag{5.12}$$

The next step is to include a beam displacement in y, y_b. The factor f_y is of the order of 0.1. From fig. 5.9 we can calculate the y coordinates:

$$\begin{aligned} y_{F1} &= f_y y_b + l_y\theta_1^y \qquad & y_{B2} &= f_y y_b - l_y\theta_1^y \\ y_{B1} &= f_y y_b + l_y\theta_2^y \qquad & y_{F2} &= f_y y_b - l_y\theta_2^y \end{aligned} \tag{5.13}$$

We define

$$\Delta y_1 = y_{F1} + y_{B2} \qquad \Delta y_2 = y_{F2} + y_{B1} \tag{5.14}$$

The effect of a shift of y_b on those variables is similar to that of a shift of x_b on the corresponding quantities of the (x,z) plane: from the last equations we have $\Delta y_1 = \Delta y_2 = 2f_y y_b$, therefore the variables Δy_1, Δy_2 and $\Delta y_0 = (\Delta y_1 + \Delta y_2)/2$ vary proportionally to y_b, whereas the difference $\Delta y_1 - \Delta y_2$ is always zero. We can now continue to consider the situation presented in fig. 5.10, where we have assumed a positive z displacement, z_b. From the figure, we obtain

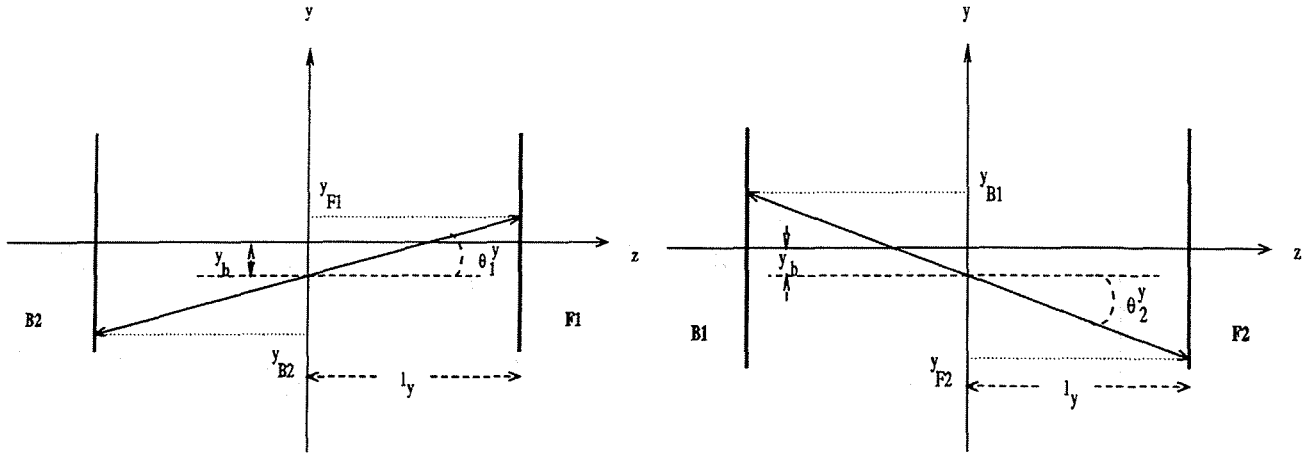

Figure 5.9: *Events on the two diagonals for zero z displacement and zero tilts.*

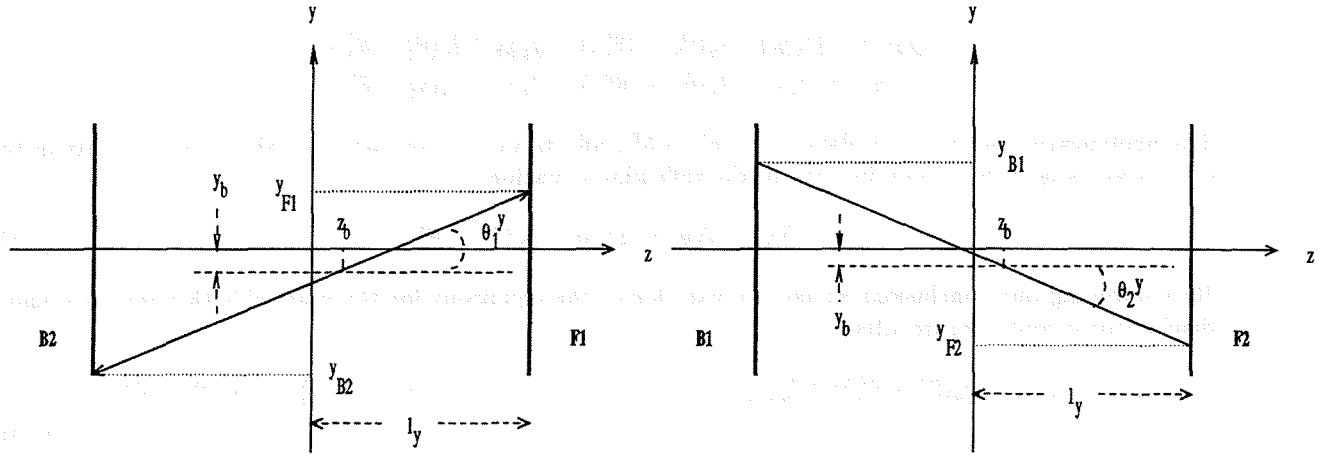

Figure 5.10: *Events on the two diagonals for nonzero z displacement and zero tilts.*

$$y_{F1} = f_y(y_b - z_b\theta_1^y) + l_y\theta_1^y \qquad y_{B2} = f_y(y_b - z_b\theta_1^y) - l_y\theta_1^y$$
$$y_{B1} = f_y(y_b + z_b\theta_2^y) + l_y\theta_2^y \qquad y_{F2} = f_y(y_b + z_b\theta_2^y) - l_y\theta_2^y \tag{5.15}$$

Consequently, the corrected factor is the one including the y_b value, which needs to have subtracted from (diagonal 1) or added to (diagonal 2) a quantity proportionally related to z_b. This induces a proportional variation of Δy_1 and Δy_2 with respect to z_b, now being given by

$$\Delta y_1 = 2f_y(y_b - z_b\theta_1^y) \qquad \Delta y_2 = 2f_y(y_b + z_b\theta_2^y) \tag{5.16}$$

again including both y_b and z_b in the same equation.

Lastly, the case of nonzero beam tilts has to be mentioned. The y displacement is again taken to be negative while the interaction point is assumed to have no displacement in the z direction. The positron (electron) beam has a positive (negative) tilt denoted by θ_+^y (θ_-^y). The situation is shown in fig. 5.11, from which it can be derived that

$$y_{F1} = f_y y_b + l_y(\theta_1^y - |\theta_-^y|) = f_y y_b + l_y(\theta_1^y + \theta_-^y)$$
$$y_{B2} = f_y y_b - l_y(\theta_1^y + |\theta_+^y|) = f_y y_b - l_y(\theta_1^y + \theta_+^y) \tag{5.17}$$

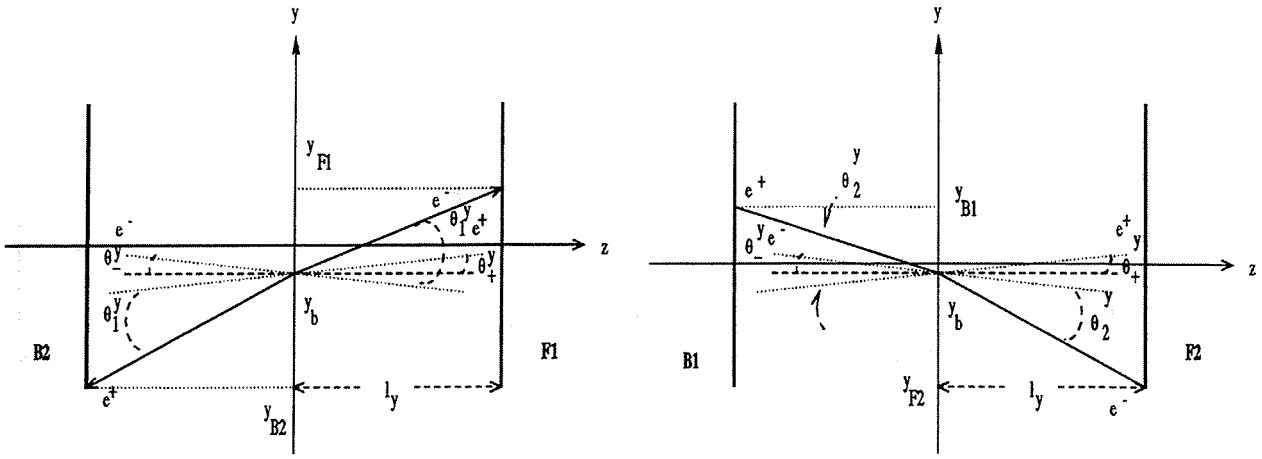

Figure 5.11: *Events on the two diagonals for zero z displacement and nonzero tilts.*

$$y_{B1} = -|f_y y_b| + l_y(\theta_2^y - |\theta_+^y|) = f_y y_b + l_y(\theta_2^y - \theta_+^y)$$
$$y_{F2} = f_y y_b - l_y(\theta_2^y + |\theta_-^y|) = f_y y_b - l_y(\theta_2^y - \theta_-^y)$$

The acollinearity in the (y,z) plane, $\epsilon_y = \theta_-^y - \theta_+^y$, affects the y coordinates of the impact points in the same way as y_b does, as can be seen in the following equation:

$$\Delta y_1 = \Delta y_2 = 2 f_y y_b + l_y(\theta_-^y - \theta_+^y) \tag{5.18}$$

By combining our conclusions so far, we can derive the equations for the case of both nonzero y and z displacement and nonzero tilts:

$$\begin{aligned} y_{F1} &= f_y(y_b - z_b(\theta_1^y + \theta_-^y)) + l_y(\theta_1^y + \theta_-^y) & y_{B2} &= f_y(y_b - z_b(\theta_1^y + \theta_+^y)) - l_y(\theta_1^y + \theta_+^y) \\ y_{B1} &= f_y(y_b + z_b(\theta_2^y - \theta_+^y)) + l_y(\theta_2^y - \theta_+^y) & y_{F2} &= f_y(y_b + z_b(\theta_2^y - \theta_-^y)) - l_y(\theta_2^y - \theta_-^y) \end{aligned} \tag{5.19}$$

from which

$$\Delta y_1 = 2 f_y(y_b - z_b(\theta_1^y + \theta_y)) + l_y \epsilon_y \qquad \Delta y_2 = 2 f_y(y_b + z_b(\theta_2^y - \theta_y)) + l_y \epsilon_y \tag{5.20}$$

Using the average values of Δy_1 and Δy_2 over one cassette we conclude that

$$\Delta y_0 = 2 f_y y_b + l_y \epsilon_y - f_y z_b(\theta_1^y - \theta_2^y + 2\theta_y) \tag{5.21}$$

The average values of θ_1^y and θ_2^y are very close to zero and also the product $f_y z_b \theta_y$ is extremely small, so the third term in the r.h.s. of eq. (5.21) is completely negligible.

One can also define the difference δy:

$$\delta y = \Delta y_2 - \Delta y_1 = 2 \cdot f_y z_b(\theta_1^y + \theta_2^y) \tag{5.22}$$

but, due to the very small values of f_y, θ_1^y and θ_2^y, δy is practically zero and thus carries no useful information on z_b.

5.3 Determination of the beamspot

From VSAT data alone we can estimate the z coordinate of the interaction point using eq. (5.10), but this is not possible neither for the x nor for the y coordinate. This is due to the fact that, as shown in eq. (5.9) and (5.21), the detector variables depend both on the beam displacement and on the acollinearity in those directions. However, we can use the beamspot values for x and y as they are determined by VD and TPC to obtain information on the variations of the acollinearity.

5.3.1 Estimation of the x beamspot

The evolution of Δx during the 1995 scan data taking is shown in fig. 5.12 (we recall that Δx represents the average value over the events of a cassette). Due to the limited VSAT acceptance in the x direction, this average value must be corrected, since Δx_1 and Δx_2 represent average values of rather broad distributions, which are affected in non trivial ways by different beam parameters, such as beam width, divergence and acollinearity.

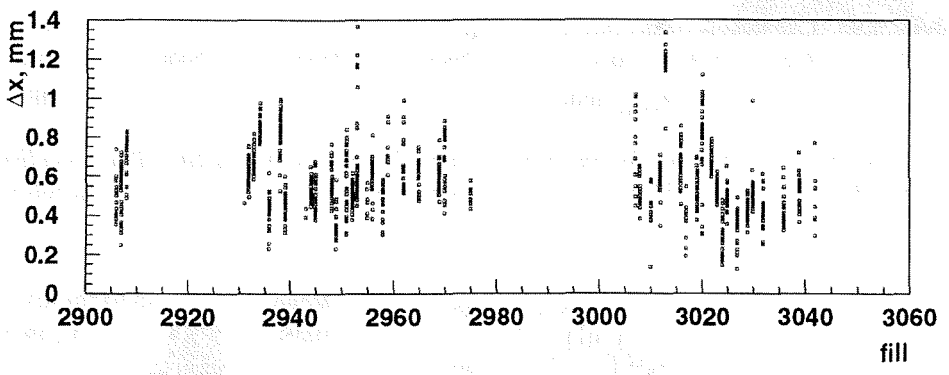

Figure 5.12: *Variations of Δx during the 1995 scan.*

Furthermore, the averaging procedure introduces a dependence of Δx_1 and Δx_2 on the y tilt. FASTSIM has shown that these effects can be parametrized in terms of quantities directly measured by the VSAT. The correction for the beam width and divergence effect can be expressed as a dependence on the widths of the Δx_1 and Δx_2 distributions, $R\Delta x_1$ and $R\Delta x_2$, respectively; the correction for the tilt in y can be achieved through the Δy_1 and Δy_1 distributions. The resulting relations are then [25]

$$\begin{aligned} \Delta x_{1C} &= \Delta x_1(1 + 0.1(R\Delta x_1 - 2.6)) - 0.1(\Delta y_1 + 7) \\ \Delta x_{2C} &= \Delta x_2(1 + 0.1(R\Delta x_2 - 2.8)) - 0.05(\Delta y_2 + 8) \end{aligned} \tag{5.23}$$

where all quantities are measured in mm. Consequently, Δx_0 and δx of eqs. (5.9) and (5.10) should be replaced by the quantities $\Delta x_C = (\Delta x_{1C} + \Delta x_{2C})/2$ and $\delta x_C = \Delta x_{2C} - \Delta x_{1C}$, respectively. It is convenient to define the quantity x_{VSAT} as follows:

$$x_{VSAT} = \frac{\Delta x_C}{2 f_x} \tag{5.24}$$

It is then clear that, from eqs. (5.9) and (5.24),

$$x_{VSAT} = x_b + \epsilon_x \frac{l_x}{2 f_x} + x_0 \tag{5.25}$$

where we have included in the offset x_0 the small term $\frac{z_b}{2}(\theta_2^x - \theta_1^x - 2\theta_x)$ of eq. (5.9), which is practically constant, since θ_1^x and θ_2^x are practically equal and θ_x is very small.

As evident from eq. (5.25), x_{VSAT} is directly related to x_b at fixed acollinearity. The distributions of x_{VSAT} for the scan and for the periods before and after the radiation accident (i.e. for fill < 3000 and for fill > 3000, respectively) are shown in fig. 5.13. The variation with fill number is shown in the same figure. The mean value for the entire scan was (0.162 ± 0.055) *mm*. The corresponding values before and after the accident were (0.168 ± 0.048) *mm* and (0.154 ± 0.062) *mm*, respectively. In fig. 5.14(a), x_{VSAT} is plotted versus x_{VD}. The figure shows a qualitative agreement and suggests a linear relation between the two measurements within an overall shift of the order of 3 mm.

In fig. 5.14(b), we have plotted the normalized difference to the expected errors in x_{VSAT} and x_{VD} measurements. This difference is given by the relation

$$\delta x_{norm} = \frac{x_{VSAT} - < x_{VSAT} > -(x_{VD} - < x_{VD} >)}{\sqrt{\sigma^2_{x_{VSAT}} + \sigma^2_{x_{VD}}}} \tag{5.26}$$

We see that the average fluctuation is about twice the expected value. Since the estimation of x_{VSAT} has been done under the assumption of fixed acollinearity, we conclude that the variations of this parameter

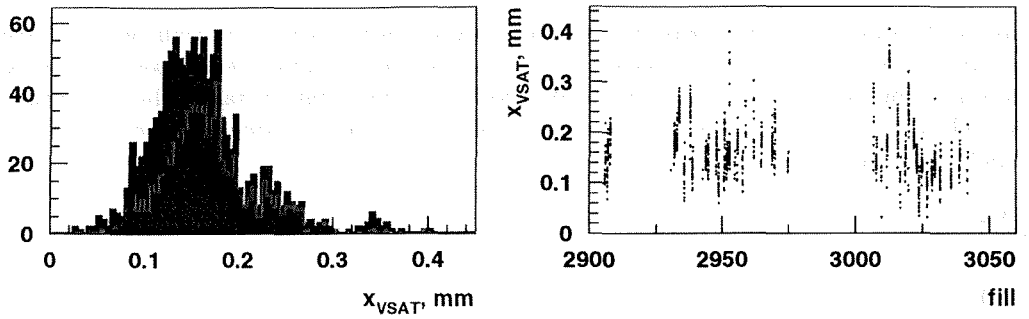

Figure 5.13: *x_{VSAT} with corrections for the beam width, divergence and y-tilt. The x-acollinearity effect has not been included. The green (blue) curve corresponds to data before (after) the accident.*

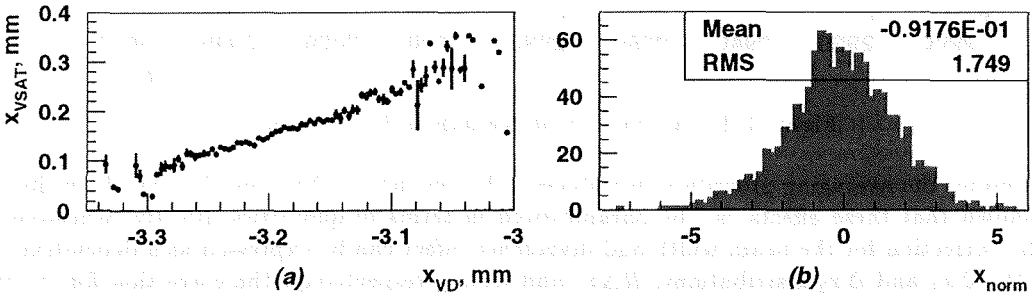

Figure 5.14: *(a) x_{VSAT} from VSAT plotted versus x_{VD}, (b) normalized difference between x_{VSAT} from VSAT and x_{VD}.*

have a significant contribution to the determination of the interaction point. From FASTSIM simulations done for different beam tilts, we estimate that an average fluctuation in acollinearity of the order of 15 μrad is sufficient to produce an additional variation of about 40 μm in the VSAT determination of x_{VSAT} [28]. This could allow us to assume a systematic difference in acollinearity of about 5 μrad in order to explain the shift of the mean value between the periods before and after the accident.

5.3.2 Estimation of the y beamspot

As was mentioned in section 5.2.2, the situation in the (y,z) plane is similar to that in the (x,z) plane, apart from the fact that the effect of the superconducting quadrupoles is here convergent. The reduced sensitivity of the detector thus induced prohibits an estimation of the y beamspot from eq. (5.21). To confirm this, we plot in fig. 5.15 y_{VSAT} from eq. (5.21) versus the y beamspot measurement of the VD. We see that there is no correlation.

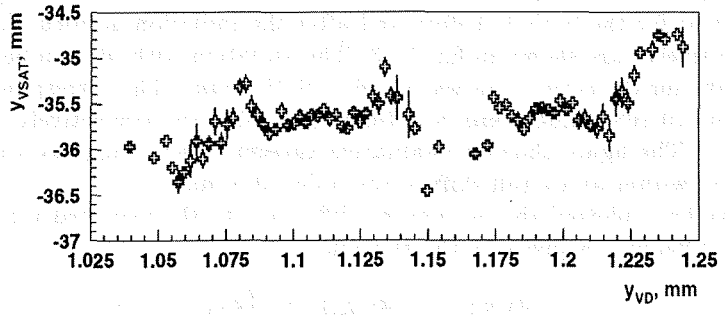

Figure 5.15: *y_{VSAT} versus y_{VD}. ϵ_y was neglected in the VSAT measurement.*

5.3.3 Estimation of the z beamspot

According to the corrections of section 5.3.1, eq. (5.10) gives

$$z_{VSAT} = \frac{\delta x_C}{2 f_x (\theta_1^x + \theta_2^x)} \tag{5.27}$$

where we have substituted z_{VSAT} for z_b for clarity. The sum of the production angles can be derived from the expressions of the impact points, eq. (5.6), as follows:

$$\theta_1^x + \theta_2^x = \frac{x_{F1} - x_{B2} - x_{F2} + x_{B1}}{2 \cdot l_x} \tag{5.28}$$

The estimation of z_{VSAT} is given in fig. 5.16. The mean value before and after the accident was (-45.976 ± 3.316) *mm* and (-50.195 ± 4.611) *mm*, respectively. The overall mean value was (-47.769 ± 4.440) *mm*.

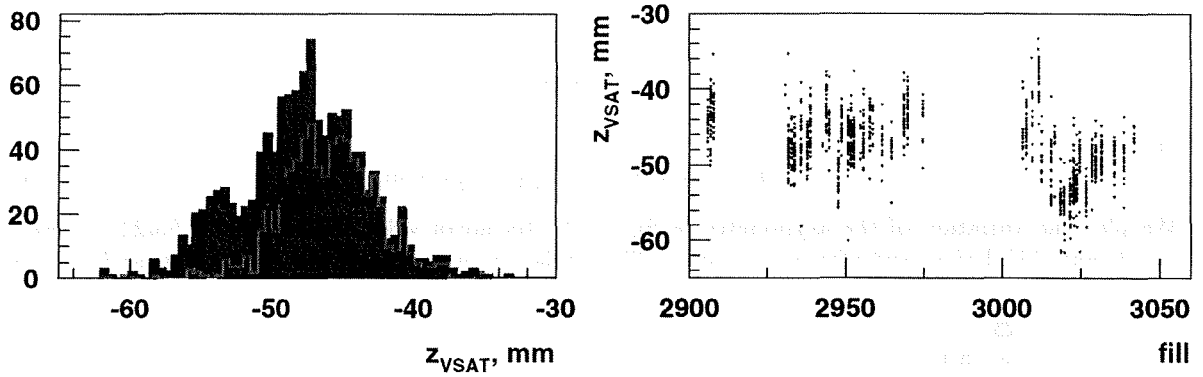

Figure 5.16: *z_{VSAT} with corrections for the beam width, divergence and y-tilt. The x-acollinearity effect has not been included. The green (blue) curve corresponds to data before (after) the accident.*

In fig. 5.17(a), we have plotted the VSAT versus the TPC measurement for the z beamspot. We discern a linear relation as in the case of x_{VSAT} (fig. 5.14(a)). The offset between the two measurements is 35 mm approximately. The normalized difference distribution is given in fig. 5.17(b).

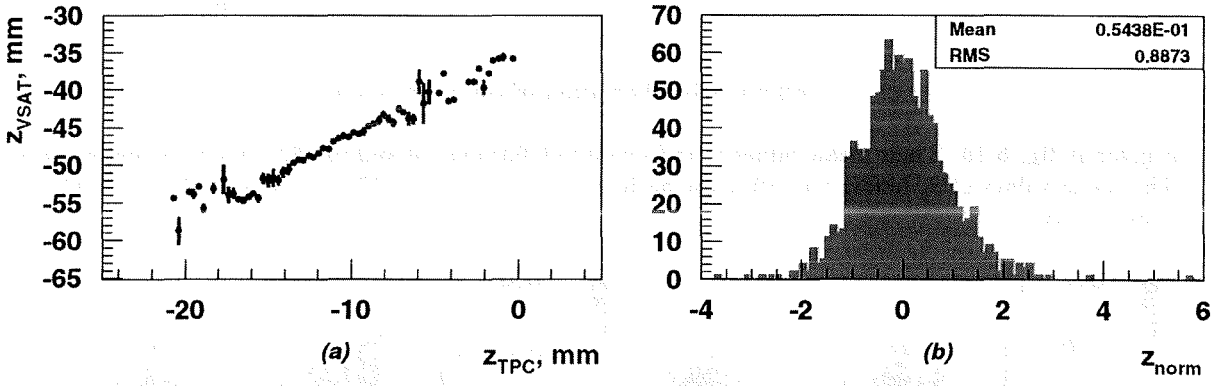

Figure 5.17: *(a) z_{VSAT} versus z_{TPC}, (b) normalized difference between z_{VSAT} and z_{TPC}.*

The rms of fig. 5.17(b) is close to unity as expected. This is because the effect of the acollinearity cancels out in the difference $\Delta x_2 - \Delta x_1$.

5.4 Variation of the asymmetry, tilt and acollinearity.

We can calculate the asymmetry directly from the data by using eq. (5.11), where N_1 and N_2 are the Bhabha events on diagonals 1 and 2, respectively. As was mentioned in section 5.2.1, FASTSIM has

provided us with a relation between the asymmetry and the mean tilt angle in the (x,z) plane, which allows us to monitor variations of θ_x according to

$$\theta_x = 1.75 \cdot A_D \tag{5.29}$$

where θ_x is in mrad. It is possible to estimate the mean tilt, θ_y, in the (y,z) plane from the relations giving the y coordinates of the impact points (eq. (5.19)):

$$y_{F1} + y_{F2} - y_{B1} - y_{B2} =$$

$$= 2f_y z_b(\theta_+^y - \theta_-^y) + 2l_y(\theta_1^y - \theta_2^y + \theta_-^y + \theta_+^y) =$$

$$= -2f_y z_b \epsilon_y + 2l_y(\theta_1^y - \theta_2^y) + 4l_y\theta_y \approx$$

$$\approx 4l_y\theta_y$$

and thus

$$\theta_y \approx (y_{F1} + y_{F2} - y_{B1} - y_{B2})/4l_y \tag{5.30}$$

We plot the variation of the asymmetry in fig. 5.18. Its mean value was -0.047 ± 0.022. There is no significant shift before and after the accident. The variation of the mean tilts in the (x,z) and (y,z) planes

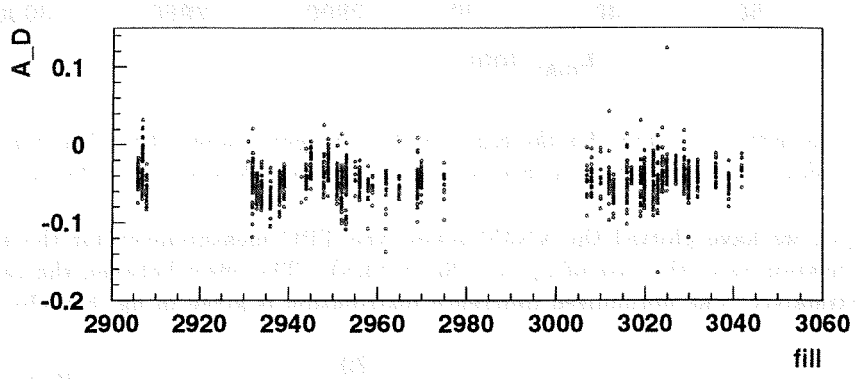

Figure 5.18: *Variation of the asymmetry.*

is given in fig. 5.19. Their mean values were (-0.082 ± 0.038) *mrad* and (0.462 ± 0.076) *mrad*, respectively. The mean values of θ_y before and after the accident were (0.474 ± 0.076) *mrad* and (0.447 ± 0.072) *mrad*, respectively.

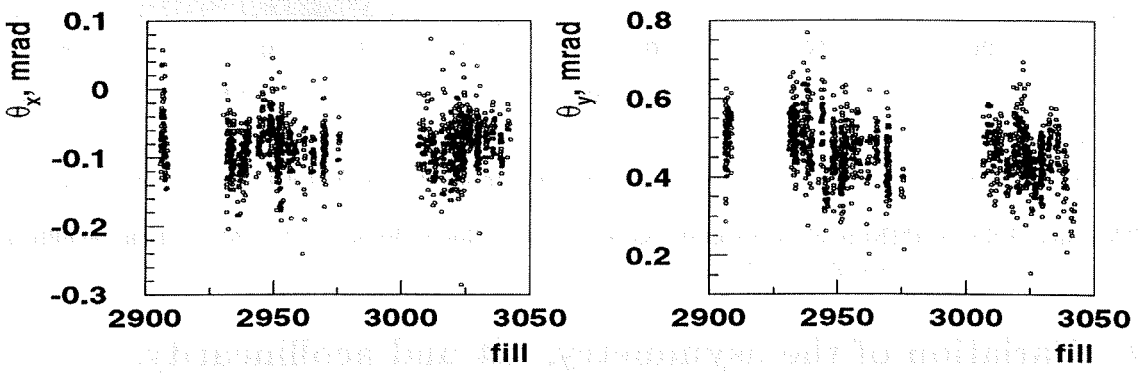

Figure 5.19: *Variations of θ_x and θ_y.*

The VD beamspot data can be used to provide us with information on the acollinearity in (x,z) and (y,z) plane. To this end, we introduce the VD values for x beamspot and y beamspot in eqs. (5.9) and (5.21), from which we obtain the following expressions:

$$\epsilon_x \approx \frac{\Delta x_C - 2f_x \cdot x_{VD}}{l_x} \tag{5.31}$$

$$\epsilon_y \approx \frac{\Delta y - 2f_y \cdot y_{VD}}{l_y} \tag{5.32}$$

We plot the ϵ_x and ϵ_y variations in fig. 5.20. The overall, before and after the accident mean values of

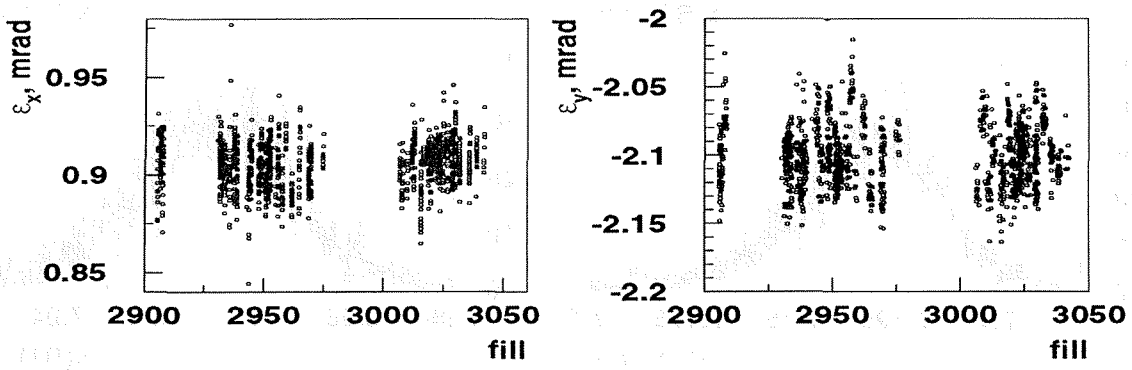

Figure 5.20: *Variation of ϵ_x and ϵ_y*

ϵ_x were (0.905 ± 0.012) *mrad*, (0.904 ± 0.012) *mrad* and (0.907 ± 0.010) *mrad*, respectively. We observe a difference of 3 μrad between the last two values, which agrees with our prediction of 5 μrad in section 5.3.1. The overall mean value of ϵ_y was (-2.101 ± 0.023) *mrad* and it has not showed a shift before and after the accident.

We have mentioned that the effect of the beam widths and divergences on the x_{VSAT} values is detected in terms of $R\Delta x$. We show the variations of this parameter in fig. 5.21. Its overall mean value was (1.937 ± 0.081) *mm*. It mean value before the accident was (1.947 ± 0.080) *mm* and after the accident (1.922 ± 0.080) *mm*.

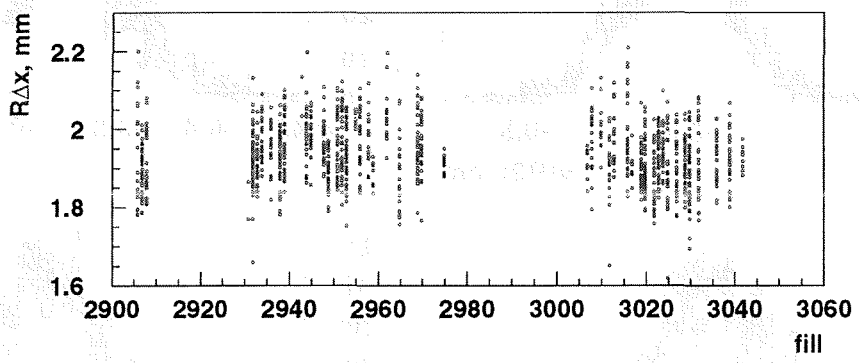

Figure 5.21: *Variation of $R\Delta x$.*

5.5 Dependence on minibunch number.

The only point which is left for us to examine at this stage is whether the beam parameters above depend on the minibunch number. Since all our calculations are based on the x and y values of the particle impact points on the four modules, we plot these values for the three minibunches in figs. 5.21 and 5.22. We observe that there is no dependence on minibunch number.

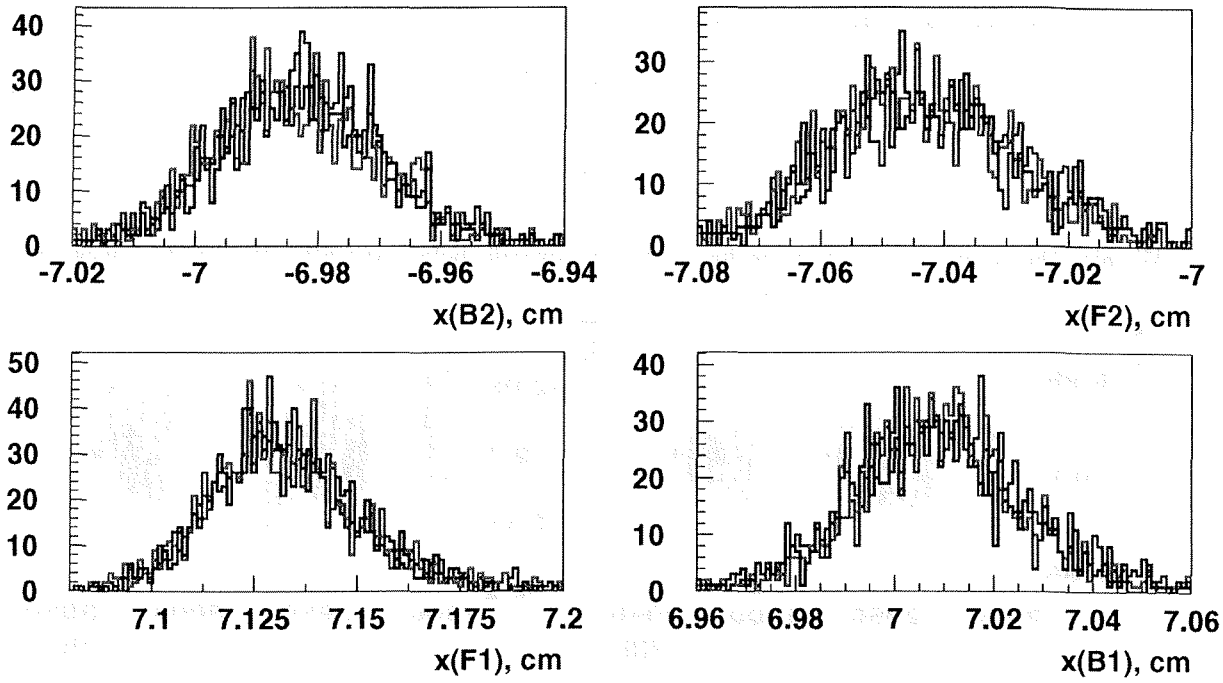

Figure 5.22: *x impact point values for the four modules and minibunch number one (red curves), two (green curves) and three (blue curves).*

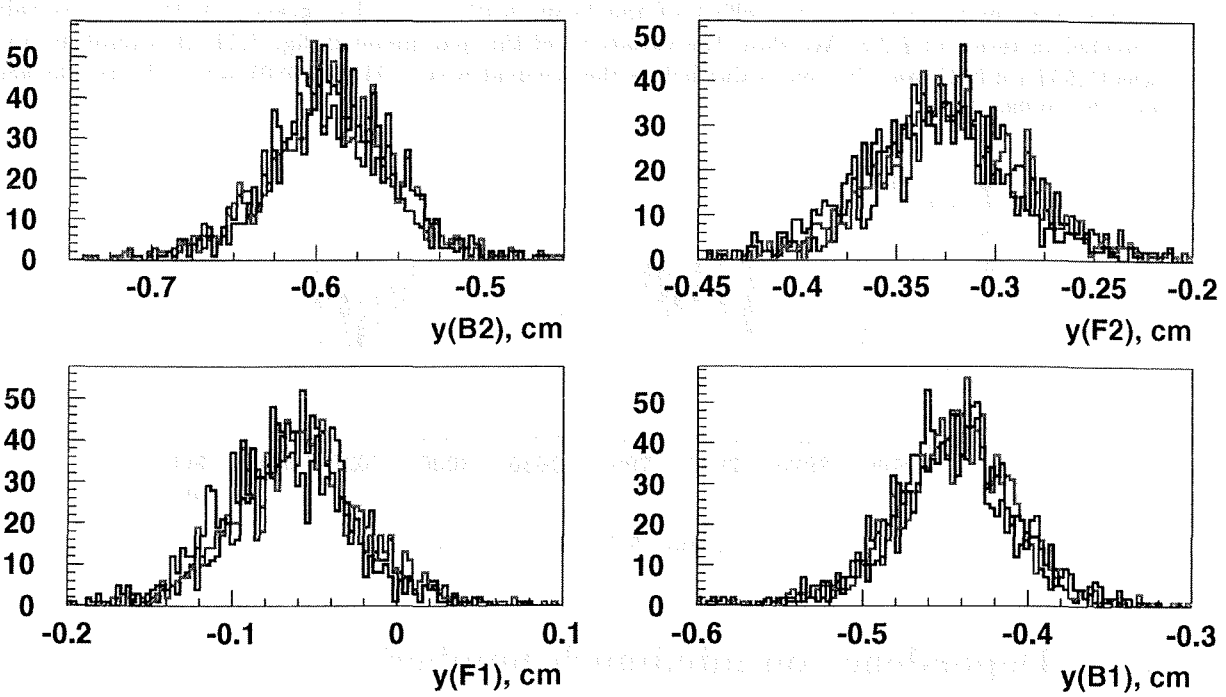

Figure 5.23: *y impact point values for the four modules and minibunch number one (red curves), two (green curves) and three (blue curves).*

Chapter 6

The Simulation

In chapter 4, we described how we obtain the Bhabha sample that we need for the luminosity evaluation. What we need to calculate now is the accepted Bhabha cross section of our detector. This can be determined by convoluting the theoretical cross section with the geometrical acceptance of the VSAT. The analytical calculation is very complicated [9] and the natural way out is to use a simulation instead. We describe this simulation, called FASTSIM, in section 6.1. After calculating the accepted cross section, we have to correct it for the variation of the beam parameters. This is described in section 6.2.

6.1 Description of FASTSIM

6.1.1 Tracking of particles from the interaction point to the VSAT modules

The events are generated with the BHLUMI program [29], where exponentiated corrections (from third order and thereafter) have been implemented giving a theoretical uncertainty of about 0.1%. FASTSIM then tracks the particles from the interaction point to the detector as follows [9].

The path of the scattered particle is divided into three different transport regions. From the interaction point to 3.7 m along the z-direction it passes through the magnetic field of the DELPHI solenoid. After that it travels through the field of the superconducting quadrupoles, which are located between 3.7 m and 5.7 m along the beam axis. The last part of the particle's path is the field-free region between the quadrupoles and the modules, which are placed at 7.7 m from the interaction point.

A convenient way to describe this motion is to use the phase space coordinates x, y, $x' = dx/ds$ and $y' = dy/ds$, where s is the coordinate along the trajectory. The motion of the particle through each of the above mentioned regions can then be represented by a matrix describing the transformation of the phase space coordinates. The path of the particle from the interaction point (ip) to the VSAT module is thus written as:

$$\begin{pmatrix} x \\ x' \\ y \\ y' \end{pmatrix}_{VSAT} = T_3 T_2 T_1 \begin{pmatrix} x \\ x' \\ y \\ y' \end{pmatrix}_{ip} \tag{6.1}$$

where T_1, T_2, T_3 are the transformation matrices for the three transport regions described above.

The transformation of the phase space under the influence of the DELPHI solenoid field can be written by introducing the bending strength of the solenoid field

$$\frac{1}{\rho} = \frac{-0.2998B}{p} \tag{6.2}$$

where B is the magnetic field in Tesla, ρ is the bending radius and p is the particle's momentum in GeV and the corresponding bending angle

$$\phi = \frac{q(z_1 - z_0)}{\rho} \tag{6.3}$$

where q is the charge of the particle and $z_1 - z_0$ is the distance traversed in the magnetic field. The expression for the T_1 matrix is then

$$T_1 = \begin{pmatrix} 1 & q\rho sin\phi & 0 & q\rho(cos\phi - 1) \\ 0 & cos\phi & 0 & -sin\phi \\ 0 & -q\rho(cos\phi - 1) & 1 & q\rho sin\phi \\ 0 & sin\phi & 0 & cos\phi \end{pmatrix} \tag{6.4}$$

The T_2 matrix giving the transformation of the phase space through the quadrupole field is of the form

$$T_2 = \begin{pmatrix} a_{11} & a_{12} & a_{13}(\theta) & a_{14}(\theta) \\ a_{21} & a_{22} & a_{23}(\theta) & a_{24}(\theta) \\ a_{31}(\theta) & a_{32}(\theta) & a_{33} & a_{34} \\ a_{41}(\theta) & a_{42}(\theta) & a_{43} & a_{44} \end{pmatrix} \tag{6.5}$$

The T_2 matrix elements are functions of the length and strength of the quadrupole field and also of the momentum of the particle. For a quadrupole field the focusing or defocusing effect in one direction (x or y) depends only on the phase space components in that direction (i.e. x and y are decoupled). However, the quadrupoles are rotated by an angle θ with respect to the VSAT coordinate system. Therefore, the coordinates of the particle have to be rotated into the quadrupole coordinate system before making the transformation through the quadrupoles and rotated back afterwards. Consequently, the elements in the upper right and lower left part of the matrix, connecting the vertical and horizontal coordinates, will be dependent on the rotation angle θ.

The region between 5.7 m and 7.7 m being a field-free region, the matrix T_3 is simply

$$T_3 = \begin{pmatrix} 1 & z_3 - z_2 & 0 & 0 \\ 0 & 1 & 0 & 0 \\ 0 & 0 & 1 & z_3 - z_2 \\ 0 & 0 & 0 & 1 \end{pmatrix} \tag{6.6}$$

where z_3 is the z position of the VSAT module and z_2 is the exit of the quadrupole.

With the values of T_1, T_2 and T_3 inserted into eq. (6.1), a relation between the phase space of the electron at the interaction point and at the impact point on VSAT module 1 is derived, e.g.

$$x_{v1} = A_{x1}x'_{ip} + B_{x1}x_{ip} + (C_x + D_x)y'_{ip} + E_x y_{ip} \tag{6.7}$$

The effect of the solenoid field is contained in the constant D_x and the effect of the relative orientation between LEP and DELPHI horizontal planes is manifested in the constants C_x and E_x.

Since a Bhabha event is defined as a coincidence between two diagonal modules, we also need to track the positron to the opposite module (index 2) from the interaction point. Under the assumption of collinear Bhabha events the slopes x' and y' are equal for the two particles and the relation for the positron reads

$$x_{v2} = A_{x2}x'_{ip} - B_{x2}x_{ip} + (C_x - D_x)y'_{ip} - E_x y_{ip} \tag{6.8}$$

The particle on module 2 is on the opposite side in x and y with respect to the first module, which gives the minus sign in front of the second term above. The contribution to the bending of the trajectory in x from the solenoidal field is in the same direction for the electron and the positron, giving the minus sign in front of the constant D_x, while the part belonging to the rotation (constant E_x) between LEP and DELPHI coordinate systems affects the particle trajectories in opposite directions.

The constants A to E in the two equations above, together with the corresponding set of constants for the transformation of the remaining phase space components, define the acceptance in phase space for a pair of diagonal VSAT modules.

The particles that hit the flanges or the material in front of them are discarded in the simulation. Behind the flanges the beam pipe is made of 1.5 *mm* of aluminium, which corresponds to 0.017 r.l., so it is possible that their shower starts when they hit the beam pipe. FASTSIM calculates the thickness of the traversed material and adds it on the front of the module. The difference from real life is then that the angle between the shower products at the module's front face is not taken into account but this

has no significant effect on the analysis [1]. Particle synchrotron radiation in the magnetic fields is also neglected.

6.1.2 The shower parametrization

Once a particle has hit the detector, FASTSIM will simulate the electromagnetic shower which is produced in the module. Both the longitudinal and transverse shower profiles are parametrized to avoid time consuming shower evolutions.

The longitudinal profile parametrization we use is the one determined in [31], where a study was made for a Si/W sandwich calorimeter which contained 24 radiation lengths of tungsten. A silicon detector with 25 cm^2 of active area was located after every two radiation lengths. The energies of the incoming electrons were between 4 and 49 GeV. Only electrons entering the central 0.25 cm^2 region were selected.

The data were fitted by the function

$$\epsilon(t) = \epsilon_0(t/2)^a exp(-bt) + \epsilon_1(t/2)^c exp[-m(t - x_1) - y_1] \tag{6.9}$$

where $\epsilon(t)$ is the detected energy in MeV at depth t, expressed in radiation lengths, ϵ_0 and ϵ_1 are normalization constants in MeV, a, b, c, m, x_1 are dimensionless functions of the incident electron energy and y_1 is a dimensionless constant:

$$a = (3.2 \pm 0.5) + (0.3 \pm 0.2) lnE,$$

$$b = (0.75 \pm 0.10) + (-0.05 \pm 0.04) lnE,$$

$$c = (0.26 \pm 0.10) lnE,$$

$$m = (0.04 \pm 0.02) lnE,$$

$$x_1 = (-6.8 \pm 3.5) + (55.9 \pm 20.3) lnE,$$

$$y_1 = 2.5 \pm 0.4,$$

$$\epsilon_0 = (2.2 \pm 1.2) + (1.5 \pm 0.6) lnE,$$

$$\epsilon_1 = 1\ MeV.$$

The transverse profile parametrization was obtain by fits on VSAT data from the x and y strip planes [32]. The formula reads

$$d(r) = a_1 exp(-r/b_1) + a_2 exp(-r/b_2) \tag{6.10}$$

where $d(r)$ is the detected energy at radius r, expressed in radiation lengths, from the impact point divided by the total energy deposit in the plane, a_1 is a dimensionless function of the depth t in radiation lengths, a_2 is a dimensionless constant and b_1, b_2 are constants in radiation lengths:

$$a_1 = 1.11 exp[-(t - 7)/3.97],$$

$$a_2 = 0.1,$$

$$b_1 = 0.082764\ r.l.,$$

$$b_2 = 0.6168\ r.l..$$

The simulated energy at a certain depth t will then be proportional to the quantity

$$signal(t) = \epsilon(t) \int d(r) dr \tag{6.11}$$

where the integral is calculated over the surface of the FAD plane located at depth t. The sum $\sum_t signal(t)$ over all FADs is proportional to the energy deposited in the module and is the equivalent of the uncalibrated energy of the data.

[1] A detailed description of the beam pipe in FASTSIM can be found in [30].

6.1.3 The accepted cross section

After FASTSIM has calculated the energy and position of the particles that hit the detector, the events are analyzed by the same program we analyze the data with. This program applies the energy and position cuts we described in chapter 4. The result of the program is a sample of accepted Bhabha events like the one represented by the blue points in fig. 4.7. The way we calculate the accepted cross section from these events is the following [32]. BHLUMI generates events according to the Born cross section and then modifies it by adding the radiative corrections. If σ_g is the (differential) Born cross section for a particular event and σ_i is the same cross section with all corrections, a weight $w_i = \sigma_i/\sigma_g$ is assigned to the event. After the event has passed the detector simulation and the experimental cuts we can calculate the average weight for all the accepted events

$$\overline{w} = \frac{\sum_{acc} w_i}{N_{generated}} \tag{6.12}$$

where $N_{generated}$ is the number of generated events. The accepted cross section is then calculated as

$$\sigma_{acc} = \overline{w} \cdot \sigma_{approx}. \tag{6.13}$$

where σ_{approx} is the integrated Born cross section for the kinematical region which was used for the run of BHLUMI.

6.2 Correction of the cross section for beam parameter variations

In order to correct the accepted cross section for the variation of the beam parameters in the 1995 scan, 29 FASTSIM runs were done. In 21 runs the x beamspot and the electron and positron divergences in x were varied. In the remaining 8 runs the electron and positron tilts in y were varied [32]. All runs had 1.2 million generated events, except 9 of the 21 first runs, which had 2 million generated events.

Before correcting the cross section we had to check that the simulation agreed with the data. To this end we compared the distributions of the x and y coordinates of the impact points on the four modules (fig. 6.1). One entry in the plots of fig. 6.1 corresponds to one run of data (i.e. one cassette) or to one run of simulation. One simulation run contains about 40000 accepted Bhabha events, so the FASTSIM distributions are only seemingly of low statistics. The difference in shape between the data and FASTSIM distributions is not a disagreement. It is due to the fact that in our plots we have the mean values of the cassettes and not the distributions of the events themselves. The simulation distributions are flat because we chose to do the same number (one) of runs for each set of beam parameters whereas LEP is running for different time intervals at each such set. Our purpose was to produce simulated spectra which would be at about the same range as the data [32]. The small departures seen have no real influence on the final measurement.

We can now do the correction of our cross section. This is done in terms of variables which are directly measured by the detector as follows [25]. For each FASTSIM run and for each diagonal i we calculate the accepted cross section σ_i and the following variables: $\Delta x_i, R\Delta x_i, \Delta y_i$. We also calculate the asymmetry, A_D. Then the correction for the cross section of diagonal i will be

$$\sigma_i = \sigma_0[1 + a_i(\Delta x_i - \overline{\Delta x_i}) + b_i(\Delta x_i - \overline{\Delta x_i})^2 + c_i(\Delta y_i - \overline{\Delta y_i}) + d_i(R\Delta x_i - \overline{R\Delta x_i}) + e_i(A_D - \overline{A_D})] \tag{6.14}$$

The mean values are those of the entire scan data. σ_0 is treated as an unknown constant. In order to calculate the coefficients (slopes) a_i, b_i, c_i, d_i, e_i we do fits to the corresponding distributions of σ_i. e.g. to calculate c_i we do a linear fit to the distribution of σ_i versus $\Delta y_i - \overline{\Delta y_i}$, etc. The results are given in the Table 6.1 [25]. The small differences between diagonals 1 and 2 are due to small asymmetries in the setup.

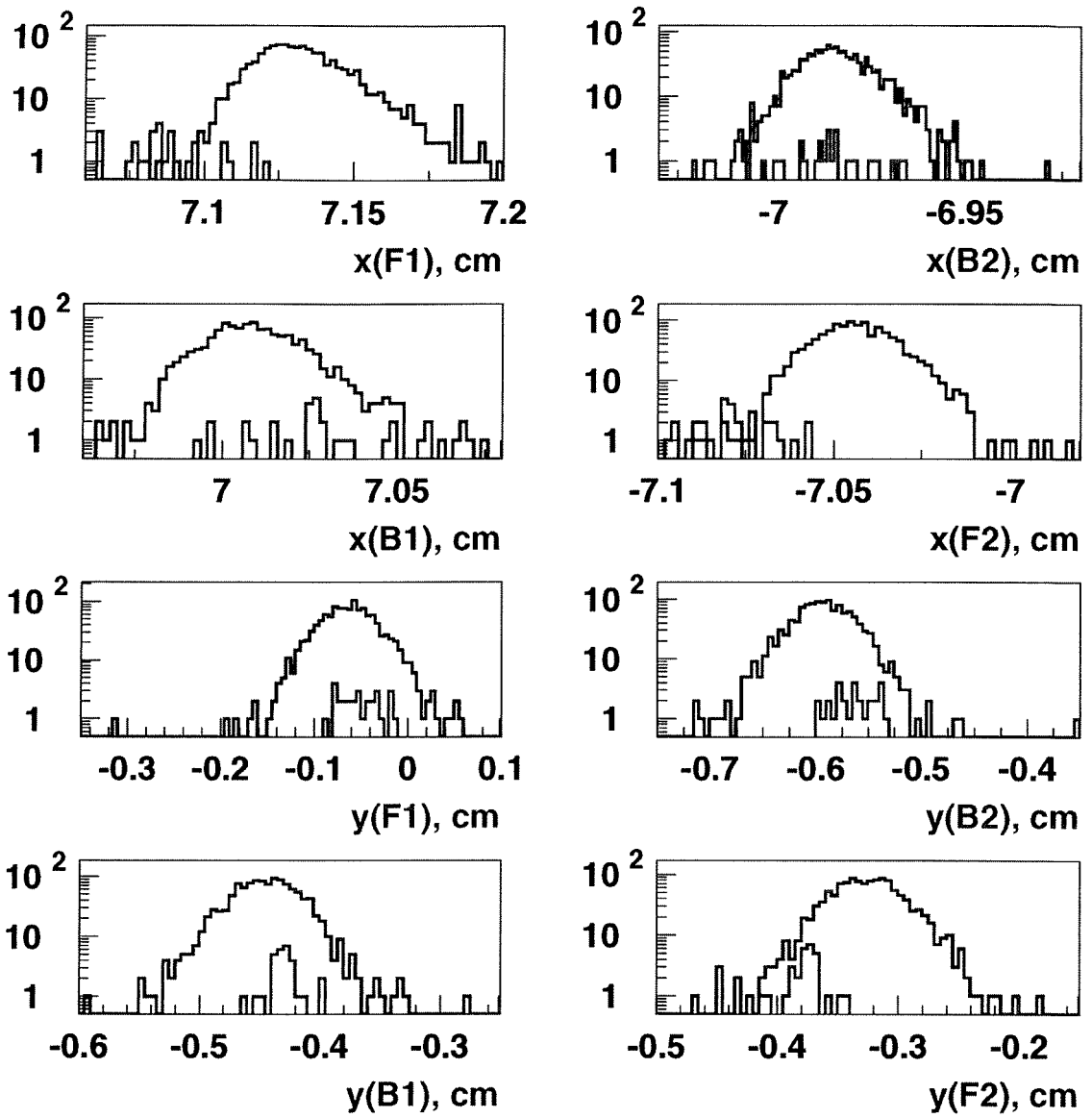

Figure 6.1: *Comparison between data (blue curves) and FASTSIM (red curves) .*

	value for i=1	value for i=2
a_i	0.400 ± 0.030	-0.128 ± 0.020
b_i	1.800 ± 0.700	0.200 ± 0.500
c_i	-0.090 ± 0.030	-0.190 ± 0.030
d_i	0.300 ± 0.100	0.300 ± 0.100
e_i	0.001 ± 0.040	0.001 ± 0.040

Table 6.1: *Slopes for the 1995 scan .*

Chapter 7

Results

7.1 Relative luminosity

According to eq. (6.14), the number of accepted Bhabha events in the data has to be corrected as follows

$$N^j = \frac{N_1^j}{1 + a_1(\Delta x_1^j - \overline{\Delta x_1^j}) + \ldots} + \frac{N_2^j}{1 + a_2(\Delta x_2^j - \overline{\Delta x_2^j}) + \ldots} \tag{7.1}$$

where N^j is the corrected number of events for the j-th cassette, N_i^j is the number of accepted Bhabha events in diagonal i and the denominators contain all the beam parameter corrections that we discussed in the previous chapter. We calculate the VSAT relative luminosity by adjusting the value of σ_0 so that the normalized differences with the STIC luminosity will be close to zero for the total data sample. The results are given in Table 7.1. The first four lines give the VSAT luminosity. Its values for all minibunch numbers, for minibunch one, two and three are given in lines one, two, three and four, respectively. The next four lines give the corresponding values for STIC luminosity. Then the corresponding numbers of VSAT and STIC Bhabha events are mentioned. In the last line of the table, we give the normalized differences (pulls) between VSAT and STIC luminosities for all minubunch numbers. We see that the pulls are acceptable. The values of the third, four and fifth column represent data taken at 45.66 GeV (peak), 44.74 GeV (peak-2) and 46.51 GeV (peak+2), respectively. The quantities in the last column refer to all energies.

In Table 7.2 we give the errors for the VSAT luminosity. The total error is calculated by adding quadratically the statistical error and the systematic error. The systematic error stems from the cross section correction for the beam parameters. For example, the correction for $R\Delta x_1$ is $d_1(R\Delta x_1 - \overline{R\Delta x_1})$, where d_1 is the slope, i.e. the correction factor given by FASTSIM, $R\Delta x_1$ is the value of $R\Delta x_1$ of the cassette currently processed and $\overline{R\Delta x_1}$ is the average value of $R\Delta x_1$ over all scan data. As a consequence, there are two contributions to the error, one due to the error of the slope, which comes from FASTSIM and is called correlated systematic error and the other being the error of $R\Delta x_1$ (depending on the statistics of the cassette) called uncorrelated systematic error. We also state the STIC error for comparison. The total VSAT error is significantly better than the STIC error.

7.2 Z^0 lineshape

In Appendix A we give the DELPHI results on the hadronic cross sections and the cross sections and forward-backward asymmetries in the leptonic channels for the data taken from 1993 to 1995 at the Z^0 peak. The contribution of our analysis, i.e. the measurement of the relative luminosity for the 1995 scan, was to cross check the stability of the STIC luminosity. The STIC and VSAT measurements were not combined, as was done in 1993, for two reasons. First, the statistical STIC error was better than the error of the calorimeter it has replaced (SAT). Second, the VSAT lost a considerable amount of data taken at peak, which shows in the much larger corresponding pull when comparing with 1993 data.

	mb	peak	peak-2	peak+2	total
L^{int}_{VSAT} (nb^{-1})		1752.54	4619.77	5520.35	11892.64
	1	580.63	1628.97	1951.87	4161.47
	2	619.18	1549.52	1870.15	4038.85
	3	550.50	1434.84	1691.23	3676.57
L^{int}_{STIC} (nb^{-1})		1736.78	4640.97	5515.72	11893.46
	1	571.33	1628.97	1948.72	4149.02
	2	614.71	1565.19	1873.14	4053.04
	3	550.21	1445.61	1692.03	3687.85
$Bhabhas_{VSAT}$		612277	1681154	1859281	4152713
	1	202853	592796	657399	1453049
	2	216321	563872	629871	1410065
	3	192327	522148	569616	1284091
$Bhabhas_{STIC}$		95232	266399	290134	651765
	1	31331	93499	102504	227334
	2	33705	89852	98533	222090
	3	30166	82978	89001	202145
Pull		2.47	-2.63	-0.01	-0.66

Table 7.1: *STIC and VSAT luminosities.*

	mb	peak	peak-2	peak+2	total
STATISTICAL (permille)		1.28	0.77	0.73	0.49
	1	2.22	1.30	1.23	0.83
	2	2.15	1.33	1.26	0.84
	3	2.28	1.38	1.33	0.88
UNC. SYSTEMATIC (permille)		0.28	0.17	0.16	0.11
	1	0.50	0.29	0.28	0.18
	2	0.48	0.29	0.28	0.19
	3	0.51	0.31	0.30	0.20
COR. SYSTEMATIC (permille)		0.34	0.42	0.37	0.09
	1	0.41	0.52	0.26	0.22
	2	0.33	0.41	0.49	0.19
	3	0.36	0.43	0.47	0.11
TOT. SYSTEMATIC (permille)		0.44	0.45	0.41	0.14
	1	0.64	0.59	0.38	0.29
	2	0.58	0.50	0.56	0.26
	3	0.62	0.53	0.56	0.22
TOTAL ERROR (permille)		1.35	0.89	0.84	0.51
	1	2.31	1.43	1.29	0.88
	2	2.23	1.42	1.38	0.88
	3	2.36	1.48	1.44	0.91
$error_{STIC}$ (permille)		3.24	1.94	1.85	1.24
	1	5.64	3.27	3.12	2.10
	2	5.44	3.33	3.18	2.12
	3	5.75	3.47	3.35	2.22

Table 7.2: *STIC and VSAT errors.*

Acknowledgements

There are many people I would like to thank because without their help this report would not have been written. I will mention here only a few.

First of all, I would like to thank my supervisors, Giuseppina Rinaudo and Bengt Lörstad, for their guidance, help and support during all the time I have been working with the VSAT. I would also like to thank Gösta Gustafson and Torbjörn Sjöstrand for their patience with my questions about Bhabha scattering and for their help with the coursework. For this latter reason I would also like to thank Anders Irbäck, Erik Sandelin and Henrik Jönsson.

Many thanks are also due to Mikael Eriksson for his help with accelerator physics, to Philippe Charpentier for information on online luminosity, to Vincent Hedberg for information on the STIC and help with data analysis and to Michele Caffo for restoring the program bhabha.for and discussing the corrections with me. I would also like to thank Helmut Burkhardt for allowing me to use figure 2.2. I owe my gratitude to the people that have worked with the VSAT, Per Jonsson, Nikolai Zimin, Henrik Carling, Ulf Mjörnmark, Fabio Cossutti, Andreas Nygren and Björn Lundberg for their collaboration and friendship. Sverker Almehed deserves a special mention for answering endless questions about the simulation and the analysis in general. I would also like to thank Jean-Paul Chavanel for his help with our vax disks.

Lastly, I would like to thank Oxana Smirnova for being a great friend and helping practically with everything. I owe my deepest gratitude to my parents for their unfailing help and support, without which this work would not have been possible.

Bibliography

[1] S. Myers, *The LEP collider*, excerpts from The John Adams Memorial Lecture, CERN, 26 November 1990.

[2] T. Camporesi et al., *Luminosity Measurement in 1994 with the STIC detector*, DELPHI 97-08 PHYS 667.

[3] M. Paganoni et al., *Energy and position reconstruction in the DELPHI Small Angle Tile Calorimeter*, DELPHI 97-07 PHYS 666.

[4] E. Falk et al., *Simulation of Off-Energy Electron Background in DELPHI*, DELPHI 97-12 LEDI 8.

[5] E. Falk et al., *Photon Analysis with STIC*, DELPHI note in preparation.

[6] Ch. Jarlskog, *Interaction point estimation and beam parameter variations in DELPHI with the VSAT*, LUNFD6/(NFFL-7110)1995.

[7] K. Potter, *Luminosity measurements and calculations*, CERN Accelerator School 1992, CERN 94-01.

[8] H. Wiedemann, *Particle Accelerator Physics*, Springer-Verlag 1993, chapter 12.

[9] A. Håkansson, *Luminosity Measurement at LEP using the Very Small Angle Tagger of DELPHI*, PhD thesis, LUNFD6/(NFFL-7077) 1993.

[10] F. M. Renard, *Basics of Electron Positron Collisions*, éditions Frontières, 1981.

[11] D. H. Perkins, *Introduction to High Energy Physics*, Addison-Wesley, 1987, chapter 2.

[12] H. Wiedemann, *Particle Accelerator Physics*, Springer-Verlag 1993, chapter 7.

[13] P. M. Jonsson, *Luminosity Measurements and Two-Photon Physics with the DELPHI VSAT at LEP*, PhD thesis, LUNFD6/(NFFL-7152) 1998.

[14] S. J. Alvsvaag at al., *The system for online monitoring of LEP beam background and luminosity at the DELPHI interaction point*, DELPHI 93-3 DAS 137.

[15] *Bhabha Scattering* in *Z Physics at LEP 1*, volume 1, CERN 98-08, convenors M. Caffo and E. Remiddi.

[16] M. Caffo, private communication.

[17] *Electroweak radiative corrections for Z physics* in *Z Physics at LEP 1*, volume 1, CERN 98-08, convenors M. Consoli and W. Hollik.

[18] M. Greco, *Bhabha scattering near the Z^0*, Physics Letters B **177** (1986) 97-105.

[19] M. Caffo et al., *Hard collinear photons, high-energy radiative corrections to Bhabha scattering*, Nuclear Physics **B252** (1985) 378-388.

[20] M. Böhm et al., *Radiative corrections to Bhabha scattering at high energies (I)*, Nuclear Physics **B304** (1988) 687-711.

[21] U. Mjörnmark, private communication.

[22] Ch. Jarlskog, *VSAT Off-line Minibunch Tagging for the 1995 Scan*, LUNFD6/(NFFL-7154) 1998, internal report in preparation.

[23] Ch. Jarlskog, *VSAT energy calibration for 1995 minibunch data*, LUNFD6/(NFFL-7129) 1996.

[24] I. Kronkvist, *Data Base and Slow Controls System of the DELPHI VSAT and Two-Photon Physics using DELPHI at LEP* , PhD thesis, LUNFD6/(NFFL-7128) 1996.

[25] G. Rinaudo, private communication.

[26] S. Almehed at al., *Measurement of the beam parameter variations in DELPHI with the VSAT*, DELPHI 95-150 LEDI 2.

[27] Ch. Jarlskog, *Beam Parameter Analysis for the VSAT* , LUNFD6/(NFFL-7145) 1997.

[28] S. Almehed et al., *High precision relative luminosity measurement with a Very Small Angle Tagger (VSAT) in DELPHI*, DELPHI 92-77 PHYS 188.

[29] S. Jadach et al., *Multiphoton Monte Carlo event generator for Bhabha scattering at small angles*, Phys. Rev. D, **40**, 3582, 1989.

[30] I. Kronkvist, *FASTSIM examination on how different LEP beam parameters affect the acceptance of the VSAT detector* , LUNFD6/(NFFL-7061) 1990.

[31] G. Barbiellini et al., *Energy resolution and longitudinal shower development in a Si/W electromagnetic calorimeter* , NIM A235 (1985) 55-60.

[32] S. Almehed, private communication.

List of Figures

Appendix A

Cross Sections and Leptonic Forward-Backward Asymmetries from the Z^0 Running of LEP

EUROPEAN ORGANIZATION FOR NUCLEAR RESEARCH

CERN–EP/Paper190/Draft2

7 July 1998

Cross Sections and Leptonic Forward–Backward Asymmetries from the Z^0 Running of LEP

DELPHI Collaboration

Abstract

During 1993 and 1995 LEP was run at 3 energies near the Z^0 peak in order to give improved measurements of the mass and width of the resonance. DELPHI accumulated data corresponding to integrated luminosities of approximately 36 pb^{-1} in 1993 and 34 pb^{-1} in 1995. During 1994, LEP operated only at the Z^0 peak and DELPHI recorded data corresponding to an integrated luminosity of approximately 46 pb^{-1}. For the 1994 and 1995 running a new luminosity monitor with significantly smaller systematic errors was available. Analyses on the hadronic cross-sections and the cross-sections and forward–backward asymmetries in the leptonic channels used the most precise evaluations of the LEP energies. In the dimuon channel events with an initial state radiation photon have been used to probe the cross-sections and asymmetries down to PETRA energies. Model independent fits to all DELPHI lineshape and asymmetry data from 1990 to 1995 have been carried out and give values of the resonance parameters with significantly smaller errors than previously published. The results are interpreted in terms of the Standard Model.

(To be submitted to E. Phys. J. C)
Send comments up to 22/07/1998 to
g.myatt1@physics.oxford.ac.uk,klaus.monig@cern.ch,
Clara.Matteuzzi@cern.ch,Dimartino@vxdel1.cern.ch

P.Abreu[21], W.Adam[50], T.Adye[36], P.Adzic[11], G.D.Alekseev[16], R.Alemany[49], P.P.Allport[22], S.Almehed[24], U.Amaldi[9], S.Amato[47], E.G.Anassontzis[3], P.Andersson[44], A.Andreazza[9], P.Antilogus[25], W-D.Apel[17], Y.Arnoud[14], B.Åsman[44], J-E.Augustin[25], A.Augustinus[9], P.Baillon[9], P.Bambade[19], F.Barao[21], R.Barbier[25], D.Y.Bardin[16], G.Barker[9], A.Baroncelli[38], M.Battaglia[15], M.Baubillier[23], K-H.Becks[52], M.Begalli[6], P.Beilliere[8], Yu.Belokopytov[9,53], A.C.Benvenuti[5], C.Berat[14], M.Berggren[25], D.Bertini[25], D.Bertrand[2], M.Besancon[39], F.Bianchi[45], M.Bigi[45], M.S.Bilenky[16], M-A.Bizouard[19], D.Bloch[10], M.Bonesini[27], W.Bonivento[27], M.Boonekamp[39], P.S.L.Booth[22], A.W.Borgland[4], G.Borisov[39], C.Bosio[41], O.Botner[48], E.Boudinov[30], B.Bouquet[19], C.Bourdarios[19], T.J.V.Bowcock[22], I.Boyko[16], I.Bozovic[11], M.Bozzo[13], P.Branchini[38], T.Brenke[52], R.A.Brenner[48], P.Bruckman[35], J-M.Brunet[8], L.Bugge[32], T.Buran[32], T.Burgsmueller[52], P.Buschmann[52], S.Cabrera[49], M.Caccia[27], M.Calvi[27], A.J.Camacho Rozas[40], T.Camporesi[9], V.Canale[37], M.Canepa[13], F.Carena[9], L.Carroll[22], C.Caso[13], M.V.Castillo Gimenez[49], A.Cattai[9], F.R.Cavallo[5], Ch.Cerruti[10], V.Chabaud[9], M.Chapkin[42], Ph.Charpentier[9], L.Chaussard[25], P.Checchia[35], G.A.Chelkov[16], M.Chen[2], R.Chierici[45], P.Chliapnikov[42], P.Chochula[7], V.Chorowicz[25], J.Chudoba[29], P.Collins[9], M.Colomer[49], R.Contri[13], E.Cortina[49], G.Cosme[19], F.Cossutti[39], J-H.Cowell[22], H.B.Crawley[1], D.Crennell[36], G.Crosetti[13], J.Cuevas Maestro[33], S.Czellar[15], B.Dalmagne[19], G.Damgaard[28], M.Davenport[9], W.Da Silva[23], A.Deghorain[2], G.Della Ricca[46], P.Delpierre[26], N.Demaria[9], A.De Angelis[9], W.De Boer[17], S.De Brabandere[2], C.De Clercq[2], B.De Lotto[46], A.De Min[35], L.De Paula[47], H.Dijkstra[9], L.Di Ciaccio[37], A.Di Diodato[37], A.Djannati[8], J.Dolbeau[8], K.Doroba[51], M.Dracos[10], J.Drees[52], K.-A.Drees[52], M.Dris[31], A.Duperrin[25], J-D.Durand[25,9], R.Ehret[17], G.Eigen[4], T.Ekelof[48], G.Ekspong[44], M.Ellert[48], M.Elsing[9], J-P.Engel[10], B.Erzen[43], M.Espirito Santo[21], E.Falk[24], G.Fanourakis[11], D.Fassouliotis[11], J.Fayot[23], M.Feindt[17], A.Fenyuk[42], P.Ferrari[27], A.Ferrer[49], S.Fichet[23], A.Firestone[1], P.-A.Fischer[9], U.Flagmeyer[52], H.Foeth[9], E.Fokitis[31], F.Fontanelli[13], B.Franek[36], A.G.Frodesen[4], R.Fruhwirth[50], F.Fulda-Quenzer[19], J.Fuster[49], A.Galloni[22], D.Gamba[45], M.Gandelman[47], C.Garcia[49], J.Garcia[40], C.Gaspar[9], M.Gaspar[47], U.Gasparini[35], Ph.Gavillet[9], E.N.Gazis[31], D.Gele[10], J-P.Gerber[10], L.Gerdyukov[42], N.Ghodbane[25], I.Gil[49], F.Glege[52], R.Gokieli[51], B.Golob[43], P.Goncalves[21], I.Gonzalez Caballero[40], G.Gopal[36], L.Gorn[1,54], M.Gorski[51], Yu.Gouz[42], V.Gracco[13], J.Grahl[1], E.Graziani[38], C.Green[22], A.Grefrath[52], P.Gris[39], K.Grzelak[51], M.Gunther[48], J.Guy[36], F.Hahn[9], S.Hahn[52], S.Haider[9], A.Hallgren[48], K.Hamacher[52], F.J.Harris[34], V.Hedberg[24], S.Heising[17], R.Henriques[21], J.J.Hernandez[49], P.Herquet[2], H.Herr[9], T.L.Hessing[34], J.-M.Heuser[52], E.Higon[49], S-O.Holmgren[44], P.J.Holt[34], D.Holthuizen[30], S.Hoorelbeke[2], M.Houlden[22], J.Hrubec[50], K.Huet[2], K.Hultqvist[44], J.N.Jackson[22], R.Jacobsson[44], P.Jalocha[9], R.Janik[7], Ch.Jarlskog[24], G.Jarlskog[24], P.Jarry[39], B.Jean-Marie[19], E.K.Johansson[44], P.Jonsson[24], C.Joram[9], P.Juillot[10], F.Kapusta[23], K.Karafasoulis[11], S.Katsanevas[25], E.C.Katsoufis[31], R.Keranen[17], B.A.Khomenko[16], N.N.Khovanski[16], A.Kiiskinen[15], B.King[22], N.J.Kjaer[30], O.Klapp[52], H.Klein[9], P.Kluit[30], D.Knoblauch[17], P.Kokkinias[11], A.Konopliannikov[42], M.Koratzinos[9], V.Kostioukhine[42], C.Kourkoumelis[3], O.Kouznetsov[16], M.Krammer[50], C.Kreuter[9], E.Kriznic[43], J.Krstic[11], Z.Krumstein[16], P.Kubinec[7], W.Kucewicz[18], K.Kurvinen[15], J.W.Lamsa[1], L.Lanceri[46], D.W.Lane[1], P.Langefeld[52], V.Lapin[42], J-P.Laugier[39], R.Lauhakangas[15], G.Leder[50], F.Ledroit[14], V.Lefebure[2], L.Leinonen[44], A.Leisos[11], R.Leitner[29], J.Lemonne[2], G.Lenzen[52], V.Lepeltier[19], T.Lesiak[18], M.Lethuillier[39], J.Libby[34], D.Liko[9], A.Lipniacka[44], I.Lippi[35], B.Loerstad[24], M.Lokajicek[12], J.G.Loken[34], J.H.Lopes[47], J.M.Lopez[40], R.Lopez-Fernandez[14], D.Loukas[11], P.Lutz[39], L.Lyons[34], J.MacNaughton[50], J.R.Mahon[6], A.Maio[21], A.Malek[52], T.G.M.Malmgren[44], V.Malychev[16], F.Mandl[50], J.Marco[40], R.Marco[40], B.Marechal[47], M.Margoni[35], J-C.Marin[9], C.Mariotti[9], A.Markou[11], C.Martinez-Rivero[33], F.Martinez-Vidal[49], S.Marti i Garcia[22], N.Mastroyiannopoulos[11], F.Matorras[40], C.Matteuzzi[27], G.Matthiae[37], J.Mazik[29], F.Mazzucato[35], M.Mazzucato[35], M.Mc Cubbin[22], R.Mc Kay[1], R.Mc Nulty[9], G.Mc Pherson[22], C.Meroni[27], E.Migliore[45], L.Mirabito[25], W.A.Mitaroff[50], U.Mjoernmark[24], T.Moa[44], R.Moeller[28], K.Moenig[9], M.R.Monge[13], X.Moreau[23], P.Morettini[13], G.Morton[34], K.Muenich[52], M.Mulders[30], C.Mulet-Marquis[14], R.Muresan[24], W.J.Murray[36], B.Muryn[14,18], G.Myatt[34], T.Myklebust[32], F.Naraghi[14], F.L.Navarria[5], S.Navas[49], K.Nawrocki[51], P.Negri[27], N.Neufeld[9], W.Neumann[52], N.Neumeister[50], R.Nicolaidou[14], B.S.Nielsen[28], M.Nieuwenhuizen[30], V.Nikolaenko[10], M.Nikolenko[10,16], V.Nomokonov[15], A.Normand[22], A.Nygren[24], V.Obraztsov[42], A.G.Olshevski[16], A.Onofre[21], R.Orava[15], G.Orazi[10], K.Osterberg[15], A.Ouraou[39], P.Paganini[19], M.Paganoni[27], S.Paiano[5], R.Pain[23], R.Paiva[21], J.Palacios[34], H.Palka[18], Th.D.Papadopoulou[31], K.Papageorgiou[11], L.Pape[9], C.Parkes[34], F.Parodi[13], U.Parzefall[22], A.Passeri[38], M.Pegoraro[35], L.Peralta[21], M.Pernicka[50], A.Perrotta[5], C.Petridou[46], A.Petrolini[13], H.T.Phillips[36], G.Piana[13], F.Pierre[39], M.Pimenta[21], E.Piotto[27], T.Podobnik[43], M.E.Pol[6], G.Polok[18], P.Poropat[46], V.Pozdniakov[16], P.Privitera[37], N.Pukhaeva[16], A.Pullia[27], D.Radojicic[34], S.Ragazzi[27], H.Rahmani[31], D.Rakoczy[50], P.N.Ratoff[20], A.L.Read[32], P.Rebecchi[9], N.G.Redaelli[27], M.Regler[50], D.Reid[9], R.Reinhardt[52], P.B.Renton[34], L.K.Resvanis[3], F.Richard[19], J.Ridky[12], G.Rinaudo[45], O.Rohne[32], A.Romero[45], P.Ronchese[35], E.I.Rosenberg[1], P.Rosinsky[7], P.Roudeau[19], T.Rovelli[5], V.Ruhlmann-Kleider[39], A.Ruiz[40], H.Saarikko[15], Y.Sacquin[39], A.Sadovsky[16], G.Sajot[14], J.Salt[49], D.Sampsonidis[11], M.Sannino[13], H.Schneider[17], Ph.Schwemling[23], U.Schwickerath[17], M.A.E.Schyns[52], F.Scuri[46], P.Seager[20], Y.Sedykh[16], A.M.Segar[34], R.Sekulin[36], R.C.Shellard[6], A.Sheridan[22], R.Silvestre[39], L.Simard[39], F.Simonetto[35], A.N.Sisakian[16], T.B.Skaali[32], G.Smadja[25], O.Smirnova[24], G.R.Smith[36], A.Sopczak[17], R.Sosnowski[51], T.Spassov[21], E.Spiriti[38], P.Sponholz[52], S.Squarcia[13], D.Stampfer[50], C.Stanescu[38], S.Stanic[43], S.Stapnes[32], K.Stevenson[34], A.Stocchi[19], J.Strauss[50], R.Strub[10], B.Stugu[4], M.Szczekowski[51], M.Szeptycka[51], T.Tabarelli[27], F.Tegenfeldt[48], F.Terranova[27], J.Thomas[34], A.Tilquin[26], J.Timmermans[30], L.G.Tkatchev[16], T.Todorov[10], S.Todorova[10],

D.Z.Toet[30], A.Tomaradze[2], A.Tonazzo[27], L.Tortora[38], G.Transtromer[24], D.Treille[9], G.Tristram[8], A.Trombini[19], C.Troncon[27], A.Tsirou[9], M-L.Turluer[39], I.A.Tyapkin[16], S.Tzamarias[11], B.Ueberschaer[52], O.Ullaland[9], V.Uvarov[42], G.Valenti[5], E.Vallazza[46], C.Vander Velde[2], G.W.Van Apeldoorn[30], P.Van Dam[30], W.K.Van Doninck[2], J.Van Eldik[30], A.Van Lysebetten[2], I.Van Vulpen[30], N.Vassilopoulos[34], G.Vegni[27], L.Ventura[35], W.Venus[36], F.Verbeure[2], M.Verlato[35], L.S.Vertogradov[16], V.Verzi[37], D.Vilanova[39], L.Vitale[46], E.Vlasov[42], A.S.Vodopyanov[16], G.Voulgaris[3], V.Vrba[12], H.Wahlen[52], C.Walck[44], C.Weiser[17], A.M.Wetherell[9], D.Wicke[52], J.H.Wickens[2], G.R.Wilkinson[9], M.Winter[10], M.Witek[18], T.Wlodek[19], G.Wolf[9], J.Yi[1], O.Yushchenko[42], A.Zaitsev[42], A.Zalewska[18], P.Zalewski[51], D.Zavrtanik[43], E.Zevgolatakos[11], N.I.Zimin[16,24], G.C.Zucchelli[44], G.Zumerle[35]

[1]Department of Physics and Astronomy, Iowa State University, Ames IA 50011-3160, USA
[2]Physics Department, Univ. Instelling Antwerpen, Universiteitsplein 1, BE-2610 Wilrijk, Belgium
and IIHE, ULB-VUB, Pleinlaan 2, BE-1050 Brussels, Belgium
and Faculté des Sciences, Univ. de l'Etat Mons, Av. Maistriau 19, BE-7000 Mons, Belgium
[3]Physics Laboratory, University of Athens, Solonos Str. 104, GR-10680 Athens, Greece
[4]Department of Physics, University of Bergen, Allégaten 55, NO-5007 Bergen, Norway
[5]Dipartimento di Fisica, Università di Bologna and INFN, Via Irnerio 46, IT-40126 Bologna, Italy
[6]Centro Brasileiro de Pesquisas Físicas, rua Xavier Sigaud 150, BR-22290 Rio de Janeiro, Brazil
and Depto. de Física, Pont. Univ. Católica, C.P. 38071 BR-22453 Rio de Janeiro, Brazil
and Inst. de Física, Univ. Estadual do Rio de Janeiro, rua São Francisco Xavier 524, Rio de Janeiro, Brazil
[7]Comenius University, Faculty of Mathematics and Physics, Mlynska Dolina, SK-84215 Bratislava, Slovakia
[8]Collège de France, Lab. de Physique Corpusculaire, IN2P3-CNRS, FR-75231 Paris Cedex 05, France
[9]CERN, CH-1211 Geneva 23, Switzerland
[10]Institut de Recherches Subatomiques, IN2P3 - CNRS/ULP - BP20, FR-67037 Strasbourg Cedex, France
[11]Institute of Nuclear Physics, N.C.S.R. Demokritos, P.O. Box 60228, GR-15310 Athens, Greece
[12]FZU, Inst. of Phys. of the C.A.S. High Energy Physics Division, Na Slovance 2, CZ-180 40, Praha 8, Czech Republic
[13]Dipartimento di Fisica, Università di Genova and INFN, Via Dodecaneso 33, IT-16146 Genova, Italy
[14]Institut des Sciences Nucléaires, IN2P3-CNRS, Université de Grenoble 1, FR-38026 Grenoble Cedex, France
[15]Helsinki Institute of Physics, HIP, P.O. Box 9, FI-00014 Helsinki, Finland
[16]Joint Institute for Nuclear Research, Dubna, Head Post Office, P.O. Box 79, RU-101 000 Moscow, Russian Federation
[17]Institut für Experimentelle Kernphysik, Universität Karlsruhe, Postfach 6980, DE-76128 Karlsruhe, Germany
[18]Institute of Nuclear Physics and University of Mining and Metalurgy, Ul. Kawiory 26a, PL-30055 Krakow, Poland
[19]Université de Paris-Sud, Lab. de l'Accélérateur Linéaire, IN2P3-CNRS, Bât. 200, FR-91405 Orsay Cedex, France
[20]School of Physics and Chemistry, University of Lancaster, Lancaster LA1 4YB, UK
[21]LIP, IST, FCUL - Av. Elias Garcia, 14-1°, PT-1000 Lisboa Codex, Portugal
[22]Department of Physics, University of Liverpool, P.O. Box 147, Liverpool L69 3BX, UK
[23]LPNHE, IN2P3-CNRS, Univ. Paris VI et VII, Tour 33 (RdC), 4 place Jussieu, FR-75252 Paris Cedex 05, France
[24]Department of Physics, University of Lund, Sölvegatan 14, SE-223 63 Lund, Sweden
[25]Université Claude Bernard de Lyon, IPNL, IN2P3-CNRS, FR-69622 Villeurbanne Cedex, France
[26]Univ. d'Aix - Marseille II - CPP, IN2P3-CNRS, FR-13288 Marseille Cedex 09, France
[27]Dipartimento di Fisica, Università di Milano and INFN, Via Celoria 16, IT-20133 Milan, Italy
[28]Niels Bohr Institute, Blegdamsvej 17, DK-2100 Copenhagen Ø, Denmark
[29]NC, Nuclear Centre of MFF, Charles University, Areal MFF, V Holesovickach 2, CZ-180 00, Praha 8, Czech Republic
[30]NIKHEF, Postbus 41882, NL-1009 DB Amsterdam, The Netherlands
[31]National Technical University, Physics Department, Zografou Campus, GR-15773 Athens, Greece
[32]Physics Department, University of Oslo, Blindern, NO-1000 Oslo 3, Norway
[33]Dpto. Fisica, Univ. Oviedo, Avda. Calvo Sotelo s/n, ES-33007 Oviedo, Spain
[34]Department of Physics, University of Oxford, Keble Road, Oxford OX1 3RH, UK
[35]Dipartimento di Fisica, Università di Padova and INFN, Via Marzolo 8, IT-35131 Padua, Italy
[36]Rutherford Appleton Laboratory, Chilton, Didcot OX11 OQX, UK
[37]Dipartimento di Fisica, Università di Roma II and INFN, Tor Vergata, IT-00173 Rome, Italy
[38]Dipartimento di Fisica, Università di Roma III and INFN, Via della Vasca Navale 84, IT-00146 Rome, Italy
[39]DAPNIA/Service de Physique des Particules, CEA-Saclay, FR-91191 Gif-sur-Yvette Cedex, France
[40]Instituto de Fisica de Cantabria (CSIC-UC), Avda. los Castros s/n, ES-39006 Santander, Spain
[41]Dipartimento di Fisica, Università degli Studi di Roma La Sapienza, Piazzale Aldo Moro 2, IT-00185 Rome, Italy
[42]Inst. for High Energy Physics, Serpukov P.O. Box 35, Protvino, (Moscow Region), Russian Federation
[43]J. Stefan Institute, Jamova 39, SI-1000 Ljubljana, Slovenia and Department of Astroparticle Physics, School of Environmental Sciences, Kostanjeviska 16a, Nova Gorica, SI-5000 Slovenia,
and Department of Physics, University of Ljubljana, SI-1000 Ljubljana, Slovenia
[44]Fysikum, Stockholm University, Box 6730, SE-113 85 Stockholm, Sweden
[45]Dipartimento di Fisica Sperimentale, Università di Torino and INFN, Via P. Giuria 1, IT-10125 Turin, Italy
[46]Dipartimento di Fisica, Università di Trieste and INFN, Via A. Valerio 2, IT-34127 Trieste, Italy
and Istituto di Fisica, Università di Udine, IT-33100 Udine, Italy
[47]Univ. Federal do Rio de Janeiro, C.P. 68528 Cidade Univ., Ilha do Fundão BR-21945-970 Rio de Janeiro, Brazil
[48]Department of Radiation Sciences, University of Uppsala, P.O. Box 535, SE-751 21 Uppsala, Sweden
[49]IFIC, Valencia-CSIC, and D.F.A.M.N., U. de Valencia, Avda. Dr. Moliner 50, ES-46100 Burjassot (Valencia), Spain
[50]Institut für Hochenergiephysik, Österr. Akad. d. Wissensch., Nikolsdorfergasse 18, AT-1050 Vienna, Austria
[51]Inst. Nuclear Studies and University of Warsaw, Ul. Hoza 69, PL-00681 Warsaw, Poland
[52]Fachbereich Physik, University of Wuppertal, Postfach 100 127, DE-42097 Wuppertal, Germany
[53]On leave of absence from IHEP Serpukhov
[54]Now at University of Florida

1 Introduction

This paper reports on analyses of the fermion-antifermion pair production cross-sections and the leptonic forward–backward asymmetries with the DELPHI data taken during the LEP energy scans of 1993 and 1995, and in 1994 when LEP operated at a single energy near the Z^0 peak. In 1993 and 1995 LEP operated at the peak energy and at 1.76 GeV above and below (the so–called "peak$\pm$2"points). Before the scans with carefully monitored energies commenced, data was taken at the peak (the "pre–scan" points). Combining these data with DELPHI results from previous years, allowed values of the Z^0 resonance parameters to be determined with significantly smaller errors than those previously published by DELPHI [1,2]. Lineshape and asymmetry measurements, such as those reported here, constitute major inputs to the tests of the Standard Model and to the determination of its parameters.

This paper is organised as follows. In section 2 we give a brief account of the LEP energy determinations. In section 3 the principal components of the DELPHI detector which are relevant for this analysis are presented, and in section 4 the determinations of the luminosity are described. In section 5 the measurements of the hadronic cross-sections are described, and in sections 6, 7 and 8 the cross-sections and forward–backward asymmetries in the leptonic channels are presented. The $\mu^+\mu^-$ events with a hard initial state photon have been analysed to give measurements of the cross-sections and forward backward asymmetries at centre–of–mass energies between 20 and 87 GeV, and these results are presented in section 9. In section 10 the fits to the data reported here, and all previous DELPHI lineshape and asymmetry data are described and in section 11 the results are interpreted within the framework of the Standard Model. Section 12 contains a summary of the results.

2 Determination of the LEP Energies

Since 1993 the energies of the LEP beams have been routinely measured by resonant depolarization [3] performed typically at the end of a physics fill. Table 1 shows the amount of data for each year collected during fills where the energy was directly measured at the end. Given that the measurements could not be done for every fill and that they had not been performed under the conditions used for data taking (separated beams and special orbit tuning) a model of the energy behaviour was necessary to provide the experimental energy. This model has to account for the variation of energy during a fill for the calibrated fills and between fills for the fills which were not calibrated at the end. The model has been developed by the Working Group on LEP Energy [4,5] and a file is provided with the estimate for the LEP centre–of–mass energy at the DELPHI interaction point every 15 minutes. This is in turn converted within DELPHI to an average energy per cassette of raw data.

The model comprises all known sources of variation of the LEP transverse magnetic field, changes of the size of the LEP ring and accelerator effects which can affect the centre-of-mass energies.

The understanding of tidal deformations of the LEP ring is well established. The puzzling variations of the LEP energy over a period of weeks which were first observed in 1993 are now controlled and corrected for by the system of Beam Orbit Monitors of LEP and understood in term of geological stresses of the LEP tunnel due to the pressure of the water table and of the effect of the weight of the Geneva Lake on the earth surrounding the LEP ring. In 1995 new Nuclear Magnetic Resonance probes were installed in two dipoles

in the LEP tunnel allowing for the first time a direct monitoring of the magnetic field seen by the beam. Also in 1995 resonant depolarization measurements were attempted routinely at the end of each physics fill. The 6 fills calibrated both at the beginning and at the end showed an unsuspected drift of the beam energy: typically of a few MeV. This effect was also monitored continously with the NMR probes. The understanding of the energy behaviour of the LEP beams was greatly improved by the ensuing studies. The temperature dependence of the dipole field was studied in great detail in the laboratory indicating a non-linear behaviour more complex than expected. A fluctuating parasitic current of typical magnitude 1A was detected on the beam pipe: a series of experiments identified the source as the leakage from the tracks of a nearby railway line. In 1993 and 1994 LEP worked in pretzel mode with 8 bunches per beam[1] while in 1995 LEP operated with 4 trains of up to 4 bunches each separated by less than 70m. In this latter mode of operation the unwanted collisions on either side of each interaction point were avoided by separating the beams in the vertical plane. This vertical separation caused a finite vertical dispersion[2] of opposite sign for each beam. In such situation if the two opposite beams cross with a finite vertical offset a systematic shift of the centre–of–mass energy can occur. These effects have been foreseen and measures taken to maintain them at negligible levels [5]. In 1995, in parallel with the energy scan, LEP started the commissioning of the first complement of Superconductive Radiofrequency Cavities installed to increase the LEP energy. A new model of the RF corrections was developed accordingly; the RF corrections to the centre–of–mass energies in DELPHI are of the order of 1 MeV with a total error well below 1 MeV [5].

The model is built in a way that the knowledge accumulated in 1995 could be fedback and used to estimate the energy also for 1994 and 1993 [5]. The energies for the bulk of the data collected at the peak in 1994 are known with accuracy comparable to those of the scan data of 1993 and 1995, due to the relatively high number of calibrations performed. There are datasets collected either before the start of the scan in 1993 and 1995 or in special accelerator conditions at the end of 1994 where the determination of the energy was more difficult due to incomplete records of the accelerator conditions. For these periods an overall centre-of-mass energy uncertainty, typically around 20 MeV, was estimated. For earlier years when the amount of information recorded was small the published analysis [6] and its conservatively estimated errors are still adequate.

The various contributions to the uncertainties on the energy estimates are correlated at different levels between years and energy points. In general high correlation between the energy points translates into important error contributions to M_Z whereas low level of correlation between off-peak points contributes to the error on Γ_Z. The most important error on M_Z (varying from $\approx \pm 2.5$ MeV for 1993 to $\approx \pm 1$ MeV in 1995) comes from the uncertainty on the modelling of the energy rise during a fill. The largest error contribution for Γ_Z ($\approx \pm 1$ MeV) comes from the fill to fill normalization.

The net effect of the LEP energy uncertainties and their correlations is to give systematic errors, common between the LEP experiments, of ± 1.8 MeV on the mass and ± 1.1 MeV on the width of the resonance, when data from all years and all experiments are combined. The rms energy spread of the beams has been determined [5] empirically to be about 55 MeV and all cross-sections reported here have been corrected for this effect.

[1] The unwanted collisions in the middle of the LEP circular sections were avoided by setting the beams into a pretzel-like oscillation in the horizontal plane

[2] Spatial ordering of particles according to their momentum

3 The DELPHI Detector

A detailed description of the DELPHI apparatus and its performance can be found in refs. [7,8]. For the present analysis the following parts of the detector are relevant:

- for the measurement of charged particles the Microvertex Detector (VD), the Inner Detector (ID), the Time Projection Chamber (TPC), the Outer Detector(OD) and the Forward Chambers A and B (FCA and FCB). For the 1995 running a lengthened Inner Detector was installed. The polar angle[3] coverage was thereby extended from $23° < \theta < 157°$ to $15° < \theta < 165°$ with a corresponding increase in forward tracking efficiency;
- for the measurement of electromagnetic energy the High-density Projection Chamber (HPC) and the Forward Electromagnetic Calorimeter (FEMC); these detectors were also used for identifying minimum ionizing particles;
- for the measurement of the hadronic energy and muon identification the Hadron Calorimeter (HCAL), which covered both the barrel and endcap regions;
- for muon identification the barrel (MUB) and endcap (MUF), and from the latter part of 1994 onwards, the newly installed and commissioned surround muon chambers (SMC), which complete the polar coverage between barrel and endcap;
- for the trigger, besides the detectors mentioned above, the barrel Time of Flight counters (TOF), the endcap scintillators (HOF) and a scintillator layer embedded in the HPC;
- for the measurement of luminosity (Section 4) the Small Angle Tagger (SAT) and the Very Small Angle Tagger (VSAT) were used in 1993. For the 1994 and later running the SAT was replaced by the Small Angle TIle Calorimeter (STIC).

Data were only accepted for the different measurements when the parts of the detector crucial to them were operating efficiently. Details of the requirements are given in the relevant sections.

The response of the detector to physics processes was modelled using the simulation program DELSIM [8], which incorporates the resolution, granularity and efficiency of the detector components. The event generators chosen for each process are described in the relevant sections of this paper. Simulated data were passed through the same reconstruction and analysis chains as the real data.

4 Determination of the Luminosity

The absolute measurement of the luminosity in 1993 was based on the SAT calorimeter, but the relative luminosity at the off–peak points was taken from the VSAT data, thus making a significant reduction in the statistical errors on the cross-sections. For the 1994 and 1995 running the STIC replaced the SAT.

4.1 The SAT Measurement

The SAT luminosity measurement was based on the observation of small angle Bhabha scattering in calorimeters consisting of lead sheets and plastic scintillating fibres, covering the polar angle range from 43 to 135 mrad. The fiducial volume was accurately defined

[3] The DELPHI coordinate system has the z-axis aligned along the electron beam direction, the x-axis points toward the centre of LEP and the y-axis is vertical. R is used to measure the radius in the (x, y) plane. The polar angle θ is measured with respect to the z-axis and the azimuthal angle ϕ is about z.

by a precisely machined tungsten mask in front of one of the calorimeters. Due to the narrow width of the transition region from 0 to 85% energy deposition, about 100 μm, a simple energy cut corresponds to the geometrical region covered by the mask. A second mask (the "ϕ mask") covered the junction in the vertical plane of the two halves of the masked calorimeter.

For the 1993 running the SAT was equipped with a tracker consisting of 2 planes of silicon strips in front of the calorimeter opposite the masked calorimeter. The use of the tracker data allowed a considerable reduction in the systematic error due to the definition of the fiducial region in the unmasked calorimeter.

The SAT Bhabha trigger required a coincidence of coplanar energy deposits of greater than 12 GeV, and was measured to have an efficiency of 100% with a statistical uncertainty of 0.01%.

The analysis of the SAT data followed closely those described in refs. [1] and [2]. The event selection criteria which defined the experimental acceptance were:

1. Acoplanarity angle, defined by the beam axis and the showers in each calorimeter, less than 20°.
2. Radial position of the shower in the masked calorimeter less than 31.25 cm.
3. Radial position of the shower in the unmasked calorimeter greater than 12.50 cm.
4. The minimum of the energies in the masked and the unmasked calorimeter greater than 65% of the beam energy.
5. The fraction of the energy of the shower in the masked calorimeter which is in the first readout ring (behind the ring mask) less than 65%
6. Azimuthal position in the masked calorimeter more than 8° from the vertical junction between the calorimeter half–barrels.

The theoretical visible cross-section was evaluated using the Monte Carlo event generator BHLUMI V4.03 [9] and the detector response was simulated using the GEANT package [10]. The authors of BHLUMI V4.03 have estimated the theoretical uncertainty for a luminometer of similar geometrical acceptance to the SAT at $\pm 0.16\%$. However the SAT analysis uses a combination of acceptance masks, selections on positions of charged particle tracks and on energy. By varying these selections it was checked that the theoretical QED cross-section was stable within the estimated uncertainty. Including the $\mathcal{O}(\alpha)$ electroweak corrections the theoretical uncertainty on the visible Bhabha cross-section was taken to be $\pm 0.17\%$.

The systematic uncertainty of the SAT luminosity measurement arises principally from the geometrical definition of the masks, the acceptance selections and the sensitivity to the LEP interaction point and beam tilts. As a result of improved energy calibration of the calorimeters the sensitivity to the minimum energy required is much reduced compared to previous analyses [1,2]. The energy distributions (after requiring $E/E_{BEAM} > 0.65$ in the opposite calorimeter) and the minimum energy distribution relative to the beam energy after the final energy calibration are shown in Figures 1(a-c). The luminosity changes by less than 0.1% for variations of the minimum energy cut between the trigger threshold at 0.3 to within 4 standard deviations of the elastic scattering peak at 0.85 as shown in Figure 1(d). Backgrounds arise from $e^+e^- \to \gamma\gamma(\gamma)$ events and from accidental coincidences of off–momentum electrons. The latter was measured using a delayed Bhabha trigger. The $e^+e^- \to \gamma\gamma(\gamma)$ background was evaluated using an event generator [11]. The total systematic uncertainty on the luminosity was estimated to be $\pm 0.29\%$, the individual contributions to which are shown in Table 2.

4.2 The VSAT Measurement

The VSAT is a tungsten-silicon calorimeter which consists of four modules located at 7.7 m from the DELPHI interaction point, behind the superconducting quadrupoles (SCQ). Due to the defocusing effect of the SCQ the angular coverage for particles of the beam energy is between 5 and 6.5 mrad in polar angle and approximately 45° in azimuthal angle. The VSAT trigger for Bhabha events requires coincident energy depositions in opposite modules of at least 20 GeV; a delayed Bhabha trigger was used to determine the accidental rate.

For 1994 and 1995 data, the VSAT luminosity was used to check the run to run stability of the STIC measurement, while for 1993 data the VSAT luminosity was used, as in 1991, to determine the relative point-to-point luminosity in the energy scan.

There were three major improvements with respect to 1991 analysis. First, there was a considerable improvement in the simulation, done using the fast simulation program (FASTSIM) described in ref. [1]:

- High statistics extensive simulations of different beam conditions were performed to evaluate the dependence of the Bhabha accepted cross-section on the beam parameter variations and extract the corresponding coefficients, which are needed to correct the luminosity determination with the procedure described in detail in ref. [1].
- Compared with the simulations performed for the analysis of 1991 data, finer and more extended variations of the beam parameters were explored.
- Both BABAMC [12] and BHLUMI [9] generators were used (the comparison between the two computations was found to be very good in the VSAT angular region).
- Each FASTSIM run had larger statistics.
- Finally, different geometrical positions of the four VSAT calorimeters with respect to the beam pipe were tested, within the uncertainty of the survey measurements.

The second improvement was a better understanding of the alignment of the detector with respect to the beam pipe, which is particularly important in the LEP plane (x, z plane). This was obtained by a careful study of the shape of the distributions of the impact points of the two Bhabha electrons on the detector; these distributions were parameterized in terms of a few relevant parameters quite sensitive to the detector alignment. The dependence of these parameters on the variations of the beam spot coordinates was compared between real and simulated data; the alignment which best fitted the data was determined with its uncertainty by adjusting the simulated (x, z) positions of the four VSAT calorimeters with respect to the beam pipe.

The third improvement was the use of a restricted fiducial volume, which had a smaller acceptance than the large fiducial volume used in 1991 analysis (about 78%), but required a considerably smaller correction for the variation of the beam parameters and had a much reduced systematic error. Two types of events were rejected in the restricted acceptance that had previously been accepted. The first consisted of events in which at least one of the two electrons had an impact point on the detector close to the outer ring of the acceptance (radial distance from the nominal beam axis greater than 7.8 cm). Due to the residual uncertainty in the alignment of the detector with respect to the beam pipe, described above, cutting these events reduced the corresponding systematic error at the off-peak points by about a factor 6. In the 1991 data this systematic error was much smaller because of the smaller spread in the average values of the beam spot x-coordinates and was negligible compared with the other sources of systematic error. The second selection excluded events in which both electrons were close to the inner edge of the acceptance by requiring that the sum of the x-coordinates of the impact points of the

two electrons be above a given cut. The cut was chosen at the minimum value for which stability in the luminosity determination was obtained. The corresponding uncertainty in the luminosity of the off-peak points was about $\pm 0.02\%$.

Table 3 summarizes the various contributions to the error for the energy point at peak+2 (the errors are slightly smaller at peak-2 and at the pre-scan point).

As for 1991 data, the uncertainty due to errors in the correction factors consisted of a part which was almost uncorrelated between different energy points and of a part which was strongly correlated. The latter, for 1993 data, was about $\pm 0.06\%$ and was added quadratically to the VSAT statistical error at the Z^0 peak ($\pm 0.05\%$) to give the normalization error to the SAT absolute luminosity. The other uncorrelated systematic errors were convoluted quadratically with the statistical error at each energy point.

4.3 The STIC Measurement

A second generation luminometer, the STIC (Small Angle TIle Calorimeter) [13], was installed in the DELPHI detector before the 1994 LEP run. It consisted of 2 lead scintillator sampling calorimeters, located at $\pm$ 220 cm from the interaction point, providing a full angular coverage in the region between 29 and 185 mrad with respect to the beam line. The scintillating tiles were arranged in towers projecting to the interaction point with 10 radial rings and 16 azimuthal sectors. The absence of cracks pointing to the interaction region and the scheme of light collection provided a very uniform energy response and an excellent energy resolution ($\sigma(E)/E \simeq \pm 2.7\%$ on the Bhabha peak as shown in Figure 2). The uniformity of the energy response and the segmentation of the detector allowed a reconstruction of the radial centre of a shower with a resolution which, at the border between towers, was about ± 250 μm. The way the detector was mechanically assembled resulted in a knowledge of the scintillating tile positions of better than ± 50 μm. Monte Carlo simulations showed that this translates into an effective knowledge of the tower positions of ± 20 μm.

The major improvements with respect to the previous DELPHI luminometer (SAT) can be summarized as follows:

1. The excellent energy resolution allowed for an easy separation of Bhabha scattering events from the background due to off momentum particles from beam-gas interactions.
2. The accuracy in the definition of the internal geometry of the detector, the absence of discontinuities and the good spatial resolution allow a very precise definition of the geometrical acceptance.

During the 1994 data taking STIC worked well, apart from 3 dead tetrodes during the first 5 pb^{-1}, of which only one had an influence on the luminosity measurement. A correction for this effect contributes negligibly to the final systematic error.

The luminosity was measured with the same "mask technique" used by the SAT. A high precision tungsten mask pointing at the interaction region, with a total thickness of 17 radiation lengths, covered the inner 35 mm of the acceptance of one of the calorimeters. Therefore a cut on the energy of the reconstructed shower translates into a very sharp cut on the inner radius, with an absolute precision of ± 20 μm, as determined by the deviations from circularity of the edge of the mask, which was measured with an accuracy of ± 1 μm. The smearing due to the transition region of the tungsten edge was measured to be 20 μm in a test beam, by using a silicon microstrip detector to define the incoming particle. This is negligible compared to the smearing due to multiple scattering in the beampipe.

The excellent position resolution in the region between two towers means that STIC can provide an independent luminosity determination, entirely based on the reconstructed position of the showers. This was used as a cross-check of the results, as well as for a useful study of the luminosity measurement at LEP II when the mask is not used.

The trigger was based on the same scheme as for the SAT: the analog sum of the signals from 45° azimuthal sectors, each overlapping 22.5° with the neighbouring one, were considered and a coincidence of energy depositions coplanar with the beam in both calorimeters larger than about 9 GeV was required. A prescaled single arm trigger was used to monitor possible trigger inefficiencies, which were found to be smaller than 2 $\times 10^{-4}$.

In the selection of the Bhabha events only the most energetic clusters on both sides were used.

To remove the background due to off-momentum particles the following cuts were applied:

1. On each side the energy of the cluster was required to be larger than 65% of the beam energy.
2. The acoplanarity between the 2 clusters was required to be less than 20°.

The effect of the energy cut is shown in Figure 3.

A special trigger, requiring a coincidence between the signal from one arm and the delayed signal ($\Delta t = 89$ μs) from the other, measured the residual background due to off-momentum particles This measurement showed that it was smaller than 2 $\times 10^{-4}$.

To accept radiative Bhabha events, as well as to avoid a strong sensitivity of the accepted cross-section to the beam parameters, the standard technique of an asymmetric acceptance was used.

The following cuts were applied to define the geometrical acceptance:

1. The radial position of the reconstructed cluster was required to be below 25 cm on the tungsten ring side.
2. The radial position of the reconstructed cluster was required to be between 8.2 and 28 cm on the opposite side.

Due to the presence of the tungsten ring, the side with the narrow acceptance was always the same. The variation of the acceptance was equal to 0.1% per mm of longitudinal displacement of the interaction point, while the sensitivity to the transverse position of the interaction point (IP) and to tilts and acollinearities of the beams was much smaller.

Selected collinear Bhabha events allowed a measurement of the average position of the interaction point, on a fill by fill basis, by minimizing the distance of closest approach of the trajectories joining the reconstructed impact points on the calorimeter faces. The typical statistical accuracy for the longitudinal position of interaction point was approximatively 150 μm, using the data from a single fill. A cross-check was performed with the measurement done by the DELPHI tracking system. The difference between the two determinations of the longitudinal position of the interaction point had a standard deviation of 200 μm.

An accurate estimation of the Bhabha cross-section accepted inside the luminometer was obtained by means of a full simulation of the detector, based on the GEANT [10] program. The simulated events were analysed in the same way as the real data.

The event generator BHLUMI 4.03 [9], which includes the complete $O(\alpha)$, the full leading logs at $O(\alpha^2)$ and the $\gamma - Z$ interference terms was used. The theoretical precision in the calculated cross-section was estimated to be 0.11%.

The total accepted cross-section was estimated to be 54.829 $\pm$ 0.010 nb at a centre-of-mass energy of 91.250 GeV.

The contribution of the process $e^+e^- \rightarrow \gamma\gamma$ in the selected sample of Bhabha was calculated to be 0.05%.

A detailed list of the contributions to the systematic uncertainty is given in Table 4. The error related to the position of the interaction point takes into account the fact that the distance between the two STIC front faces was measured with an accuracy better than 250 μm. It also takes into account the largest observed variation in temperature measured by the probes located around the STIC modules.

The overall uncertainty is evaluated to be 0.09%, which is better than the design goal of the STIC luminometer. This systematic uncertainty is common to the 1994 and 1995 measurements.

During 1995 the STIC trigger had to be modified in order to cope with the bunch train running of LEP. The strobe signal for the calorimeter ADC's was made by a coincidence of the wagon gate and the signals coming from the Veto system, which consists of 64 trapezoidal scintillation counters assembled into 2 planes and put in front of the calorimeter.

No wagon assignment was available in 411 out of the 1.6 million Bhabha events taken in 1995 due to inefficiencies of the Veto, and therefore the energy in the STIC was slightly underestimated. In 1.6% of the cases, due to noise in the Veto, the wagon assignement was ambiguous, but the energy in the STIC could be easily corrected offline.

Therefore the contribution of the bunch train operation of LEP to the systematics of the luminosity measurement is negligible.

5 Hadronic Cross-sections

As in previous analyses [1,2] the event selection was based on charged particles only, having momentum greater than 0.4 GeV and polar angle, θ, between 20° and 160°. In order to retain only well measured tracks, those shorter than 30 cm or with momentum resolution larger than 100% were rejected. Events were retained if their charged multiplicity, N_{ch}, was above 4, and if the total energy of the charged particles, E_{ch}, was greater than 12% of the centre-of-mass energy. Bhabha events with multiple reinteractions in the detector material were removed by requiring events with less than 11 charged particles to have E_{rad} $(=\sqrt{(E_f^2 + E_b^2)})$ less than $0.90\sqrt{s}/2$, where $E_{f,b}$ stands for the total energy deposit in the forward and backward electromagnetic calorimeters (FEMC).

The present analysis differs from the previous ones when selecting the tracks with respect to their origin. The determination of the primary vertex of each event was improved, thus allowing the tracks to be selected with tighter cuts: the impact parameter with respect to the vertex position was required to be less than 2 cm in $R\phi$ and less than 4 cm/sinθ in z. A large fraction of the tracks originating from secondary interactions could be eliminated in this way and the residual background from low multiplicity leptonic events could be reduced by up to 50%. As another benefit from the new track selection, the simulation reproduced the real data more accurately and the systematic uncertainty on the selection efficiency was reduced from 0.11% to 0.09%. For those events where the vertex search did not converge, the tracks were selected with respect to the position of the beam spot. About 3% of the events were accepted in this way in 1993 and 1995, and about 4% in 1994.

The trigger efficiency was derived from a comparison of independent trigger components of the experiment. The efficiency found was higher than 99.99% at all energy points.

A total of 2,650,000 events was selected over the three years.

The selection efficiency was found from Monte Carlo simulations based on the JETSET 7.3 generator [14] tuned to DELPHI data [15]. The simulation was carried out for those events in which the generated annihilation energy was greater than $0.1\sqrt{s}$. This cut was introduced explicitly into the fitting procedure used to extract the Z^0 parameters and was estimated to have a negligible effect on the systematic errors. The determination of the Z^0 parameters was therefore insensitive to the theoretical description of the spectrum of low mass hadronic resonances.

The selection efficiency determined from the simulation was corrected for instabilities of the tracking detectors and for detection and tracking inefficiencies in the forward region not included in the Monte Carlo. These corrections are shown in Table 5 for each energy point.

The corrected selection efficiency was found to be about 94.8% on the resonance peak in 1993 and 1994. It is largest at peak energies and is smaller by $(0.044 \pm 0.015)\%$ at 89.4 GeV and by $(0.027 \pm 0.015)\%$ at 93.0 GeV because of the variation of N_{ch} and $E_{ch}/\sqrt{s}$ with the collision energy. It was about 0.5% larger in 1995, mainly because of the extension of the acceptance of the Inner Detector in the forward region. The total systematic uncertainty on the 1993 and 1995 selection efficiencies amounts to $\pm$ 0.09%, out of which 0.07% are common to other years. The systematic uncertainty is $\pm$ 0.10% in 1994, with a part common to previous years amounting to 0.08%. As an example, the different contributions to the systematic uncertainties obtained in 1995 are reported in Table 6.

The influence of the bunch train operation of the LEP collider on the response of the tracking and luminosity detectors, as well as on the track reconstruction efficiency, was investigated. The cross-sections corresponding to each bunch number were extracted. The values obtained, relative to the total cross-section at each collision energy in 1995 are shown in Figure 4. No significant variation of the cross-sections with the bunch number was observed.

The $\tau^+\tau^-$ and e^+e^- backgrounds were evaluated from simulations based respectively on the KORALZ [16] and on the BABAMC [12] generators, and by inspection of distributions sensitive to the residual contaminations. These distributions showed that the simulated backgrounds were underestimating the observed ones. The magnitude of each simulated background was then rescaled in order to achieve agreement between the simulated and the real distributions. The $\tau^+\tau^-$ background was found to be about $(0.4 \pm 0.03)\%$ at all energies. The e^+e^- background was typically $(0.07 \pm 0.02)\%$ at 89.4 GeV and $(0.03 \pm 0.01)\%$ at 91.2, 91.3 and 93.0 GeV. The two-photon collision background was estimated to be 16 ± 3 pb from Monte Carlo simulations based on the TWOGAM generator [17], accounting for all three components of the process (i.e. QCD, QPM and VDM). The systematic uncertainties related to the residual backgrounds are summarised in Table 6.

In Figure 5, the events selected in 1994 at the peak energy are compared to simulated samples of the $q\bar{q}$ signal and of all relevant backgrounds. The charged multiplicity distribution is shown, as well as two background sensitive distributions. Above the cut values the combined signal and background distributions reproduce the data well .

The selection efficiencies and residual backgrounds found at peak energies are summarised in Tables 11, 12 and 13. The hadronic cross-sections measured in 1993, 1994 and

1995 are given in Table 7. Data from a short period in 1994 when the beam energy was significantly different have been treated separately.

6 Cross-sections and Forward–Backward Asymmetries in the e^+e^- Channel

6.1 Selection Criteria

Two different methods were used for event selection, as described in ref. [2]. Only the barrel region of DELPHI was used for this analysis. In each method, both the electron and the positron were required to be within the range $44° < \theta < 136°$, where θ was the polar angle of the particle with respect to the direction of the electron beam, and the acollinearity was required to be smaller than 10°. Due to the influence of the t-channel contribution to e^+e^- scattering, the barrel angular region is the most sensitive to the electroweak parameters.

6.1.1 Method 1

This method largely relies on the energy measured in the HPC. Due to the presence of about 0.7 radiation length of material in front of the HPC, electrons have a high probability to radiate before reaching the calorimeter. To obtain the complete reconstruction of the electromagnetic energy, clusters were constructed in the calorimeter by selecting the two most energetic electromagnetic showers in opposite hemispheres and adding to these showers the energy released in the electromagnetic calorimeter in a cone of half-angle 5° around the shower direction, or having a transverse energy, with respect to the most energetic shower, smaller than 0.2 GeV. Charged particles were selected by requiring:

- momentum greater than 1.5 GeV;
- impact parameter to the average interaction point smaller than 5 cm both in the radial and in the beam direction;
- track length greater than 30 cm.

The association between the charged particle track and the electromagnetic shower was not explicitly required. The direction of the charged track or, in case it was missing, the direction defined by the electromagnetic shower centroid and the mean beam position, was used as the fermion direction. Events were divided into two hemisphere defined by the plane perpendicular to the most energetic electromagnetic cluster direction. In order to recover information about tracks which could have deteriorated in the region after the VD, an algorithm was developed to reconstruct "track segments", independently from the global track search, by using hits in the three VD layers. Events were accepted if they fulfilled one of these two sets of requirements:

- two energy clusters in opposite hemispheres, at least one with energy above 30 GeV, the other above 25 GeV;
- no more than 4 charged particles and, for topologies with more than two tracks in one hemisphere: total electromagnetic energy greater than 70 GeV;
- for topologies with less than two tracks: VD hits compatible with one charged track segment per hemisphere;

or

- one energy cluster with energy above 40 GeV;
- one charged particle in each hemisphere;
- no energy deposited beyond the first 1.5 interaction lengths of the Hadron Calorimeter.

The energy cuts quoted were used at the peak energy, they were scaled according to the event centre-of-mass energy at the other scan points. To avoid the region in polar and azimuthal angle where poor efficiency is expected for electromagnetic energy (and track) reconstruction, both fermions were required to be outside the polar range $88° < \theta < 92°$ and at least one was required to be outside $\pm 0.7°$ in ϕ from the HPC gaps between modules.

The selection efficiency was estimated by using BABAMC [12] generated events to be $(89.34 \pm 0.10)\%$, $(89.57 \pm 0.10)\%$ and $(89.77 \pm 0.10)\%$ in the 1993, 1994 and 1995 runs respectively. The loss of events was mainly due to the azimuthal fiducial cuts. The selection efficiency was found to be independent of the centre-of-mass energy, within the Monte Carlo statistical error.

The main background was due to $\tau^+\tau^-$ events and was estimated by using simulated $\tau^+\tau^-$ events, generated by KORALZ [16] Monte Carlo. In the θ acceptance region, the percentage of $\tau^+\tau^-$ events passing the selection cuts was $(1.38 \pm 0.04)\%$, $(1.18 \pm 0.05)\%$, and $(1.24 \pm 0.04)\%$ in 1993, 1994 and 1995 runs respectively, with negligible dependence on the centre-of-mass energy.

6.1.2 Method 2

In this method, e^+e^- events were selected with two almost independent sets of experimental cuts, chosen in such a way as to minimize the correlations between the two sets. As in method 1, a cut in polar angle at $90 \pm 2°$ was applied. In one set (selection A), events were accepted if they had :

- at least two track segments in opposite hemispheres seen by the VD and no more than four in total; the 2-versus-2 track segment topology was excluded to reject photon conversions;
- two high energy electromagnetic clusters observed in the HPC, at least one with energy above 75% of the beam energy and another above 55% .

In the second set (selection B), events were accepted if they had:

- at least 2 charged particle tracks, of momentum greater than 1.5 GeV and distance of closest approach to the nominal vertex position less than 5 cm, seen by the DELPHI tracking system (except VD) with acollinearity less than 10°, and no more than four tracks in total; the 2-versus-2 track topology was excluded;
- the quadratic sum of the momenta of the highest momentum charged particles in each hemisphere greater than $0.99\sqrt{s}/2$;
- the ionization, as measured by the TPC, of all tracks in the event compatible with the electron hypothesis;
- no energy observed in the last three layers of HCAL associated to the impact points of the two highest momentum charged particles;
- the Outer Detector hit pattern associated to the impact points of the tracks compatible with the pattern of a particle showering in or before the OD, or giving back-scattering from the calorimeter;
- no hit in the muon chambers associated to the tracks.

Considering the selections A and B as independent, the efficiency of each of them and the overall efficiency of the "OR" of the two could be easily computed by a comparison of the number of events selected by each one separately or by both simultaneously. To get a correct result, the contribution of background events passing the cuts had first to be subtracted. The presence of background in the sample of selected events had two consequences. First, it increased the number of selected events, second it biased the estimate of the selection efficiency towards smaller values. Using $\tau^+\tau^-$ simulated events the background on the "OR" of the selections was estimated to be $(1.10 \pm 0.04)\%$, $(0.83 \pm 0.04)\%$ and $(0.85 \pm 0.04)\%$ in 1993, 1994 and 1995 runs respectively. In 1994, as an example, it is $(0.49 \pm 0.03)\%$ for selection A only, $(0.53 \pm 0.03)\%$ for selection B only, and $(0.05 \pm 0.01)\%$ for the "AND" of the two selections. After the background correction, the overall efficiency of the two selections was measured to be $(97.82 \pm 0.07)\%$, $(96.95 \pm 0.06)\%$ and $(97.42 \pm 0.08)\%$ in 1993, 1994 and 1995 runs respectively. The simulated e^+e^- events were used to estimate and remove the bias caused by the correlation between the two selections due to the detector structure or to the kinematics of the events. The bias on the combined efficiency was found to be 0.1%. The stability in the estimated total number of events with respect to variations of the cuts is shown in Figure 6. The stability was found to be better than 0.20%.

In both methods the measured efficiencies did not include the loss due to the exclusion of the polar angle region around 90°.

6.2 Measurement of the Cross-section

A total of 24,286, 41,290 and 20,833 events was selected with Method 2 in 1993 1994 and 1995 data respectively. A correction was applied for the $\pm 2°$ polar angle fiducial cut around 90°. It was computed at the different energies by using the program TOPAZ0 [18] and checked with ALIBABA [19]. No significant difference was found between the two generators. The total cross-sections obtained with the two selection methods were compatible and the arithmetic average of the two results was used. Since the two samples are highly correlated, there was no reduction in the statistical error. In order to fit the results with the ZFITTER [20] package, the t-channel contribution had to be removed from the measured cross-sections and asymmetries. In addition, a correction was applied because ZFITTER only allows a limit on the polar angle of one of the two final state fermions, the other being constrained by the collinearity requirement. These two corrections were computed by using TOPAZ0 and ALIBABA. The two results were compared at each energy, and the difference between the two has been taken as an indication of the systematic error. For the t-channel subtraction a mean value, over the different energy points, of 1 pb and 0.5 pb on the forward and backward cross-sections respectively was deduced. For the two fermion acceptance corrections a mean value of 0.15% of $\sigma(s)$ was estimated.

After the subtraction of the t-channel contribution and the correction for the polar angle definition by the electron only, the cross-sections given in Table 8 were obtained. The errors quoted are statistical only. Apart from the luminosity, systematic errors arise from the event selection, acceptance definition and from the t-channel and background subtractions. The systematic uncertainties are shown in Tables 11,12 and 13 for the different run periods. Of the total systematic errors, 82% are assumed to be correlated between the different years.

6.3 Measurement of the Forward-Backward Asymmetries

In the samples of events selected with the two methods described above, the charge of the event was defined as positive when the positron was in the forward hemisphere, negative in the opposite case. The method used to determine the charge was similar to the one used for the analysis of the 1992 data [2]. In the $e^+e^- \to e^+e^-$ events, in addition to the canonical charge definition from reconstructed tracks, it is possible to look at the effects of the magnetic field bending to the impact position of HPC clusters. It is then possible to correlate the sign of the bending to the sign of the event charge allowing for a high redundancy on the charge determination. The percentage of events with two charged particles of the same sign was about 2% of the two-track events. The use of the bending to determine the charge of those events and the charge of the events with more or less than two tracks, avoids possible hemisphere dependent biases. The measured event charge was compared with the generated one in Monte Carlo events, showing a discrepancy on 0.4% of the events, with no evidence of bias.

The forward-backward asymmetries were determined with the same samples of events considered for the cross-section determination and are given in Table 8 with their statistical uncertainties. Systematic errors arise because of charge confusion, forward-backward acceptance differences and t-channel subtraction. They are shown in Tables 11,12 and 13 for the different run periods.

7 Cross-sections and Forward–Backward Asymmetries in the $\mu^+\mu^-$ Channel

7.1 Selection Criteria

The same selection criteria were applied for all periods of data taking 1993 - 1995, with minor differences to account for year–to–year changes in detector performance.

The following kinematic, topological and muon identification cuts were applied to obtain a sample of $e^+e^- \to \mu^+\mu^-$ events with high efficiency and small remaining background:

- The two most energetic charged particles were required to have momenta $P_1, P_2 > 5$ GeV.
- To suppress $\tau^+\tau^-$ contamination the event variable P_{rad}, defined as $\sqrt{(P_1^2 + P_2^2)}$, was required to exceed $0.87\sqrt{s}/2$.
- The acollinearity of the two most energetic charged particles was required to be less than 20°.
- The negatively charged particle was required to to lie within the polar angle interval $20° - 160°$ for the cross-section measurement. This was extended to $11° - 169°$ for the asymmetry determination.
- Both candidate tracks had to be identified as a muon, requiring an associated hit in the muon chambers (MUB, MUF and, from the latter part of 1994 onwards, the SMC) or energy depositions in the HCAL, the HPC or the FEMC consistent with a minimum ionizing particle. Furthermore the calorimeters were used to reject Bhabha events and tracks from hadrons.
- To reduce the background from cosmic rays, at least one track was required to originate from close to the beamspot at the perigee in the transverse plane. The cuts applied depended on the detectors participating in the track reconstruction, but

was 0.1 cm for the majority of cases. Cuts were also placed on the axial separation at this point.

For the asymmetry analysis of the 1993 pre-scan period, problems with the Forward Chambers A necessitated restricting the polar interval to $18° - 162°$. In all years, events lying within 2° of the six TPC azimuthal sector boundaries were excluded from the asymmetry measurement, as there was evidence of possible bias in these regions. Furthermore the $\sim 0.5\%$ of events in which the charge assignment was the same sign for both tracks were discarded in the asymmetry analysis.

A run selection was applied to exclude runs from the analysis, in which relevant components of the DELPHI detector were not adequately operational. For the cross-section analysis this involved a combination of the TPC, the HCAL and the muon chambers. In addition, runs were excluded where the luminometers had problems, where the hadronic cross-section indicated severe problems in the data taking, and where the beam energy was anomalous. As the analysis of the forward-backward asymmetry is less dependent on knowledge of detector efficiencies, a looser run selection was used here. Only runs, in which the TPC was not fully operational were excluded, although in 1993 further requirements were placed on the muon identification detectors to eliminate a possible detector bias.

Tables 11,12 and 13 show the number of events remaining for the analyses after all cuts for the different run periods.

7.2 Measurement of the Cross-section

7.2.1 Determination of selection efficiencies

As far as possible, corrections were determined from the data themselves, using simulations only for the studies of correlations and for small corrections. This is possible because of the distinctive back to back event topology of $\mu^+\mu^-$ events, and because the DELPHI trigger fires on single tracks.

The important contributions to the selection efficiency which can be determined primarily from the data are the following:

- **Trigger efficiency**
  This was measured by comparing independent subtriggers. The event efficiency was $> 99.5\%$ for all years.
- **Muon identification efficiency**
  The principal method used a restricted event sample with negligible $\tau^+\tau^-$ and Bhabha background. The event efficiency was found to be $> 99\%$ throughout the acceptance, apart from in between the barrel and the forward regions for those data collected before the installation of the SMC.
- **Tracking efficiency**
  A loss of $\sim 3\%$ near the sector boundaries of the TPC was determined from the azimuthal distribution of events. Away from these boundaries an efficiency of $> 99.5\%$ was calculated by use of an event sample with one identified muon track plus a hit in the muon chambers in the opposite hemisphere.

These efficiencies were measured and then combined in polar angle bins to account for angular correlations. Systematic errors were assigned from comparison of various methods and from the statistical precision of the measurements.

Further losses, such as those due to vertex cuts and background vetoes were measured through a combination of data and simulations. The loss due to the P_{rad} cut was studied with a variety of event generators and found to be $< 0.1\%$.

The total selection efficiencies for the different running periods are given in Tables 11, 12 and 13. These are with respect to events within the polar, momentum and acollinearity acceptance stated above. Uncertainties in the detector implementation of this acceptance are included in the assigned error. Figure 7 shows the behaviour of the selection efficiency as a function of the polar angle.

7.2.2 Determination of residual backgrounds

The residual contamination from $\tau^+\tau^-$ events was determined by fitting the relative contribution of $\mu^+\mu^-$ and $\tau^+\tau^-$ events in discriminant variables. The best sensitivity was obtained by fitting in P_{rad}, as illustrated in Figure 8. The residual $\tau^+\tau^-$ contamination was found to be $\sim 1\%$.

The background from cosmic muons was determined from data, by counting the number of events failing the impact parameter cuts and interpolating to the region within the cuts. This gave a contamination of $\sim 0.1\%$. Cross-checks using detectors with timing and directional information, such as the RICH, confirmed this result.

Contamination from other backgrounds, such as from two photon processes and from Bhabha events was found to be of order 0.01% and therefore negligible in the measurement.

The background estimation for the three years is summarised in Tables 11, 12 and 13.

7.2.3 Results

The resulting cross-sections after subtraction of backgrounds and correction for inefficiencies are given in Table 9. These numbers are given within the phase space defined by a cut of 5 GeV on the momentum of the outgoing particles, an acollinearity cut of 20° and a restriction of the polar angle of the negatively charged muon to $20° - 160°$. The systematic error does not include the uncertainty due to luminosity measurement. The differential cross-sections combined for all years 93 - 95 are shown in Figure 9.

As a further cross check, for each running period the stability of the cross-section versus time was investigated by calculating cross-sections for each LEP fill. In addition, for the 1995 run period where LEP was operated in bunch train mode the stability versus the bunch number was studied. No evidence of any systematic dependence was found.

7.3 Measurement of the Forward-Backward Asymmetry

The forward-backward asymmetry was calculated using an unbinned maximum likelihood fit to the lowest order form of the angular distribution. In such a fit the result is insensitive to knowledge of the selection efficiencies, provided that these are the same for events with forward going negative muons and backward going negative muons.

To test that this assumption of symmetry in the charge and hemisphere efficiency was valid, the detector asymmetry, A_{det}, was determined for each running period. This is defined as follows:

$$A_{det} = \frac{\epsilon^-_{fwd}\epsilon^+_{bwd} - \epsilon^-_{bwd}\epsilon^+_{fwd}}{\epsilon^-_{fwd}\epsilon^+_{bwd} + \epsilon^-_{bwd}\epsilon^+_{fwd}}, \qquad (1)$$

where ϵ^{+-}_{fwd} and ϵ^{+-}_{bwd} are the efficiencies to reconstruct a μ^+/μ^- in the forward or backward hemisphere of the detector respectively. Evidence of non-zero detector asymmetry was found around the azimuthal TPC sector boundaries, and in the very forward region during the 1993 pre-scan. With these regions excluded, A_{det} was found to be compatible with zero for all periods. For each data set the statistical uncertainty on this conclusion was assigned as the systematic error. This dominated other uncertainties, but was still small compared to the statistical error. Figure 10 shows the detector asymmetry as a function of the polar angle for the running period of 1994.

Further sources of systematic errors that have been considered include the biases induced by $\tau^+\tau^-$, cosmic and Bhabha contamination, possible uncertainties in the measurement of the polar angle, a charge dependence of the momentum determination, and the exclusion of events with at least one misassigned charge. The effect of neglecting higher order terms in the form of the angular distributions was investigated and found to be small.

The stability of the forward-backward asymmetry against time was tested by calculating its value separately for each LEP fill. Also the asymmetry was determined in bins of the polar angle, to look for any residual systematic effects. These checks were satisfactory.

The forward-backward asymmetries and the assigned systematic errors are given in Table 9. These are given within the phase space defined by a cut of 5 GeV on the momentum of the outgoing particles and an acollinearity cut of 20°.

8 Cross-sections and Forward–Backward Asymmetries in the $\tau^+\tau^-$ Channel

8.1 Selection criteria

The selection of $\tau^+\tau^-$ events in the barrel region of the detector from the 1993–1995 data was similar to that described in ref. [2]. In addition, the analysis has been extended to include data in the forward regions of the detector and for the first time with DELPHI data the $\tau^+\tau^-$ cross-section has been measured in the polar angle range $20° < \theta < 160°$. The same selection criteria were applied to the entire sample, with minor differences to account for year-to-year changes in detector performance.

Events were required to be of low multiplicity and to have high thrust, in order to remove background from $q\bar{q}$ final states. Further kinematic restrictions were imposed to remove the backgrounds from e^+e^-, $\mu^+\mu^-$ and four-fermion final states. For the barrel selection the thrust axis, computed using charged particle momenta, was required to lie in the polar angle interval $43° < \theta < 137°$. Events were also rejected if the highest momentum charged particles in each event hemisphere were both in the polar angle range $88° < \theta < 92°$. The following topological and kinematic cuts were applied:

- The number of well reconstructed charged particle tracks per event, N_{ch}, was required to be in the range $2 \leq N_{ch} \leq 6$.
- The event thrust was required to exceed 0.996.
- To suppress $\mu^+\mu^-$ contamination, the event variable P_{rad} (see section 7.1) was required to satisfy $P_{rad} < \sqrt{s}/2$.
- To suppress e^+e^- contamination, the event variable E_{rad}, defined as $\sqrt{(E_1^2 + E_2^2)}$, where E_1 and E_2 are the energies in the electromagnetic calorimeters within a cone of half–angle 30° around the thrust direction in each hemisphere, was required to satisfy $E_{rad} < \sqrt{s}/2$.

- To suppress four-fermion final states, the total charged and neutral energy, E_{vis}, was required to exceed $8\sqrt{s}/91.2$ GeV.

Additional cuts were imposed on those events with $N_{ch} = 2$ to reduce further the backgrounds from Bhabha scattering and cosmic muons. The former were most effectively removed by requiring that the acollinearity angle exceed 0.5° and the latter were almost entirely eliminated with tight cuts on the track impact parameters with respect to the beam collision point in the $r - \phi$ plane.

For the 1993 data, in order to avoid selection efficiency bias due to poor modelling of the electron momentum spectrum, the P_{rad} cut was only applied to those events which satisfied a very loose $\mu^+\mu^-$ event selection based on muon chamber and calorimeter information. In the absence of this cut, the e^+e^- background was removed by imposing harder E_{rad} cuts: $E_{rad} < 0.9\sqrt{s}/2$ and $E_{rad} < 0.6\sqrt{s}/2$ for those events in which the track of the highest momentum particle in either thrust hemisphere passed close ($\pm 1.5°$) to one of the 24 azimuthal boundary planes between adjacent HPC modules.

For the 1995 data, in order to avoid biases due to imperfect modelling of the E_{rad} distribution, events were required to satisfy $E_{rad} < 0.95\sqrt{s}/2$ if the highest momentum charged particle in each event hemisphere passed more than 0.3° from the nearest HPC azimuthal boundary. For events in which only one of these highest momentum charged particles passed more than 0.3° from the nearest HPC azimuthal boundary this requirement was tightened to $\sqrt{s}/3$.

Events in the forward region were selected by requiring that the thrust axis fell in the polar angle ranges $20° < \theta < 43°$ or $137° < \theta < 160°$. The majority of the cuts used in the barrel event selection were also employed in the forward region with, however, several significant changes, in order to suppress background, especially from Bhabha scattering:

- To suppress four-fermion background, E_{vis} was required to exceed $12\sqrt{s}/91.2$ GeV.
- The Bhabha background was severely limited by restricting the acollinearity angle of each event to be greater than 1°, or 2° in the polar angle range $35° < \theta < 43°$ or $137° < \theta < 145°$. For events with more than two charged particle tracks the acollinearity was determined using the vector sum of the charged particle momenta in each thrust hemisphere.
- To restrict further the Bhabha background harder E_{rad} cuts were imposed: $E_{rad} < 0.8\sqrt{s}/2$ or $E_{rad} < 0.6\sqrt{s}/2$ if the thrust axis was in the range $35° < \theta < 43°$ or $137° < \theta < 145°$. In this latter range of angles the electromagnetic calorimetry is relatively poor.

For the analysis of the 1995 data in the forward region the E_{rad} and P_{rad} requirements were altered. If the highest momentum charged particle in each event hemisphere extrapolated to within the acceptance of the FEMC the E_{rad} cut was $0.85\sqrt{s}/2$. If only one of these tracks extrapolated to the FEMC then the cut was tightened to $0.4\sqrt{s}/2$. The P_{rad} cut was reduced to $0.9\sqrt{s}/2$.

A run selection was applied to exclude runs from the analysis in which the relevant components of the DELPHI detector were not adequately operational. For the cross-section analysis this involved a combination of the TPC and the HPC. In addition, runs were excluded where the luminometers had problems, where the hadronic cross-section indicated severe problems in the data taking, and where the beam energy was anomalous. For the asymmetry analysis the requirements on the luminometer performance were dropped.

Tables 11, 12 and 13 show the number of events remaining in each year after the application of the selection criteria.

8.2 Measurement of the Cross-section

8.2.1 Determination of selection efficiencies

The determination of the event selection efficiency for $\tau^+\tau^-$ is highly dependent on Monte Carlo simulation (using the KORALZ program [16]) because the selection criteria are based on the use of a number of global event variables such as E_{rad} and P_{rad}. This contrasts with the e^+e^- and $\mu^+\mu^-$ analyses which treat the reconstruction and identification of each lepton independently. Consequently, the event reconstruction and identification efficiencies do not readily factorize. The trigger efficiency can, however, be determined from the experimental data by comparing independent subtriggers, and in all years it exceeded 99.9%.

The quality of the Monte Carlo modelling of the $\tau^+\tau^-$ events was carefully monitored by comparing distributions of experimental data and simulated data (including residual background contributions) in all of the topological and kinematic variables used for the event selection. Figures 11 and 12 show such comparisons for the event thrust distribution and for the radial energy variable, E_{rad}. A small discrepancy in the modelling of the reconstruction efficiency for tracks close to the six azimuthal TPC boundary planes was observed and a small correction ($< 1.0\%$) was applied to the event selection efficiency.

The combined event selection efficiency for the barrel and forward regions was determined by simulation to be in the range $62\% - 64\%$ for the three running periods . The trigger and selection efficiencies for the different running periods are given in Tables 11, 12 and 13.

8.2.2 Determination of residual backgrounds

The main backgrounds in the selection of $\tau^+\tau^-$ arise from $q\bar{q}$, e^+e^-, $\mu^+\mu^-$ and four-fermion final states. Each of these contributions were determined by Monte Carlo simulation using various discriminating variables to check that the experimental data and simulated data were consistent. For example, the E_{rad} distribution (see Figure 12) is sensistive to the e^+e^- background whereas the P_{rad} distribution is sensitive to the $\mu^+\mu^-$ background. The only other significant residual background, from cosmic muons, was determined from the experimental data using the technique applied in the $\mu^+\mu^-$ event selection (see section 7.2.2) based on impact parameter distributions.

The backgrounds for the different running periods were quite similar but with some variation due to the change of cuts after 1993. As an illustration of typical magnitudes the 1994–1995 background levels were as follows. The four-fermion background was estimated to be 5.5 ± 0.4 pb, that due to $q\bar{q}$ events $(0.92 \pm 0.10)\%$ and that due to $\mu^+\mu^-$ events $(0.57 \pm 0.04)\%$ at all energies. The cosmic muon background was estimated to be $(0.34 \pm 0.03)\%$, $(0.11 \pm 0.01)\%$ and $(0.23 \pm 0.02)\%$ and the e^+e^- background to be 12.9 ± 2.0 pb, 14.9 ± 2.0 pb and 11.2 ± 1.6 pb, at the centre–of–mass energies of 89.4 GeV, 91.2 GeV and 93.0 GeV respectively. The total background at the Z peak was about 3.7% of the selected event sample. Tables 11, 12 and 13 show the various background estimates for the different running periods.

8.2.3 Results

The resulting cross-sections after subtraction of backgrounds and correction for inefficiencies are given in Table 10. These numbers are given fully corrected for the effects of kinematic and acceptance cuts. Careful comparison of the τ pair invariant mass spectrum revealed a discrepancy between the KORALZ and ZFITTER [20] programs at low values

of the invariant mass. The former program, used to compute the event selection efficiency by Monte Carlo simulation, was found to be in error. Consequently a small correction, 4.5 pb, was applied to the measured cross-sections at each centre-of-mass energy for each year.

The systematic error due to selections and backgrounds is estimated to be $\pm 0.6\%$ for all running periods, in addition to the systematic error on the luminosity. The differential cross-sections for 1995 are shown in Figure 13.

8.3 Measurement of Forward-Backward Asymmetry

The forward-backward asymmetry was calculated using an unbinned maximum likelihood fit to the lowest order form of the angular distribution. As remarked in section 7.3, such a fit is expected to be insensitive to knowledge of the event selection efficiencies. The fit was performed on the events of the 1–1, 1–3 and 3–3 topologies in the polar angle range $20° < \theta < 160°$. For the 1995 data an alternative toplogical selection was studied in which 1–N events were used in the fit (N=1,..5). The results were found to be consistent with those obtained with the standard topological selection.

Systematic errors arise from the e^+e^- subtraction, from charge confusion and from neglect of radiative corrections which alter the lowest order angular distribution. A small additive correction (less than 0.003 in magnitude) has to be made to the measured asymmetry to account for biases introduced by the selection cuts. These biases arise from initial state radiation and from the θ dependence of the τ polarization. The precise value of this correction depends on the cuts used, which varied from year to year and between the barrel and forward region, and was determined by Monte Carlo simulation. The uncertainty on the correction of ± 0.0009 was dominated by Monte Carlo statistics. The overall systematic errors are estimated to be ± 0.005, ± 0.002 and ± 0.002 at centre–of–mass energies of 89.4 GeV, 91.2 GeV and 93.0 GeV respectively. The forward–backward asymmetries measured in each running period appear in Table 10. The selection bias described above was not taken into account in previous publications [1,2]. The precision on the 1991 measurements does not warrant the application of this correction. However, the published value of the 1992 asymmetry must be reduced by 0.0021 ± 0.0009 to $0.0071 \pm 0.0088(stat) \pm 0.0019(syst)$. The corrected value of the 1992 asymmetry is used in the fits described in later sections of this paper.

Table 14 gives a summary of the systematic errors in the cross-section determinations in the hadronic and leptonic channels, and their year-to year-correlations. The systematic uncertainties in the luminosity determination are not included. Similarly Table 15 summarises the systematic uncertainties in the determintions of the leptonic forward-backward asymmetries, and their correlations year-to-year.

9 Cross-sections and Forward–Backward Asymmetries in the $\mu^+\mu^-$ Channel with Initial State Radiation

Experimental results from studies of events collected at LEP1 in the channel $e^+e^- \to \mu^+\mu^-\gamma_{ISR}$, with γ_{ISR} being an initial state radiation photon, have been used to probe the cross-sections and forward-backward asymmetries in the energy region between LEP1 and TRISTAN and down to PETRA energies. Similar measurements have been performed previously by DELPHI [21] with the data taken between 1991 and 1994, and by other

experiments [22]. In this section the analysis of the data taken in 1995 is presented. By adding these data to those taken between 1991 and 1994, cross-sections and forward-backward asymmetries were determined as well as the helicity cross-section ratio $\frac{\sigma_{LL}+\sigma_{RR}}{\sigma_{RL}+\sigma_{LR}}$ where the two subscripts stand for the helicities of the incoming e^- and outgoing μ^- respectively. The theoretical background to these analyses is explained in refs. [21] and [23].

For the simulation studies about 220,000 dimuon events were generated with the DYMU3 program [24] at the same 3 energies as the data, about 103,000 $\tau^+\tau^-$ events were generated with the KORALZ program [16] and about 25,000 $e^+e^- \rightarrow e^+e^-\mu^+\mu^-$ events were generated with the FERMISV program [25]. All generated events were passed through the detector simulation program DELSIM [8] and the same data reconstruction program as the data.

9.1 Selection of events

The selection of dimuon events with Initial State Radiation (ISR) from the data taken in 1995 was performed as described in ref. [21]. First a sample of dimuon events with or without photon production was selected for normalisation purposes. From this sample the events with ISR were then extracted. For the calculation of the cross-sections, the same selection procedure was applied to the 220,000 simulated dimuon events.

To select the sample of dimuon events allowing for possible photon emission, the events had to contain two charged particles of momentum greater than 10 GeV, both of which were identified as muons either by the muon chambers, by the hadron calorimeter or by the electromagnetic calorimeters. Both particles had to come from the interaction region, which was defined as $|z|$ less than 4.5 cm and R less than 1.5 cm . The variable $P_{rad} = \sqrt{P_1^2 + P_2^2}$, where P_1 and P_2 are the momenta of the two muons, had to exceed $0.3\sqrt{s}/2$. Events with more than 5 charged particle tracks were rejected.

To reduce the $\tau^+\tau^-$ background, three criteria were introduced. Firstly, if the acollinearity angle between the two muons was larger than 1°, the event was rejected if the energy deposited in the hadron calorimeter was larger than a cutoff value dependent on the polar angle (see [1]). Secondly, if the event had more than 2 charged particle tracks, either the acollinearity angle between the two muons had to be less than 1° or both muons had to have at least one associated hit in the muon chambers. Thirdly, in the procedure to separate ISR from Final State Radiation (FSR) events, a variable ΔE_γ was introduced, which was defined as:

$$\Delta E_\gamma = E'_\gamma - E''_\gamma, \tag{2}$$

where

$$E'_\gamma = \sqrt{s} - E_{\mu+} - E_{\mu-} \tag{3}$$

and

$$E''_\gamma = \frac{|\sin(\theta_{\mu+} + \theta_{\mu-})|}{|\sin(\theta_{\mu+} + \theta_{\mu-})| + \sin\theta_{\mu+} + \sin\theta_{\mu-}}\sqrt{s}\,. \tag{4}$$

In these formulae, $\theta_{\mu+}$ and $\theta_{\mu-}$ are the polar angles, and $E_{\mu+}$ and $E_{\mu-}$ the energies of the muons; the variable E''_γ is an approximation to the energy of an ISR photon emitted in the direction of one of the beams. This variable is also effective in rejecting tau events [21] and only events with $\Delta E_\gamma < 25$ GeV were retained.

Because the selection efficiencies could not be estimated reliably at low polar angles, the cross-sections were determined with samples of events with the μ^- polar angle in the

region $20° \leq \theta_{\mu^-} \leq 160°$. For the measurement of the forward-backward asymmetries however, the likelihood fit method is not affected by the selection efficiencies if these are forward-backward symmetric (see section 7.3). Therefore, for these measurements the μ^- polar angle region was extended to $11° \leq \theta_{\mu^-} \leq 169°$.

After this selection of dimuon events, data runs were rejected if the parts of the DELPHI detector used in the analysis were not fully operational. The total number of dimuons available for the asymmetry analysis in the 1995 data amounted to 29,104. The total number of dimuons selected for the cross-section analysis was 22,389. From the 220,000 simulated $\mu^+\mu^-$ events, 183,318 remained after the dimuon selection in the polar angle region $20° \leq \theta_{\mu^-} \leq 160°$. The tau background was estimated with the simulated $\tau^+\tau^-$ events to be 0.20%. The background from two-photon events was also estimated with simulated events, and found to be less than 0.1% for the channel $e^+e^- \to e^+e^-\mu^+\mu^-$. No simulated events for the channel $e^+e^- \to e^+e^-\tau^+\tau^-$, were found to satisfy the dimuon selection criteria. The cosmic ray background was estimated from the data, by relaxing the definition of the interaction region [1] and counting the number of additional events accepted in the data sample. It was found to amount to 0.43%.

To extract the events with ISR from the dimuon sample the same procedure was used as for the analysis of the 1991-1994 data [21]. To ensure a high purity of the selected sample for all effective annihilation energies ($\sqrt{s'}$), the selection criteria were taken to be different in each $\sqrt{s'}$ interval. Two sets of selections were used depending on whether or not a photon was detected in the electromagnetic calorimeters close to one of the muons.

For the effective annihilation energy $\sqrt{s'}$, or equivalently the $\mu^+\mu^-$ invariant mass $M_{\mu\mu}$, the following expression was used:

$$\sqrt{s'} = M_{\mu\mu} = \sqrt{s - 2E''_\gamma\sqrt{s}}\,. \tag{5}$$

The justification for this procedure is explained in [26]. The analysis was restricted to the $\sqrt{s'}$ region between 20 and 87 GeV.

In the 1995 data sample, 100 ISR events were selected for the cross-section calculation, and 124 for the asymmetry and helicity cross-section ratio calculation. From the 183,318 simulated dimuons , 980 ISR events were selected for the cross-section calculations.

The efficiency of the selection procedure and the contamination by FSR events were studied with a sample of about 146,000 simulated radiative muon events generated by DYMU3 with $\mu\mu$ invariant mass $M_{\mu\mu} < 88$ GeV. The resulting efficiency and the purity regarding FSR are displayed as a function of $\sqrt{s'}$ in Figure 14. The purity of the sample is near 90% over the whole energy interval. In this Figure the values obtained in ref. [21] for the data taken between 1991 and 1994 are also shown. The purity of the 1995 sample is the same within errors as the purity of the previous sample. The selection efficiency for the 1995 data is however higher than the efficiencies obtained for the 1991-1994 data. This is due to the improvement of the track reconstruction at low polar angles with the extension of the ID.

The cosmic ray background was checked using the sample of ISR events selected for the cross-section calculation. No additional events were found when the cuts on the interaction region definition were relaxed.

The background from $e^+e^- \to \tau^+\tau^-$ events was estimated from the sample of simulated $\tau^+\tau^-$ events. No events were found to satisfy the ISR selection criteria.

The background from two-photon processes was estimated from simulated events. It was found that the channel $e^+e^- \to e^+e^-\mu^+\mu^-$ contributed a background of 4.7%, mainly concentrated at low values of $\sqrt{s'}$.

9.2 Cross-sections

For the calculation of the cross-sections the polar angle of the μ^- was required to be in the range $20° \leq \theta_{\mu^-} \leq 160°$. A total of 100 events was selected from the 1995 data, and 980 events from the simulated sample.

The ratio of the averages of the observed to the Standard Model Improved Born cross-sections inside a given $\sqrt{s'}$ interval is given by

$$\frac{<\sigma_{IB}^{obs}(\sqrt{s'})>}{<\sigma_{IB}^{SM}(\sqrt{s'})>} = \frac{N_{obs}(\sqrt{s'}) \cdot N_{sim}^{norm}}{N_{sim}(\sqrt{s'}) \cdot N_{obs}^{norm}}, \tag{6}$$

where $\sqrt{s'}$ is the mean effective annihilation energy in the interval. The quantities $N_{obs}(\sqrt{s'})$ and $N_{sim}(\sqrt{s'})$ represent the numbers of ISR events in a given $\sqrt{s'}$ interval in the data and in the simulated sample respectively. The quantities N_{obs}^{norm} and N_{sim}^{norm} represent the number of dimuon events selected in the real and simulated data samples. In each $\sqrt{s'}$ interval, the normalisation of the ISR sample to the full dimuon sample was calculated separately for the on-peak and off-peak data, after which the results were averaged. The number $N_{obs}(\sqrt{s'})$ was corrected for the two-photon background, and the number N_{obs}^{norm} was corrected for the background arising from cosmic ray and tau events. The other backgrounds were too small to justify a correction. It was verified that the selection efficiency for ISR events was the same for the observed data and the simulation.

Table 16 shows the number of ISR events selected in the 1995 data and in the simulated samples, as well as the cross-section ratio calculated with formula (6) as a function of $\sqrt{s'}$, up to an energy of 87 GeV. Only statistical errors were taken into account. The main source of systematic errors was the modelling of the muon momenta in the simulation. To reduce these effects to a negligible size, the muon momenta were smeared in the simulation to match the resolution observed in the data. Figure 15 shows the ratios between the observed and theoretical Improved Born cross-sections as a function of the effective annihilation energy for the 1995 data. In this Figure the cross-section ratios obtained from the analysis of the 1992-1994 data are also shown. The cross-section ratios from the two samples agree well. Consequently a weighted average was made of the numbers obtained from the two samples. The result of this procedure is shown in Table 16.

The observed cross-sections were calculated by multiplying the cross-section ratios with the Improved Born cross-sections predicted by the SM. The theoretical Improved Born cross-sections, $\sigma_{IB}^{SM}(\sqrt{s'})$, were obtained from the DYMU3 program. The parameters used in this calculation were $M_Z = 91.25$ GeV/c^2, $\Gamma_Z = 2.562$ GeV/c^2, and $\sin^2\theta_W = 0.2296$, which were the default values used by DELPHI for the generation of $\mu^+\mu^-$ events. The observed cross-sections are displayed in Figure 16, together with the cross-sections for the reaction $e^+e^- \to \mu^+\mu^-$ obtained near the Z^0 peak [1,2] and those obtained at PEP, PETRA, and TRISTAN [28]. The published values were corrected to obtain Improved Born values.

9.3 Asymmetries and helicity cross-sections

For the estimation of the forward-backward asymmetries the polar angle of the μ^- was required to be in the range $11° \leq \theta_{\mu^-} \leq 169°$. A total of 124 events was selected from the 1995 data. The distribution of these events as a function of $\sqrt{s'}$ is shown in Table 17.

For events which are not produced in the e^+e^- c.m. frame, the angle between the μ^- and the e^- beam direction in the $\mu^-\mu^+$ rest frame is given by [27]:

$$\cos\theta^* = \frac{\sin\frac{1}{2}(\theta_{\mu^+} - \theta_{\mu^-})}{\sin\frac{1}{2}(\theta_{\mu^+} + \theta_{\mu^-})}, \tag{7}$$

where θ_{μ^+} and θ_{μ^-} are the polar angles of the μ^+ and the μ^- with respect to the e^- beam axis in the laboratory frame.

In each $\sqrt{s'}$ interval the $\cos\theta^*$ distribution for the 1995 data was compared to the distribution obtained for the 1991-94 data and was found to be the same within errors. It was checked that the contamination of the 1995 sample by FSR events was the same as that found for the 1991-94 sample. Therefore the $\cos\theta^*$ distributions from the 1991-94 sample could be added to that obtained from the 1995 sample. In total there were 523 events.

In each $\sqrt{s'}$ interval, the asymmetry A_{FB} was then obtained by performing a maximum likelihood fit of the raw $\cos\theta^*$ distribution to an expression of the form

$$\frac{dN}{d\cos\theta^*} = C[P_{isr}(1+\cos^2\theta^*+\frac{8}{3}A_{FB}\cos\theta^*)+P_{fsr}(1+\cos^2\theta^*)+P_{\gamma\gamma}(1+\cos^2\theta^*+\frac{8}{3}A^{\gamma\gamma}_{FB}\cos\theta^*)], \tag{8}$$

where the term P_{isr} represents the purity of the sample, which on average amounts to 90%, P_{fsr} and $P_{\gamma\gamma}$ are the contamination by FSR and $\gamma\gamma$ events and $A^{\gamma\gamma}_{FB}$ is the asymmetry for these $\gamma\gamma$ events (see Table 17). For the FSR events the asymmetry is taken to be zero, since this refers to the Z^0 peak. Formula (8) does not include radiative corrections. Since the asymmetries determined in this analysis are Improved Born asymmetries, only the electro-weak corrections should be considered. These are small compared to the experimental precision and modify the asymmetry by at most 0.02 in the energy region between 40 and 88 GeV. It was checked on simulated events that the selection efficiency for each $\cos\theta^*$ bin was compatible with that of the corresponding $-\cos\theta^*$ bin.

These fitted asymmetries are shown in Table 17, and are displayed in Figure 17 together with the SM prediction for the Improved Born asymmetry. Figure 17 also shows the asymmetries measured by DELPHI near the Z^0 peak (see [1,2]), after correction to Improved Born values. The SM Improved Born asymmetry was calculated with the DYMU3 program with the parameters mentioned in Section 9.2. The only source of systematic error on the asymmetry, $\delta(A_{FB})^{fit}_{sys}$, which was considered was that resulting from the error on the purity. The values of this error are shown in Table 17.

The helicity cross-sections $\tilde{\sigma}^{\mu}_{+}$ and $\tilde{\sigma}^{\mu}_{-}$ and their ratio (see [23]) were determined as follows. The raw $\cos\theta^*$ distribution in each $\sqrt{s'}$ interval was corrected for selection inefficiencies in the same way as described in [21]. This procedure relies on the fact that the distribution in $|\cos\theta^*|$ is symmetric and of the form $1+\cos^2\theta^*$. The $\cos\theta^*$ distributions were then corrected for the contamination by FSR and $\gamma\gamma$ events by subtracting a distribution obtained from simulated events. Next, in each bin of the $\cos\theta^*$ distribution the corrected content was multiplied by a weight factor:

$$F_{\pm} = A\,(1 \pm B\cos\theta^*), \tag{9}$$

where

$$A = \frac{2}{C_M(3+C_M^2)}, \qquad B = \frac{3+C_M^2}{2C_M^2} \tag{10}$$

and $C_M = \cos\theta^*_{max}$. These weighted contents were summed for all $\cos\theta^*$ bins between -0.8 and $+0.8$ for $\sqrt{s'}$ below 65 GeV, and between -0.9 and $+0.9$ for the other $\sqrt{s'}$

values. The C_M limits were chosen depending on the statistics in each $\sqrt{s'}$ interval. The values of and statistical errors on $\tilde{\sigma}^{\mu}_{+}$ and $\tilde{\sigma}^{\mu}_{-}$ were derived from the weighted sums. The error on the purity of the sample was taken into account in the systematic error. The numbers obtained are given as a function of $\sqrt{s'}$ in Table 17.

10 Fits to the Data

Fits to the data on the hadronic and leptonic cross-sections and the leptonic forward–backward asymmetries reported here, and to all the previously published DELPHI data [1,2] have been made. Full account was taken of the LEP energy uncertainties and their point–to–point and year–to–year correlations [5]. Allowance was also made for the correlations from year to year of the systematic errors in the measured cross-sections and asymmetries.

10.1 Model-Independent Fits

Before QED radiative corrections, it is possible to write the cross-section for $e^+e^- \rightarrow$ *hadrons*, $\sigma(s)$, in an almost model-independent form as

$$\sigma(s) = \sigma_0 \frac{s\Gamma_Z^2}{(s-M_Z^2)^2 + (s^2/M_Z^2)\Gamma_Z^2},$$

where M_Z and Γ_Z are respectively the Z^0 mass and width and σ_0 can be expressed in terms of the hadronic and electronic partial widths, Γ_{had} and Γ_e, as

$$\sigma_0 = \frac{12\pi\Gamma_e\Gamma_{had}}{M_Z^2\Gamma_Z^2}.$$

The leptonic partial widths Γ_f can be written in terms of effective vector and axial-vector coupling constants, g_{V_f} and g_{A_f}, as

$$\Gamma_l = \frac{G_F M_Z^3}{6\pi\sqrt{2}}(g_{V_l}^2 + g_{A_l}^2)(1+\delta_l^{QED}),$$

where $\delta_l^{(QED)}$ accounts for final state photonic corrections.

In order to fit the hadronic and leptonic cross-sections and the leptonic forward–backward asymmetries, the parameters M_Z, Γ_Z, σ_0, R_f and $A_{FB}^{0\,f}$ were chosen where

$$R_f = \frac{\Gamma_{had}}{\Gamma_f}$$

and

$$A_{FB}^{0\,f} = 3\frac{g_{V_e}g_{A_e}}{(g_{V_e}^2+g_{A_e}^2)}\frac{g_{V_f}g_{A_f}}{(g_{V_f}^2+g_{A_f}^2)}.$$

This set of parameters was chosen because they have small correlations between them and are therefore preferred for combining results from the different LEP experiments. To lowest order the forward-backward asymmetry in the reaction $e^+e^- \rightarrow f^+f^-$ at $\sqrt{(s)} = M_Z$ is given by $A_{FB}^{0\,f}$ and its variation away from the peak is mainly proportional to $g_{A_e}g_{A_f}$.

The program ZFITTER [20] was used to determine the parameters from fits to the experimental data. The theoretical formalism of ZFITTER takes account of the most up to date knowledge of initial and final state QED effects. According to the recommendation of the LEP Electroweak Working Group [29], $A_{\rm FB}^{0,f}$ is defined in terms of the real parts of the couplings, whereas the leptonic partial widths are defined in terms of their magnitudes. The differences are insignificant with present experimental uncertainties, but are in any case correctly taken into account in the fits. Corrections arising from γ exchange and hadronic γ-Z interference are calculated within the framework of the Standard Model.

Carrying out a 9–parameter fit, allowing independent couplings for the three lepton species, the parameters shown in Table 18 were obtained. The χ^2/DF of this fit was 179/168. The correlation coefficients for the parameters of this fit are given in Table 19. The uncertainty on $\Gamma_{\rm Z}$ includes a contribution of ± 0.0002 GeV, common to all LEP experiments, due to the uncertainty of ± 1 MeV on the LEP centre–of–mass energy spread. The uncertainty on $M_{\rm Z}$ also contains a contribution of 0.1 MeV due to the imprecise knowledge of the distance between the radio frequency stations in LEP points 2 and 6. However this error is totally anti-correlated between ALEPH and DELPHI and disappears when an average is made over the experiments.

Since the parameters are in good agreement with lepton universality, a 5-parameter fit assuming flavour independence of the couplings was performed. The resulting parameters are also given in Table 18. The χ^2/DF of this fit was 184/172. The correlation coefficients of the parameters of this fit are given in Table 20. Here R_l is defined for the $\rm Z^0$ decay into a pair of massless charged leptons and is treated consistently throughout. The results of the 9–parameter and 5–parameter fits are in good agreement with those published by the other LEP collaborations [30–32].

In Figure 18 the result of the 5–parameter fit is shown together with the DELPHI data on the hadronic cross-sections. In Figure 19 and Figure 20 respectively are shown the DELPHI data on leptonic cross-sections and forward–backward asymmetries, compared to the results of the 5–parameter fit. All the leptonic data shown are corrected for the acollinearity and momentum cuts and extrapolated to the full solid angle where necessary.

From the results of the preceeding fits the following parameters can be derived:

$$\begin{aligned} \Gamma_e &= 83.53 \pm 0.27 \text{ MeV} \\ \Gamma_\mu &= 84.34 \pm 0.41 \text{ MeV} \\ \Gamma_\tau &= 83.89 \pm 0.58 \text{ MeV} \end{aligned}$$

from the 9–parameter fits and

$$\begin{aligned} \Gamma_l &= 83.81 \pm 0.18 \text{ MeV} \\ \Gamma_{\rm inv} &= 498.7 \pm 3.4 \text{ MeV} \\ \Gamma_{\rm had} &= 1.7373 \pm 0.0041 \text{ GeV}. \end{aligned}$$

from the 5–parameter fits.

10.2 Fits of the Parameters of the S–Matrix

Within the framework of the S-Matrix approach [33], the total cross-section for e^+e^- annihilation into a fermion-antifermion pair, $\sigma^0_{\rm tot}(e^+e^- \to f\bar{f})$, as a function of centre-of-

mass energy $\sqrt{s}$ can be expressed as:

$$\sigma^0_{\rm tot}(s) \;=\; \frac{4}{3}\pi\alpha^2\left[\frac{g_f^{\rm tot}}{s}+\frac{s r_f^{\rm tot}+(s-\overline{M}_Z^2)j_f^{\rm tot}}{(s-\overline{M}_Z^2)^2+\overline{M}_Z^2\overline{\Gamma}_Z^2}\right],$$

where $g_f^{\rm tot}$ represents the photon exchange, $r_f^{\rm tot}$ the Z exchange and $j_f^{\rm tot}$ the γ-Z interference. Similarly, using the same functional form, a forward-backward asymmetric cross-section, $\sigma^0_{\rm fb}$ can be defined:

$$\sigma^0_{\rm fb}(s) \;=\; \frac{4}{3}\pi\alpha^2\left[\frac{g_f^{\rm fb}}{s}+\frac{s r_f^{\rm fb}+(s-\overline{M}_Z^2)j_f^{\rm fb}}{(s-\overline{M}_Z^2)^2+\overline{M}_Z^2\overline{\Gamma}_Z^2}\right].$$

The forward-backward asymmetry is then simply given by:

$$A_{\rm fb}(s) \;=\; \frac{3}{4}\frac{\sigma^0_{\rm fb}(s)}{\sigma^0_{\rm tot}(s)}.$$

The above S-Matrix expressions are based on a Breit-Wigner denominator with an s-independent width. The relationships to the parameters M_Z and Γ_Z used in the model independent fits of section 10.1, where an s-dependent width was assumed are:

$$\begin{aligned} M_Z &\equiv \overline{M}_Z\sqrt{1+\overline{\Gamma}_Z^2/\overline{M}_Z^2} \;\approx\; \overline{M}_Z + 34.1\ \text{MeV} \\ \Gamma_Z &\equiv \overline{\Gamma}_Z\sqrt{1+\overline{\Gamma}_Z^2/\overline{M}_Z^2} \;\approx\; \overline{\Gamma}_Z + \ 0.9\ \text{MeV}, \end{aligned} \tag{11}$$

so that $\Gamma_Z/M_Z = \overline{\Gamma}_Z/\overline{M}_Z$.

Allowing independent parameters for each of the lepton species, fits to the DELPHI cross-section and leptonic forward–backward asymmetry data were carried out using an option in the program ZFITTER [20]. The results are shown in Table 21. A χ^2/DF of 144/128 was obtained. The correlation coefficients for the parameters of this fit are given in Table 22.

If on the other hand universality of the lepton parameters is assumed then the results shown in Table 23 were obtained, with a χ^2/DF of 152/136. From Table 23 it can be seen that the parameters are in agreement with the Standard Model expectations. The correlation coefficients for the parameters of this fit are given in Table 24.

11 Interpretation of the Results

Assuming the Minimal Standard Model value for Γ_ν/Γ_l:

$$\Gamma_\nu/\Gamma_l \;=\; 1.991 \pm 0.001$$

(where the central value is evaluated for $M_Z = 91.1867$ GeV, $m_t = 174.1$ GeV [36,37], $m_H = 150$ GeV and the error quoted accounts for a variation of m_t in the range $m_t = 174.1 \pm 5.4$ GeV and a variation of m_H in the range $90 < m_H(\text{GeV}) < 300$), and using our result:

$$\Gamma_{\rm inv}/\Gamma_l \;=\; 5.950 \pm 0.036$$

the number of light neutrino species can be deduced. The result is:

$$N_\nu \;=\; 2.988 \pm 0.018.$$

Within the context of the Minimal Standard Model, a fit has been made to the DELPHI data, leaving the values of the top mass m_t and the strong coupling constant $\alpha_s(M_Z^2)$ as free parameters. The results are:

$$\begin{aligned} m_t &= 174^{+15+8}_{-17-5}\ \text{GeV} \\ \alpha_s(M_Z^2) &= 0.110 \pm 0.006 \pm 0.001. \end{aligned}$$

The central values were obtained assuming a Higgs boson mass m_H of 150 GeV, and the second uncertainty corresponds to the variation of m_H in the range $90 < m_H(\text{GeV}) < 300$. The QED coupling constant was taken as $\alpha(M_Z^2)^{-1} = 128.896 \pm 0.090$ [38]. The value of m_t is quite consistent with direct measurements [36,37], and the value of $\alpha_s(M_Z^2)$ is in agreement with other determinations [39].

The partial widths for the Z decay into leptons, and the lepton forward–backward asymmetries can be combined to determine the magnitudes of the effective vector and axial-vector couplings. As defined above the asymmetries depend upon the ratio g_{V_l}/g_{A_l} whereas the leptonic partial widths depend upon $(g_{V_l}^2 + g_{A_l}^2)$. The following values are obtained:

$$\begin{aligned} g_{V_l}^2 &= (1.58 \pm 0.16) \times 10^{-3} \\ g_{A_l}^2 &= 0.2506 \pm 0.0006. \end{aligned}$$

The leptonic vector and axial-vector couplings correspond to a value of the weak mixing angle of

$$\sin^2 \theta_{eff}^{lept} = 0.2301 \pm 0.0010.$$

An interesting question is to what extent the measured values of the total and partial widths allow for the possibility of decays of the Z^0 into yet unknown particles. If such particles are "invisible" this can be deduced in a straightforward manner from the comparison of the measured value of Γ_{inv} to its Standard Model prediction. Whether the new particles are visble or invisible, they will contribute to the measured value of Γ_Z. Confronting the measured values of Γ_{inv} and Γ_Z to their Standard Model predictions allows a derivation of upper limits on the extra partial widths ($\Gamma_{\text{inv}}^{\text{new}}$ and Γ_Z^{new}) related to new physics. The Standard Model predictions were computed for $m_t = 174.1 \pm 5.4$ GeV [36,37], $\alpha_s(M_Z^2) = 0.118 \pm 0.003$ [39], $\alpha(M_Z^2)^{-1} = 128.896 \pm 0.090$ [38] and $M_H = 150^{+150}_{-60}$ GeV. The following 95 % confidence level limits were obtained:

$$\begin{aligned} \Gamma_{\text{inv}}^{\text{new}} &< 2.8\ \text{MeV} \\ \Gamma_Z^{\text{new}} &< 2.9\ \text{MeV}. \end{aligned}$$

The situation may actually be more complicated, since the new decays may involve visible and invisible particles. They can enter into the selections of the different Z decay channels with unknown efficiencies, and therefore the measured partial widths are no longer reliable. On the other hand, since the e^+e^- and $\mu^+\mu^-$ channels each involve only two particles, carrying each near the beam energy, it is unlikely that a new decay mode would be wrongly assigned to these channels. Therefore, as suggested in ref. [34], we can base an estimate of the partial width, Γ^{new}, for decays into unknown particles on the assumption that the cross-section and asymmetry measurements in the e^+e^- and $\mu^+\mu^-$

channels are reliable. The analysis is done within the formalism of the ϵ parameters [35], so that no specific assumptions are made about loop corrections. The value of m_t is needed to evaluate the $b\bar{b}$ vertex, the other vertex corrections being assumed to behave normally.

Using the results of Section 10.1, we obtain for $\Gamma^{\rm new}$ and $\delta\Gamma_{\rm had}$ (the part of $\Gamma^{\rm new}$ leading to visible decays into hadronic final states):

$$\begin{aligned} \Gamma^{\rm new} &= -3.8 \pm 4.8 \text{ MeV} \\ \delta\Gamma_{\rm had} &= -1.8 \pm 6.0 \text{ MeV}. \end{aligned}$$

Normalizing over the physical region gives $\Gamma^{\rm new} < 7.2$ MeV at 95% confidence level.

12 Summary

DELPHI data from the LEP energy scans of 1993 and 1995 with precise monitoring of the beam energies, and those from a high statistics run in 1994 have been analysed in conjunction with data from previous years. The parameters of the Z^0 resonance have been determined with significantly improved precision. The analysis of $\mu^+\mu^-$ events with hard initial state photon observed in 1995 has been presented. When combined with published measurements from data of previous years, results on the cross-sections and forward backward asymmetries for $\sqrt{s}$ in the range 20–87 GeV have been obtained. All observations are consistent with the expectations of the Standard Model.

Acknowledgements

We are greatly indebted to our technical collaborators and to the funding agencies for their support in building and operating the DELPHI detector, and to the members of the CERN-SL Division for the excellent performance of the LEP collider.
We also acknowledge the support of
Austrian Federal Ministry of Science, Research and Arts,
FNRS–FWO, Belgium,
FINEP, CNPq, CAPES, FUJB and FAPERJ, Brazil,
Czech Ministry of Industry and Trade, GA CR 202/96/0450 and GA AVCR A1010521,
Danish Natural Research Council,
Commission of the European Communities (DG XII),
Direction des Sciences de la Matière, CEA, France,
Bundesministerium für Bildung, Wissenschaft, Forschung und Technologie, Germany,
General Secretariat for Research and Technology, Greece,
National Science Foundation (NWO) and Foundation for Research on Matter (FOM), The Netherlands,
Norwegian Research Council,
State Committee for Scientific Research, Poland, 2P03B00108, 2P03B03311 and 628/E–78–SPUB–P03–023/97,
JNICT–Junta Nacional de Investigação Científica e Tecnológica, Portugal,
Vedecka grantova agentura MS SR, Slovakia, Nr. 95/5195/134,
Ministry of Science and Technology of the Republic of Slovenia,
CICYT, Spain, AEN96–1661 and AEN96-1681,
The Swedish Natural Science Research Council,
Particle Physics and Astronomy Research Council, UK,

Department of Energy, USA, DE–FG02–94ER40817.

References

[1] DELPHI Collaboration, P. Abreu et al., Nucl. Phys. **B417** (1994) 3.
[2] DELPHI Collaboration, P. Abreu et al., Nucl. Phys. **B418** (1994) 403.
[3] L. Arnaudon et al., Z.Phys. **C66** (1995) 45.
[4] The working group on LEP energy, R. Assmann et al., Z. Phys. **C66** (1995) 567.
[5] The LEP Energy Working Group, R. Assmann et al., "Calibration of Centre–of–Mass Energies at LEP1 for Precise Measurements of Z properties", preprint CERN-EP/98-40 (1998), submitted to Eur. Phys. Journal C.
[6] L. Arnaudon et al., Phys.Lett.B307 (1993),187
[7] DELPHI Collaboration, P. Aarnio et al. , Nucl. Instr. & Meth. **A303** (1991) 233.
[8] DELPHI Collaboration, P. Abreu et al. , Nucl. Instr. & Meth. **A378** (1996) 57.
[9] S. Jadach, E. Richter–Was, B.F.L. Ward and Z. Was, Phys. Lett. **B353** (1995) 362; S. Jadach, W. Placzek and B.F.L. Ward, Phys. Lett. **B353** (1995) 349.
[10] R. Brun et al., "GEANT3", CERN report DD/EE/84–1 (1987), CERN Program Library Long Writeup W5013.
[11] F.A. Berends and R. Kleiss, Nucl. Phys. **B186** (1981) 22.
[12] F.A. Berends, W. Hollik and R.Kleiss, Nucl. Phys. **B304** (1988) 712.
[13] A.C.Benvenuti et al., "The DELPHI Small Angle Tile Calorimeter", contribution to IEEE NSS 1994, and references therein.
[14] T. Sjöstrand, Comp. Phys. Comm. **39** (1986) 347; M. Bengtsson and T. Sjüstrand, Comp. Phys. Comm. **43** (1987) 367.
[15] DELPHI Collaboration, P. Abreu at al., Z. Phys. **C77** (1996) 11.
[16] KORALZ S. Jadach, B.F.L. Ward and Z. Wąs, Comp. Phys. Comm. **66** (1991) 276.
[17] S. Nova, A. Olchevski and T. Todorov, "Monte Carlo event generator for two photon processes", DELPHI Note 90–35 (1990).
[18] G. Montagna et al., Nucl. Phys. **B401** (1993) 3, and Comput. Phys. Commun. **76** (1993) 328.
[19] W.J.P. Beenakker, F.A. Berends and S.C. van der Marck, Nucl. Phys. **B349** (1991) 323.
[20] "ZFITTER: An Analytical Program for Fermion Pair Production in e^+e^- Annihilation", D. Bardin et al., preprint CERN-TH 6443 (1992) and references therein. The version ZFITTER 5.0 is used for the fits reported in this paper.
[21] DELPHI Collaboration, P. Abreu at al., Z. Phys. **C75** (1997) 581.
[22] ALEPH Collaboration, R. Barate et al., Phys. Lett. **B399** (1997) 329; L3 Collaboration, M. Acciari et al., Phys. Lett. **B374** (1996) 331; OPAL Collaboration, P.D. Acton et al., Phys. Lett. **B273** (1991) 338.
[23] J.-M. Frêre, V.A. Novikov, M.I. Vysotsky, Phys. Lett. **B386** (1996) 437.
[24] J.E. Campagne and R. Zitoun, Z. Phys **C43** (1989) 469 and Proc. Radiative Corrections–Results and Perspectives, Brighton, 9–14 July 1989, p271.
[25] J. Hilgart, R. Kleis, Comp. Phys. Comm. **75** (1993) 191.
[26] DELPHI Collaboration, P. Abreu at al., Z. Phys. **C65** (1995) 603.
[27] Z. Was and S. Jadach, Phys. Rev. **D41** (1990) 1425.
[28] HRS Collaboration, M. Derrick et al., Phys. Rev. **D31** (1985) 2352; MAC Collaboration, W. W. Ash et al., Phys. Rev. Lett. **55** (1985) 1831;

TASSO Collaboration, W. Braunschweig et al., Z. Phys. **C40** (1988) 163;
CELLO Collaboration, H.-J. Behrend et al., Phys. Lett. **B191** (1987) 209;
JADE Collaboration, W. Bartel et al., Z. Phys. **C26** (1985) 507;
MARK J Collaboration, B. Adeva et al., Phys. Rev. **D38** (1988) 2665;
AMY Collaboration, A. Bacala et al., Phys. Lett. **B218** (1989) 112;
AMY Collaboration, C. Velissaris et al., Phys. Lett. **B331** (1994) 227;
TOPAZ Collaboration, B. Howell et al., Phys. Lett. **B291** (1992) 206;
VENUS: K. Miyabayashi, *Recent electroweak results from TRISTAN*, Proc. of the XXXth Rencontres de Moriond, Les Arcs, March 1995, ed. J. Trân Thanh Vân.

[29] LEP Electroweak Working Group Minutes (May 1995).

[30] ALEPH Collaboration, D. Buskulic et al., Z. Phys. **C62** (1994) 539.

[31] L3 Collaboration, M. Acciarri et al., Z. Phys **C62** (1994) 551.

[32] OPAL Collaboration, R. Akers et al., Z. Phys. **C61** (1994) 19.

[33] A. Leike, T. Riemann and J. Rose, Phys. Lett. **B273** (1991) 513;
T. Riemann, Phys. Lett. **B293** (1992) 451;
S. Kirsch and T. Riemann, Comp. Phys. Comm. **88** (1995) 89.

[34] K. Mönig, "Model Independent Limit of the Z-Decay-Width into Unknown Particles", preprint CERN/OPEN-97-040 (1997).

[35] G. Altarelli, R. Barbieri and F. Caravaglios, Nucl. Phys. **B349** (1995) 145.

[36] CDF Collaboration, J. Lys et al., "Top Mass Measurements at CDF", Proc. ICHEP96, Warsaw, 25–31 July 1996, p1196.

[37] D0 Collaboration, S. Abachi et al., Phys. Rev. Lett. **79** (1997) 1197.

[38] S. Eidelmann and F. Jegerlehner, Z. Phys. **C67** (1995) 585.

[39] R.M. Barnett et al., Phys. Rev. **D54** (1996) 1.

Year	Peak–2	cal. fills	Peak	cal. fills	Peak+2	cal. fills
1993	$10\,\mathrm{pb}^{-1}$	13/38(35%)	$20\,\mathrm{pb}^{-1}$	1/57(2%)	$10\,\mathrm{pb}^{-1}$	11/31(45%)
1994			$60\,\mathrm{pb}^{-1}$	11/167(8%)		
1995	$10\,\mathrm{pb}^{-1}$	14/22(69%)	$20\,\mathrm{pb}^{-1}$	1/14(6%)	$10\,\mathrm{pb}^{-1}$	13/23(65%)

Table 1: Dataset statistics per year and per energy point. The integrated luminosities are approximate, since the analyses of different channels required different selections of runs. The two values in the calibrated fills columns express the number of fills with at least one successful calibration divided by the total number of fills and the other shows the percentage of calibrated integrated luminosity.

Source of systematics	Contribution to $\frac{\Delta\mathcal{L}}{\mathcal{L}}$ (%)
Ring mask radius	0.02
ϕ mask acceptance	0.03
Unmasked acceptance borders	0.14
Interaction point $< z >$	0.10
Interaction point $< x, y >$ plus tilt	0.05
Energy cut	0.10
Data behind ϕ-mask	0.11
Less than 65% of energy in inner ring	0.01
Trigger efficiency	0.01
Off-momentum background	0.01
Monte Carlo statistics	0.04
Total experimental	0.24
Total theoretical	0.17
Total systematic uncertainty	0.29

Table 2: Contributions to the systematic uncertainty on the SAT absolute luminosity measurement.

Source of systematics	Contribution to $\frac{\Delta\mathcal{L}}{\mathcal{L}}$ (%)
errors in correction factors (uncorrelated part)	0.020
cut at the outer ring	0.015
cut at the inner edge	0.020
errors in measured parameters	0.015
energy cut	0.015
trigger efficiency and Bhabha selection	0.010
statistical error	0.050

Table 3: Contributions to the error of the VSAT luminosity measurement at the "peak+2" point.

Source of systematics	Contribution to $\frac{\Delta\mathcal{L}}{\mathcal{L}}$ (%)
IP position	0.06
Mask technique	0.04
MC statistics	0.03
R_A^{in} cut	0.02
R^{out} cut	0.02
Acoplanarity cut	0.01
Energy cut	0.03
Background subtraction	0.02
Trigger inefficiency	0.02
Total experimental	0.09
Total theoretical	0.11

Table 4: Contributions to the systematic error of the STIC luminosity measurement.

year	Collision energy (GeV)	Detector instabilities (%)	Forward inefficiencies (%)
1993	89.431	0.010 ± 0.005	0.16 ± 0.05
	91.187	0.11 ± 0.02	0.16 ± 0.05
	91.303	0.010 ± 0.005	0.16 ± 0.05
	93.015	0.010 ± 0.005	0.16 ± 0.05
1994	91.200	0.040 ± 0.010	0.18 ± 0.07
	91.204	0.019 ± 0.010	0.18 ± 0.07
1995	89.438	0.005 ± 0.002	0.10 ± 0.04
	91.278	0.003 ± 0.002	0.10 ± 0.04
	91.292	0.006 ± 0.002	0.10 ± 0.04
	92.965	0.004 ± 0.002	0.10 ± 0.04

Table 5: Corrections to the selection efficiencies for hadronic events due to detector instabilities and to detection and track reconstruction inefficiencies in the forward region not included in the Monte Carlo simulation. All corrections are negative. The uncertainties quoted are systematic.

Collision energy (GeV)	89.438	91.278	91.292	92.965
Monte Carlo statistics	0.02	0.02	0.02	0.02
forward inefficiency	0.04	0.04	0.04	0.04
off-peak efficiency correction	0.02	-	-	0.02
cut variations	0.08	0.08	0.08	0.08
total uncertainty on sel. eff.	0.09	0.09	0.09	0.09
$\tau^+\tau^-$ background	0.03	0.03	0.03	0.03
e^+e^- background	0.02	0.01	0.01	0.01
$\gamma\gamma$ collision background	0.03	0.01	0.01	0.02
total uncertainty	0.10	0.10	0.10	0.10

Table 6: Breakdown of the systematic uncertainties (in per-cent) on the 1995 hadronic cross-sections related to the knowledge of the selection efficiency and of the residual backgrounds.

year	Collision energy (GeV)	Cross-section (nb)
1993	89.431	9.868 ± 0.035
	91.187	30.351 ± 0.060
	91.303*	30.424 ± 0.098
	93.015	13.893 ± 0.041
1994	91.200	30.466 ± 0.034
	91.204	30.417 ± 0.152
1995	89.438	9.930 ± 0.038
	91.279	30.631 ± 0.105
	91.292*	30.650 ± 0.075
	92.965	14.348 ± 0.045

Table 7: DELPHI hadronic cross-sections measured from 1993 to 1995. In this and subsequent tables, data taken during the "pre-scan" operation is indicated with *. The uncertainties quoted are statistical. They do not include overall normalisation uncertainties coming from efficiencies and backgrounds (± 0.10% in 1993 and 1995, and ± 0.11 % in 1994) and from the absolute luminosity (± 0.29% in 1993 and ± 0.14% in 1994 and 1995).

year	Collision energy (GeV)	Cross-section (nb)	A^e_{FB}
1993	89.430	0.298 ± 0.008	-0.122 ± 0.028
	91.186	0.904 ± 0.011	0.028 ± 0.012
	91.303*	0.918 ± 0.014	-0.018 ± 0.016
	93.014	0.399 ± 0.007	0.089 ± 0.017
1994	91.201	0.910 ± 0.005	0.000 ± 0.006
1995	89.438	0.302 ± 0.009	-0.135 ± 0.030
	91.278	0.929 ± 0.017	0.011 ± 0.018
	91.292*	0.911 ± 0.012	0.002 ± 0.013
	92.965	0.435 ± 0.007	0.105 ± 0.017

Table 8: DELPHI cross-sections and forward–backward asymmetries measured in the e^+e^- channel. The results refer to the polar angle range $44° < \theta < 136°$. The cut on acollinearity given in the text applies to both sets of results which refer to the s–channel only. The uncertainties quoted are statistical. They do not include, for the cross-sections, overall normalization uncertainties coming from efficiencies and backgrounds (at the peak, $\pm 0.46\%$ in 1993 and $\pm 0.52\%$ in 1994 and 1995) and from the absolute luminosity ($\pm$ 0.29% in 1993 $\pm$ 0.14% in 1994 and $\pm$ 0.14% in 1995), and for the asymmetries a systematic uncertainty at the peak of ± 0.0026 in 1993, ± 0.0021 in 1994 and ± 0.0020 in 1995.

year	Collision energy (GeV)	Cross-section (nb)	A^μ_{FB}
1993	89.431	0.427 ± 0.007	-0.141 ± 0.015
	91.187	1.324 ± 0.012	-0.007 ± 0.008
	91.302*	1.354 ± 0.017	0.016 ± 0.013
	93.015	0.617 ± 0.008	0.104 ± 0.012
1994	91.200	1.331 ± 0.006	0.007 ± 0.004
1995	89.438	0.436 ± 0.007	-0.154 ± 0.016
	91.279	1.359 ± 0.018	0.020 ± 0.012
	91.292*	1.351 ± 0.013	0.000 ± 0.008
	92.965	0.649 ± 0.009	0.086 ± 0.012

Table 9: DELPHI cross-sections and forward–backward asymmetries measured in the $\mu^+\mu^-$ channel. The cross-sections are for the polar angle range $20° < \theta < 160°$ and the asymmetries refer to the full solid angle. The cuts on momenta and acollinearity given in the text apply to both sets of results. The uncertainties quoted are statistical. For the cross-sections they do not include overall normalization uncertainties coming from efficiencies and backgrounds ($\pm 0.28\%$ in 1993, $\pm 0.26\%$ in 1994 and $\pm 0.28\%$ in 1995.) and from the absolute luminosity (0.29% in 1993 and $\pm$ 0.14% in 1994 and 1995) . For the asymmetries there is a systematic uncertainty of ± 0.0009 in 1993, ± 0.0005 in 1994 and ± 0.0010 in 1995.

year	Collision energy (GeV)	Cross-section (nb)	$A_{\rm FB}^{\tau}$
1993	89.431	0.471 ± 0.009	-0.154 ± 0.020
	91.187	1.478 ± 0.015	-0.007 ± 0.011
	91.303*	1.503 ± 0.021	0.003 ± 0.017
	93.015	0.666 ± 0.011	0.112 ± 0.016
1994	91.200	1.480 ± 0.007	0.016 ± 0.005
1995	89.438	0.495 ± 0.010	-0.123 ± 0.019
	91.278	1.466 ± 0.023	-0.005 ± 0.015
	91.292*	1.462 ± 0.017	0.019 ± 0.011
	92.965	0.697 ± 0.011	0.122 ± 0.015

Table 10: DELPHI cross-sections and forward–backward asymmetries measured in the $\tau^+\tau^-$ channel. The cross-sections and asymmetries refer to the full solid angle and the cuts on momenta and acollinearity given in the text are corrected for. The uncertainties quoted are statistical. They do not include, for the cross-sections, overall normalization uncertainties coming from efficiencies and backgrounds ($\pm 0.60\%$) and from the absolute luminosity (0.29% in 1993 and $\pm$ 0.14% in 1994 and 1995) , and for the asymmetries a systematic uncertainty of ± 0.0020 at the peak.

	Hadrons	e^+e^-	$\mu^+\mu^-$	$\tau^+\tau^-$
Cross-section				
θ acceptance (°)	0-180	44-136	20-160	20-160
Selected events	682,262	24,286	28,888	21,920
Selection efficiency (%)	94.84 ± 0.09	97.82 ± 0.07	93.89 ± 0.26	61.99 ± 0.36
Trigger efficiency (%)	> 99.99	> 99.99	99.88 ± 0.01	99.98 ± 0.01
$\tau^+\tau^-$ background (%)	0.38 ± 0.03	1.10 ± 0.04	1.10 ± 0.11	–
$q\bar{q}$ background (%)	–	–	–	0.84 ± 0.15
$e^+e^- + \mu^+\mu^-$ bkgd. (%)	0.04 ± 0.01	–	–	1.60 ± 0.17
Two-photon bkgd. (pb)	16 ± 3	–	–	1.9 ± 0.5
Cosmic ray bkgd. (%)	–	–	0.11 ± 0.03	0.11 ± 0.05
Tot. syst. error (%)	± 0.10	$\pm 0.46^{\dagger}$	± 0.28	± 0.60
Asymmetry $A_{\rm FB}^{f}$				
θ acceptance (°)	–	44-136	11-169	20-160
Selected events		24,286	27,492	16,091
Tot. syst. error	–	$\pm 0.0026^{\dagger}$	± 0.0009	± 0.0020

Table 11: Summary of event samples, angular acceptances, efficiencies (within the acceptances for e^+e^- and $\mu^+\mu^-$) , backgrounds and systematic errors in the hadronic and leptonic cross-sections, and the leptonic forward–backward asymmetries for the 1993 data. The e^+e^- data refer specifically to analysis method 2. The total systematic uncertainty of $\pm 0.29\%$ in the luminosity is not included in the above numbers for the cross-sections. †Includes the uncertainty due to the t-channel subtraction.

	Hadrons	e^+e^-	$\mu^+\mu^-$	$\tau^+\tau^-$
Cross-section				
θ acceptance (°)	0-180	44-136	20-160	20-160
Selected events	1,310,243	41,290	56,856	39,133
Selection efficiency (%)	94.79 ± 0.10	96.95 ± 0.06	94.84 ± 0.25	63.79 ± 0.36
Trigger efficiency (%)	> 99.99	> 99.99	99.73 ± 0.01	99.98 ± 0.01
$\tau^+\tau^-$ background (%)	0.41 ± 0.03	0.83 ± 0.04	1.14 ± 0.06	–
$q\bar{q}$ background (%)	–	–	–	0.92 ± 0.10
$e^+e^- + \mu^+\mu^-$ bkgd. (%)	0.04 ± 0.01	–	–	2.07 ± 0.20
Two-photon bkgd. (pb)	16 ± 3	–	–	1.9 ± 0.2
Cosmic ray bkgd. (%)	–	–	0.07 ± 0.02	0.11 ± 0.05
Tot. syst. error (%)	± 0.11	$\pm 0.52^\dagger$	± 0.26	± 0.60
Asymmetry A_{FB}^f				
θ acceptance (°)	–	44-136	11-169	20-160
Selected events		41,290	58,532	39,133
Tot. syst. error	–	$\pm 0.0021^\dagger$	± 0.0005	± 0.0020

Table 12: Summary of event samples, angular acceptances, efficiencies (within the acceptances for e^+e^- and $\mu^+\mu^-$), backgrounds and systematic errors in the hadronic and leptonic cross-sections, and the leptonic forward–backward asymmetries for the 1994 data. The e^+e^- data refer specifically to analysis method 2. The total systematic uncertainty of $\pm 0.14\%$ in the luminosity is not included in the above numbers for the cross-sections. †Includes the uncertainty due to the t-channel subtraction.

	Hadrons	e^+e^-	$\mu^+\mu^-$	$\tau^+\tau^-$
Cross-section				
θ acceptance (°)	0-180	44-136	20-160	43-137
Selected events	659,331	20,833	26,211	18,787
Selection efficiency (%)	95.34 ± 0.09	97.42 ± 0.08	94.40 ± 0.26	62.00 ± 0.36
Trigger efficiency (%)	> 99.99	> 99.99	99.74 ± 0.01	99.98 ± 0.01
$\tau^+\tau^-$ background (%)	0.38 ± 0.03	0.85 ± 0.04	1.22 ± 0.10	–
$q\bar{q}$ background (%)	–	–	–	1.10 ± 0.15
$e^+e^- + \mu^+\mu^-$ bkgd. (%)	0.02 ± 0.01	–	–	1.39 ± 0.17
Two-photon bkgd. (pb)	16 ± 3	–	–	2.5 ± 0.2
Cosmic ray bkgd. (%)	–	–	0.09 ± 0.03	0.11 ± 0.05
Tot. syst. error (%)	± 0.10	$\pm 0.52^\dagger$	± 0.28	± 0.60
Asymmetry $A_{\rm FB}^f$				
θ acceptance (°)	–	44-136	11-169	43-137
Selected events		20,833	29,143	19,551
Tot. syst. error	–	$\pm 0.0020^\dagger$	± 0.0010	± 0.0020

Table 13: Summary of event samples, angular acceptances, efficiencies (within the acceptances for e^+e^- and $\mu^+\mu^-$), backgrounds and systematic errors in the hadronic and leptonic cross-sections, and the leptonic forward–backward asymmetries for the 1995 data. The e^+e^- data refer specifically to analysis method 2. The total systematic uncertainty of $\pm 0.14\%$ in the luminosity is not included in the above numbers.
†Includes the uncertainty due to the t-channel subtraction.

$q-\bar{q}$	1990	1991	1992	1993	1994	1995
1990	0.0040	0.0015	0.0008	0.0008	0.0008	0.0008
1991	0.0015	0.0020	0.0008	0.0008	0.0008	0.0008
1992	0.0008	0.0008	0.0013	0.0008	0.0008	0.0008
1993	0.0008	0.0008	0.0008	0.0010	0.0008	0.0008
1994	0.0008	0.0008	0.0008	0.0008	0.0010	0.0008
1995	0.0008	0.0008	0.0008	0.0008	0.0008	0.0010
e^+e^-	1990	1991	1992	1993	1994	1995
1990	0.0080	0.0050	0.0041	0.0041	0.0041	0.0041
1991	0.0050	0.0050	0.0041	0.0041	0.0041	0.0041
1992	0.0041	0.0041	0.0059	0.0041	0.0041	0.0041
1993	0.0041	0.0041	0.0041	0.0052	0.0041	0.0041
1994	0.0041	0.0041	0.0041	0.0041	0.0052	0.0041
1995	0.0041	0.0041	0.0041	0.0041	0.0041	0.0052
$\mu^+\mu^-$	1990	1991	1992	1993	1994	1995
1990	0.0080	0.0050	0.0040	0.0020	0.0020	0.0020
1991	0.0050	0.0050	0.0040	0.0020	0.0020	0.0020
1992	0.0040	0.0040	0.0040	0.0020	0.0020	0.0020
1993	0.0020	0.0020	0.0020	0.0031	0.0020	0.0020
1994	0.0020	0.0020	0.0020	0.0020	0.0028	0.0020
1995	0.0020	0.0020	0.0020	0.0020	0.0020	0.0030
$\tau^+\tau^-$	1990	1991	1992	1993	1994	1995
1990	0.0120	0.0075	0.0047	0.0047	0.0047	0.0047
1991	0.0075	0.0075	0.0047	0.0047	0.0047	0.0047
1992	0.0047	0.0047	0.0060	0.0047	0.0047	0.0047
1993	0.0047	0.0047	0.0047	0.0060	0.0047	0.0047
1994	0.0047	0.0047	0.0047	0.0047	0.0060	0.0047
1995	0.0047	0.0047	0.0047	0.0047	0.0047	0.0060

Table 14: The systematic errors due to selection efficiencies and background subtractions in the measurements of hadronic and leptonic cross-sections, and their correlations year-to-year. In the e^+e^- case the uncertainties apply to the s-channel. The systematic uncertainties due to the luminosity determination are not included.

e^+e^-	1990	1991	1992	1993	1994	1995
1990	0.0030	0.0020	0.0020	0.0016	0.0016	0.0016
1991	0.0020	0.0020	0.0020	0.0016	0.0016	0.0016
1992	0.0021	0.0020	0.0030	0.0016	0.0016	0.0016
1993	0.0016	0.0016	0.0016	0.0025	0.0016	0.0016
1994	0.0016	0.0016	0.0016	0.0016	0.0021	0.0016
1995	0.0016	0.0016	0.0016	0.0016	0.0016	0.0021
$\mu^+\mu^-$	1990	1991	1992	1993	1994	1995
1990	0.0050	0.0030	0.0010	0.0005	0.0005	0.0005
1991	0.0030	0.0030	0.0010	0.0005	0.0005	0.0005
1992	0.0010	0.0010	0.0010	0.0005	0.0005	0.0005
1993	0.0005	0.0005	0.0005	0.0009	0.0005	0.0005
1994	0.0005	0.0005	0.0005	0.0005	0.0005	0.0005
1995	0.0005	0.0005	0.0005	0.0005	0.0005	0.0015
$\tau^+\tau^-$	1990	1991	1992	1993	1994	1995
1990	0.0050	0.0020	0.0010	0.0015	0.0015	0.0015
1991	0.0020	0.0020	0.0010	0.0015	0.0015	0.0015
1992	0.0010	0.0010	0.0017	0.0015	0.0015	0.0015
1993	0.0015	0.0015	0.0015	0.0020	0.0015	0.0015
1994	0.0015	0.0015	0.0015	0.0015	0.0020	0.0015
1995	0.0015	0.0015	0.0015	0.0015	0.0015	0.0020

Table 15: The systematic errors in the measurements of leptonic forward-backward asymmetries, and their correlations year-to-year. In the e^+e^- case the uncertainties apply to the s-channel.

$\sqrt{s'}$ [GeV]	24-38	38-45	45-52	52-59	59-66	66-73	73-80	80-84	84-87
N_{obs}^{95}	2	9	2	5	5	7	11	16	43
N_{sim}^{95}	14	44	27	47	33	45	108	193	466
$<\sigma_{IB}^{obs}>/<\sigma_{IB}^{SM}>$	0.92	1.56	0.59	1.04	0.83	1.15	0.95	0.82	0.97
1995	$\pm$1.03	$\pm$0.62	$\pm$0.59	$\pm$.59	$\pm$0.68	$\pm$0.52	$\pm$0.31	$\pm$0.20	$\pm$0.15
$<\sigma_{IB}^{obs}>/<\sigma_{IB}^{SM}>$	1.14	0.99	1.01	0.76	0.56	1.05	0.93	0.90	1.11
1992-1995	$\pm$0.49	$\pm$0.23	$\pm$0.33	$\pm$0.21	$\pm$0.18	$\pm$0.23	$\pm$0.14	$\pm$0.11	$\pm$0.06
$<\sqrt{s'}>$ [GeV]	33.6	41.7	47.5	55.6	62.1	70.2	77.4	82.5	85.8
σ_{IB}^{SM} [pb]	86.6	56.5	43.9	32.9	27.6	24.9	29.6	49.8	106.1
σ_{IB}^{obs} [pb](92-95)	98.7	55.9	44.3	25.0	15.5	26.1	27.5	44.8	117.8
$\delta(\sigma_{IB}^{obs})$ [pb](92-95)	$\pm$42.4	$\pm$13.0	$\pm$14.5	$\pm$6.9	$\pm$5.0	$\pm$5.7	$\pm$4.1	$\pm$5.5	$\pm$6.4

Table 16: Numbers of ISR events found in the 1995 data and simulated samples (N_{obs}^{95} and N_{sim}^{95}) for different $\sqrt{s'}$ intervals, and the ratios of the average measured to SM Improved Born cross-sections for 1995. Next the cross-section ratio for the data taken in 1992 to 1995 is given. Then $<\sqrt{s'}>$ is the mean measured effective annihilation energy in the interval, and σ_{IB}^{SM} is the mean Improved Born cross-section within each energy interval expected in the Standard Model, obtained from the DYMU3 program. Finally σ_{IB}^{obs} with its error $\delta(\sigma_{IB}^{obs})$ is the resulting measured cross-section.

$\sqrt{s'}$ [GeV]	20-50	50-65	65-80	80-84	84-87
N_F^{95}	9	6	4	4	17
N_B^{95}	6	8	19	17	34
$P_{\gamma\gamma}$	0.10	0.07	0.01	0.	0.
$A_{FB}^{\gamma\gamma}$ [%]	-49.	-24.	-75.		
$< \sqrt{s'} >$ [GeV]	42.5	58.9	74.4	82.4	85.9
$A_{FB}^{fit}corr$ [%]	14.3 ± 14.4	-37.4 ± 15.6	-68.2 ± 7.0	-63.3 ± 8.4	-45.3 ± 6.2
$\delta(A_{FB})_{sys}^{fit}$[%]	± 0.4	± 0.6	± 0.7	± 0.6	± 0.3
$\tilde{\sigma}_+^\mu/\tilde{\sigma}_-^\mu$	1.54 ± 0.55	0.34 ± 0.17	0.09 ± 0.05	0.10 ± 0.06	0.23 ± 0.05
δ_{sys}	0.05	0.01	0.01	0.01	0.01

Table 17: N_F^{95}, N_B^{95}: observed number of ISR events in the forward and backward hemispheres for the 1995 data; $P_{\gamma\gamma}$: contamination by $\gamma\gamma$ events; $A_{FB}^{\gamma\gamma}$: asymmetry for $\gamma\gamma$ events as determined from simulated data; $A_{FB}^{fit}corr$: the asymmetry with statistical error calculated with a maximum likelihood fit, corrected for FSR and $\gamma\gamma$ contamination, with systematic error $\delta(A_{FB})_{sys}^{fit}$, based on the data from 1991 to 1995; ; $\tilde{\sigma}_+^\mu/\tilde{\sigma}_-^\mu$: the helicity component ratio with its statistical error based on the data from 1991 to 1995; δ_{sys}: the systematic error on the above helicity component ratio .

Parameter	Value
M_Z	91.1864 ± 0.0029
Γ_Z	2.4872 ± 0.0041
σ_0	41.553 ± 0.079
R_e	20.87 ± 0.12
R_μ	20.67 ± 0.08
R_τ	20.78 ± 0.13
R_l	20.728 ± 0.060
$A_{FB}^{0\,e}$	0.0189 ± 0.0048
$A_{FB}^{0\,\mu}$	0.0160 ± 0.0025
$A_{FB}^{0\,\tau}$	0.0243 ± 0.0037
A_{FB}^{0}	0.0187 ± 0.0019

Table 18: The results of the 9-parameter and 5-parameter fits to all DELPHI data on hadronic and leptonic cross-sections and leptonic forward-backward asymmetries.

	Γ_Z	σ_0	R_e	R_μ	R_τ	$A_{FB}^{0\,e}$	$A_{FB}^{0\,\mu}$	$A_{FB}^{0\,\tau}$
M_Z	0.05	-0.06	-0.03	-0.06	-0.03	0.04	0.07	0.07
Γ_Z	–	-0.24	-0.01	-0.01	0.00	0.00	0.00	0.00
σ_0		–	0.11	0.17	0.10	0.00	-0.01	-0.01
R_e			–	0.06	0.04	0.01	0.00	0.00
R_μ				–	0.05	0.00	0.01	0.00
R_τ					–	0.00	0.00	0.02
$A_{FB}^{0\,e}$						–	0.01	0.01
$A_{FB}^{0\,\mu}$							–	0.02

Table 19: The correlation coefficients for the parameters of the 9-parameter fit.

	Γ_Z	σ_0	R_l	A_{FB}^{0}
M_Z	0.05	-0.06	-0.06	0.09
Γ_Z	–	-0.24	-0.01	0.00
σ_0		–	0.22	-0.01
R_l			–	0.01

Table 20: The correlation coefficients for the parameters of the 5-parameter fit.

Parameter	Value
M_Z (GeV)	91.1942±0.0115
Γ_Z (GeV)	2.4849±0.0048
r_{had}^{tot}	2.945±0.011
r_e^{tot}	0.1408±0.0010
r_μ^{tot}	0.14241±0.00073
r_τ^{tot}	0.14146±0.00100
j_{had}^{tot}	-0.28±0.65
j_e^{tot}	-0.064±0.053
j_μ^{tot}	0.053±0.043
j_τ^{tot}	-0.008±0.047
r_e^{fb}	0.00340±0.00092
r_μ^{fb}	0.00276±0.00051
r_τ^{fb}	0.00418±0.00072
j_e^{fb}	0.816±0.073
j_μ^{fb}	0.712±0.037
j_τ^{fb}	0.705±0.047

Table 21: S-Matrix parameters from a fit to all the DELPHI data without the assumption of lepton universality.

	Γ_Z	r_{had}^{tot}	r_e^{tot}	r_μ^{tot}	r_τ^{tot}	j_{had}^{tot}	j_e^{tot}	j_μ^{tot}	j_τ^{tot}	r_e^{fb}	r_μ^{fb}	r_τ^{fb}	j_e^{fb}	j_μ^{fb}	j_τ^{fb}
M_Z	-.51	-.46	-.26	-.32	-.25	-.97	-.58	-.71	-.65	.16	.25	.17	-.04	.00	.00
Γ_Z	–	.88	.51	.66	.48	.54	.29	.40	.36	-.07	-.11	-.07	.04	.04	.03
r_{had}^{tot}		–	.53	.69	.51	.49	.26	.36	.32	-.06	-.10	-.06	.04	.05	.04
r_e^{tot}			–	.40	.29	.28	.19	.20	.19	-.02	-.06	-.04	.08	.03	.02
r_μ^{tot}				–	.38	.34	.18	.33	.23	-.04	-.05	-.04	.03	.08	.03
r_τ^{tot}					–	.27	.14	.20	.25	-.03	-.05	.00	.02	.03	.09
j_{had}^{tot}						–	.57	.71	.65	-.16	-.25	-.16	.04	.00	.01
j_e^{tot}							–	.42	.38	-.07	-.15	-.10	.02	.00	.00
j_μ^{tot}								–	.48	-.11	-.16	-.12	.03	-.04	.00
j_τ^{tot}									–	-.10	-.17	-.09	.03	.00	-.03
r_e^{fb}										–	.05	.03	.08	.00	.00
r_μ^{fb}											–	.05	.01	.20	.00
r_τ^{fb}												–	.01	.00	.18
j_e^{fb}													–	.00	.00
j_μ^{fb}														–	.00

Table 22: The correlation matrix for the set of parameters given in Table 21.

Parameter	Value	SM prediction
M_Z (GeV)	91.1944±0.0115	–
Γ_Z (GeV)	2.4846±0.0048	2.4932
r_{had}^{tot}	2.944±0.011	2.9603
r_ℓ^{tot}	0.14177±0.00065	0.14253
j_{had}^{tot}	-0.29±0.65	0.22
j_ℓ^{tot}	0.008±0.037	0.004
r_ℓ^{fb}	0.00325±0.00039	0.00266
j_ℓ^{fb}	0.725±0.027	0.799

Table 23: S-Matrix parameters from a fit to all the DELPHI data assuming lepton universality. The Standard Model predictions are calculated for $M_Z = 91.1882$ GeV, $m_t = 174.1$ GeV, $m_H = 300$ GeV, $\alpha_s(M_Z^2) = 0.118$ and $1/\alpha(M_Z^2) = 128.896$.

	Γ_Z	r_{had}^{tot}	r_ℓ^{tot}	j_{had}^{tot}	j_ℓ^{tot}	r_ℓ^{fb}	j_ℓ^{fb}
M_Z	-.511	-.46	-.38	-.97	-.83	.33	-.01
Γ_Z	–	.88	.74	.54	.45	-.15	.07
r_{had}^{tot}		–	.78	.49	.41	-.13	.07
r_ℓ^{tot}			–	.40	.37	-.09	.10
j_{had}^{tot}				–	.82	-.32	.02
j_ℓ^{tot}					–	-.26	-.01
r_ℓ^{fb}						–	.17

Table 24: The correlation matrix for the set of parameters given in Table 23.

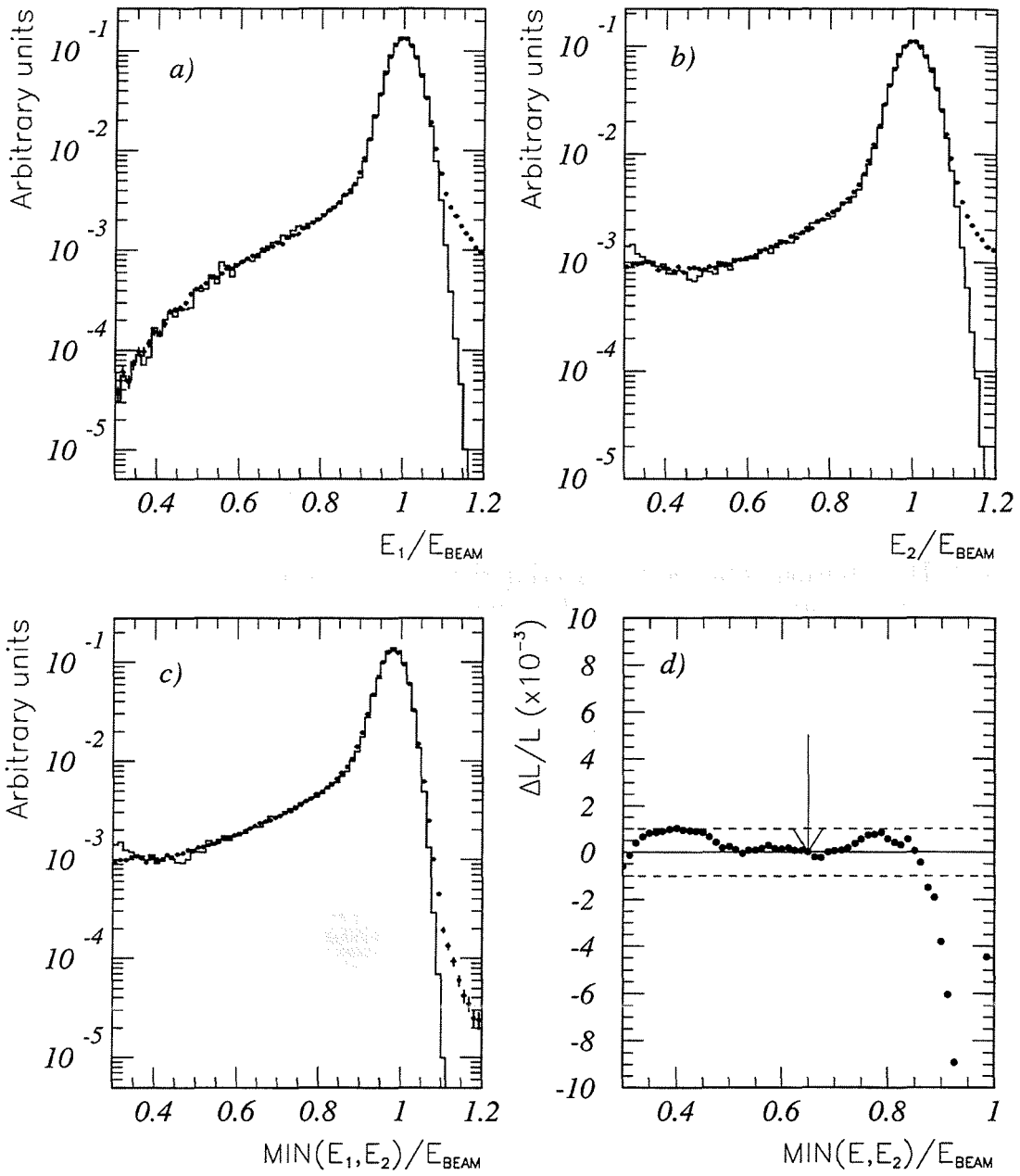

Figure 1: (a), (b) The relative energy distributions in the two SAT calorimeters separately and (c) the relative minimum energy distribution for data (points) and simulated data (histograms) after all other event selection criteria have been applied. (d) The variation of the measured luminosity with respect to the placement of the minimum energy cut. The luminosity change is defined to be zero at the standard cut of 65% of the beam energy, indicated by the arrow.

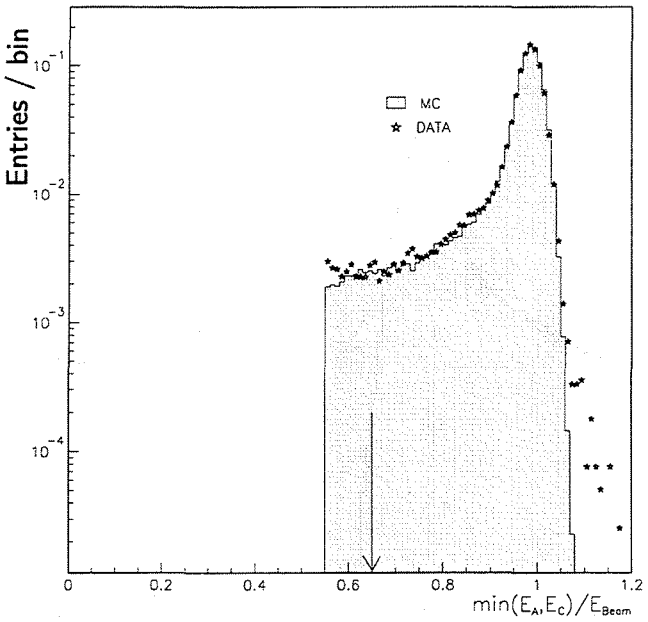

Figure 2: Distribution obtained by selecting the highest energy cluster in each of the two STIC arms and plotting the lower of these two.

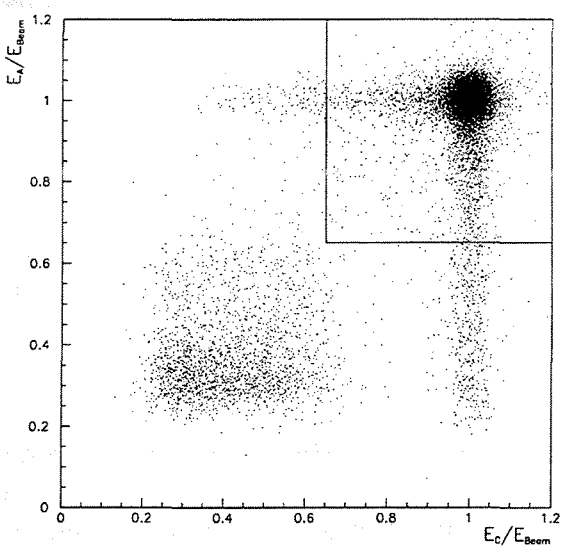

Figure 3: Distribution of the highest energy cluster of one STIC arm versus the highest energy cluster of the other: the selected region is indicated by the line.

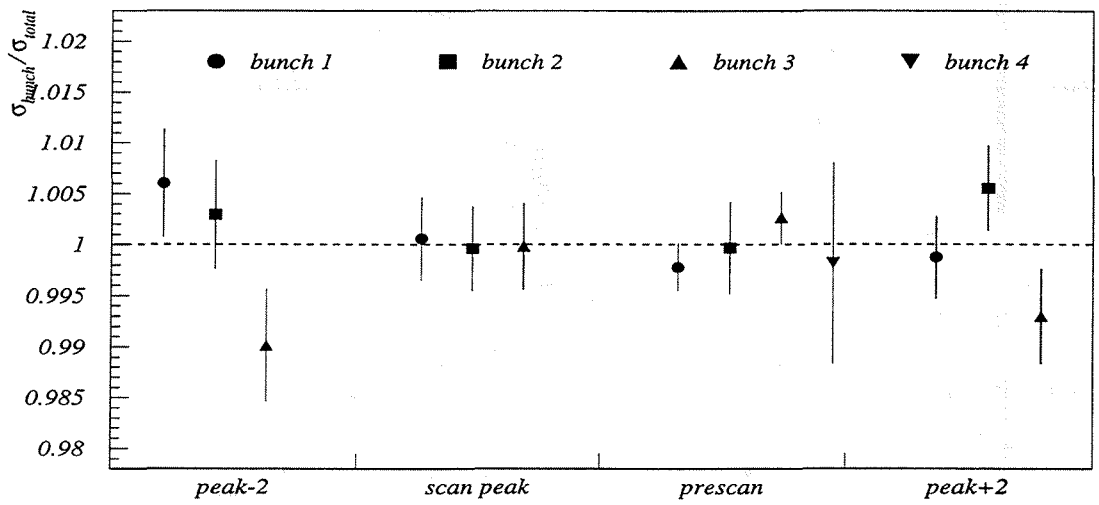

Figure 4: Cross-section per bunch divided by the total cross-section at each collision energy in 1995.

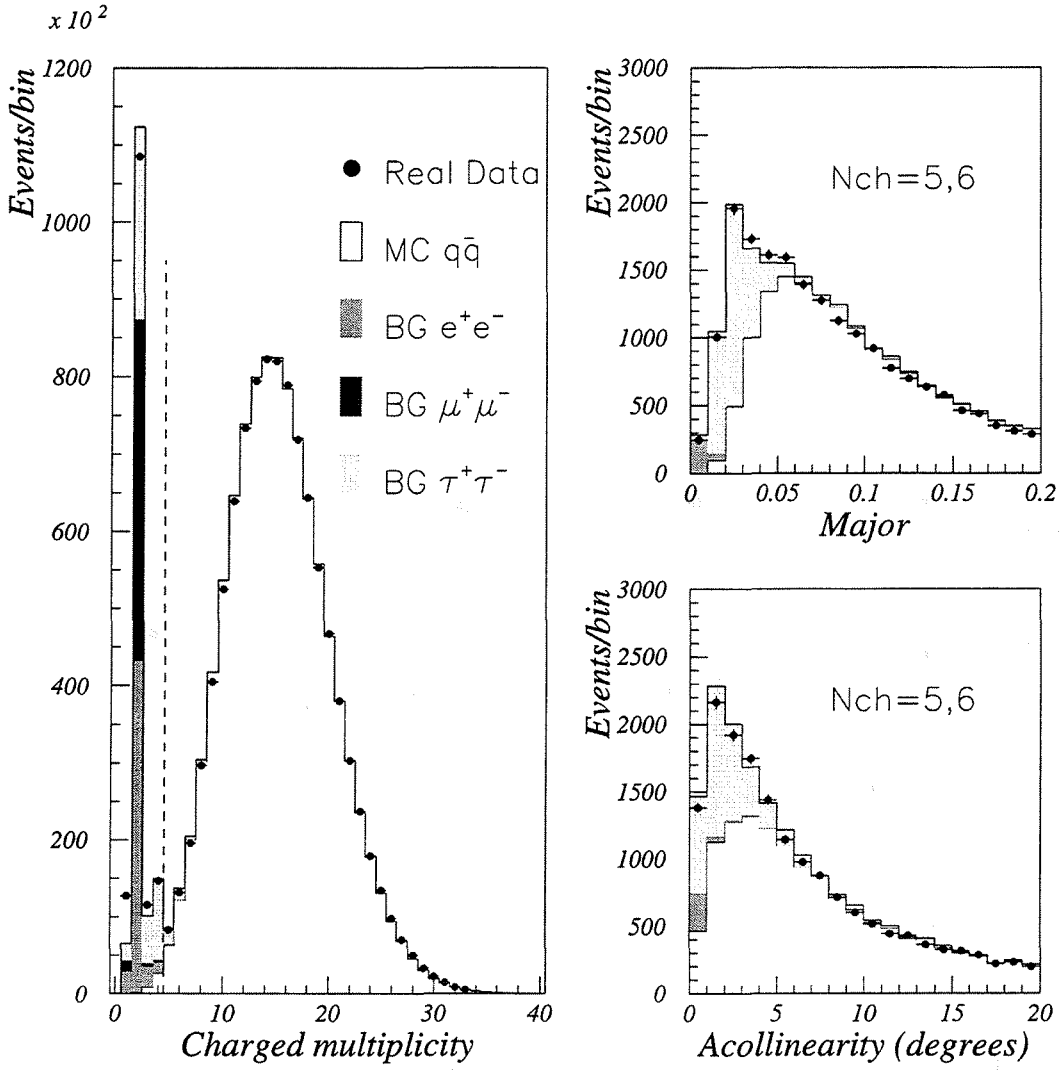

Figure 5: Distribution of the charged multiplicity, of the acollinearity between the momenta of both event hemispheres and of the major value of the transverse momentum with respect to the event thrust axis, for hadronic events at the peak energy. The multiplicity distribution is shown for events satisfying all other selection criteria, the dashed vertical line showing the charged multiplicity cut. The acollinearity and the major distributions are restricted to selected events with charged multiplicity 5 and 6. Points with error bars represent the real data. The white area under the full line stands for the $q\bar{q}$ Monte Carlo. The shaded areas show the contributions from the main background processes visible on these distributions: $\tau^+\tau^-$ pairs (light grey), e^+e^- pairs (dark grey) and $\mu^+\mu^-$ pairs (medium grey).

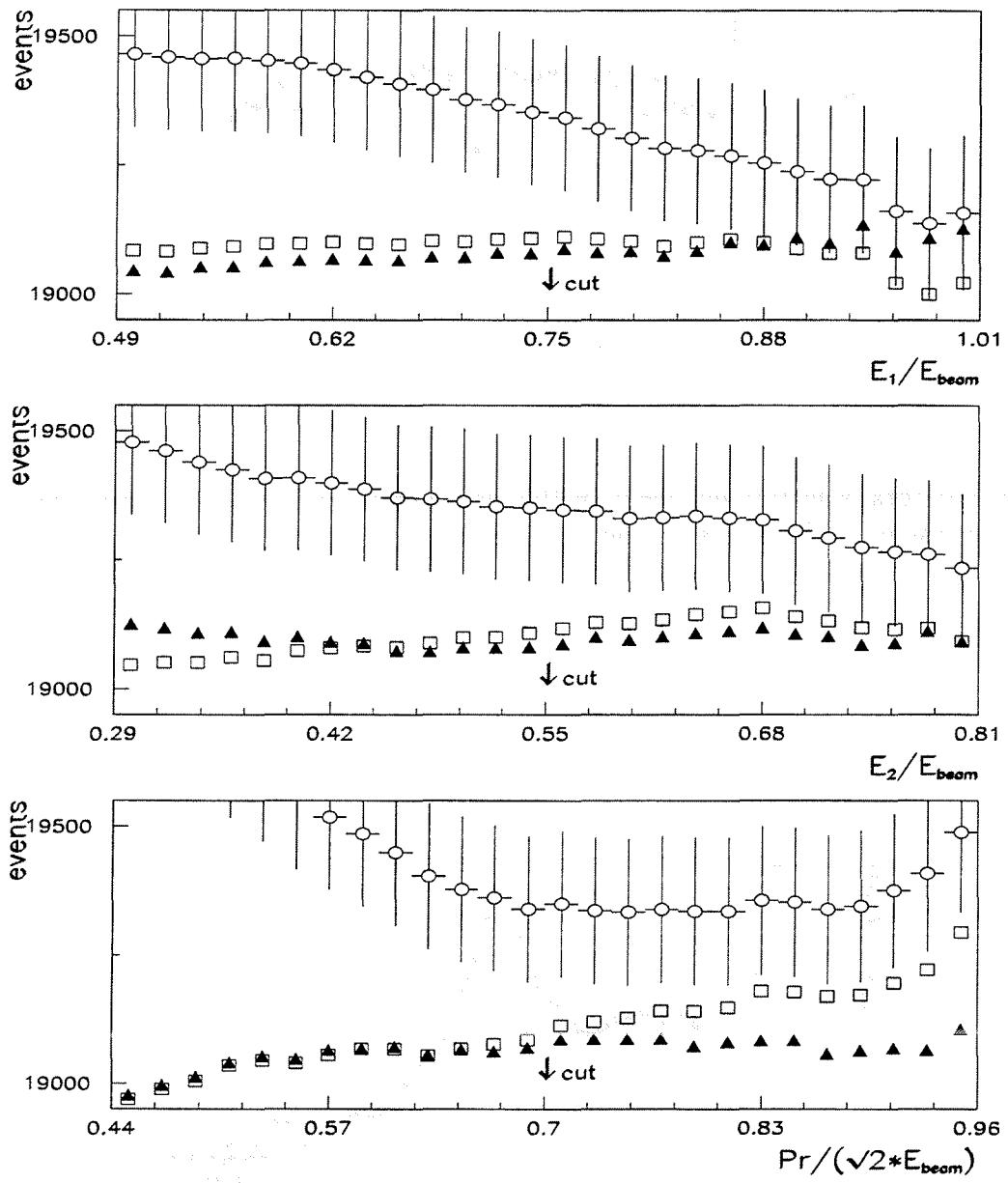

Figure 6: Total number of e^+e^- events estimated by method 2 at the scan energies, as a function of some of the cut variables: a) energy of the most energetic electromagnetic cluster, normalized to the beam energy b) energy of the second most energetic electromagnetic cluster, normalized to the beam energy c) quadratic sum of the momenta of the two highest momentum charged particles. The circles give the estimated number of events after efficiency correction (the statistical error is shown), the squares after background subtraction and the triangles after correlation correction. The chosen cut value is indicated with an arrow.

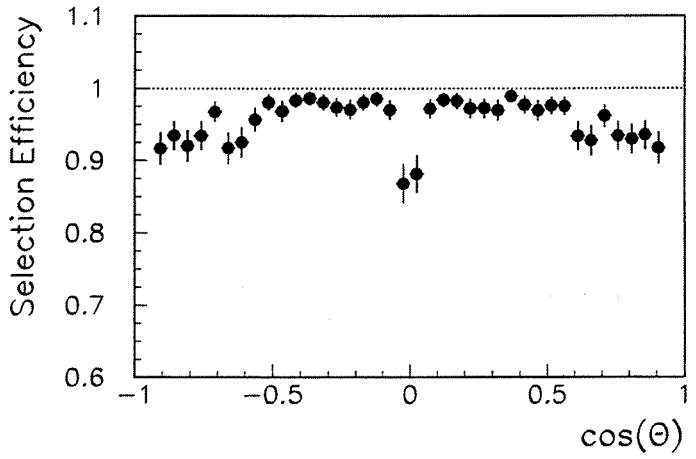

Figure 7: The total selection efficiency in 1994 for events $e^+e^- \to \mu^+\mu^-$ versus the cosine of the polar angle for the fastest muon.

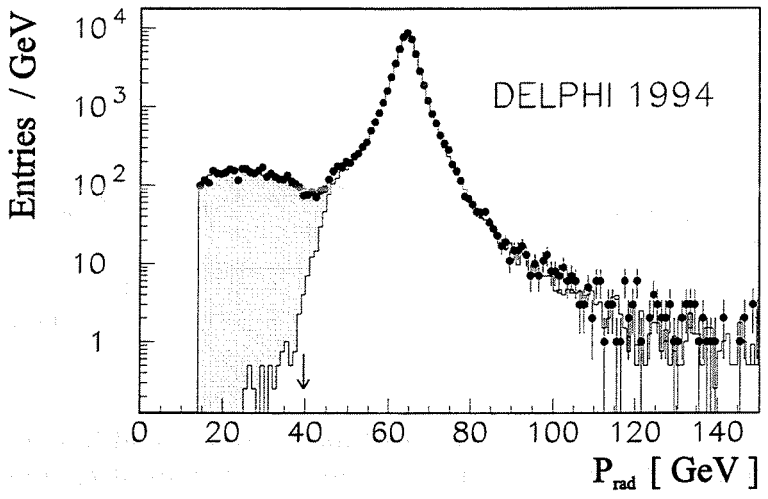

Figure 8: Distribution of the event variable P_{rad} for data from the 1994 runing period (points) and fitted Monte Carlo. The unshaded area is $\mu^+\mu^-$, the shaded area is $\tau^+\tau^-$. The arrow indicates the cut applied in the final event selection.

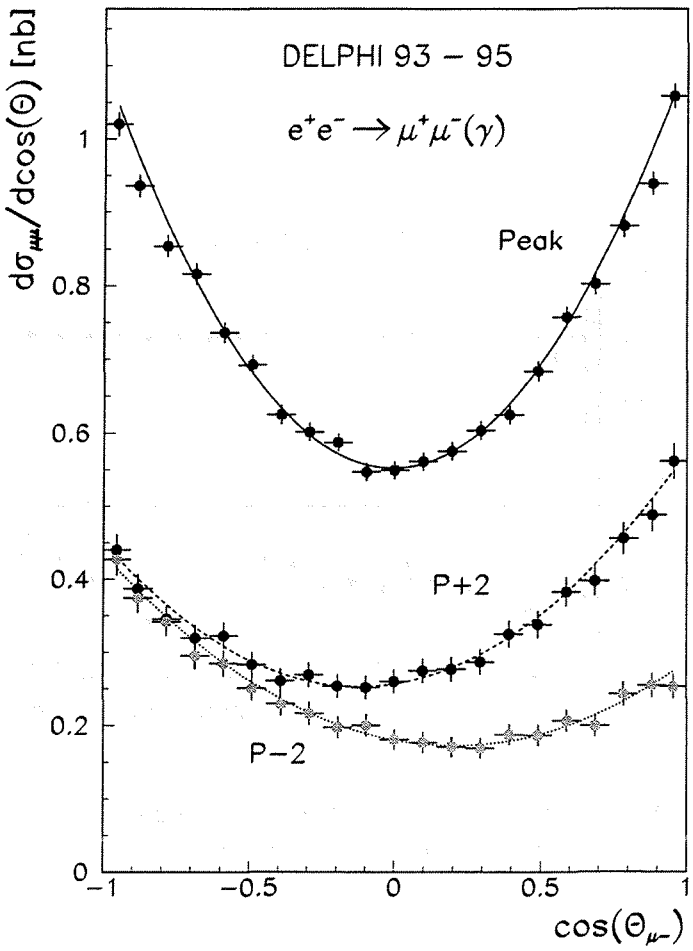

Figure 9: Differential cross-sections of the reaction $e^+e^- \rightarrow \mu^+\mu^-$ combined for all years 1993 to 1995. The superimposed curves are fits to the data points assuming the lowest order form of the differential cross-section

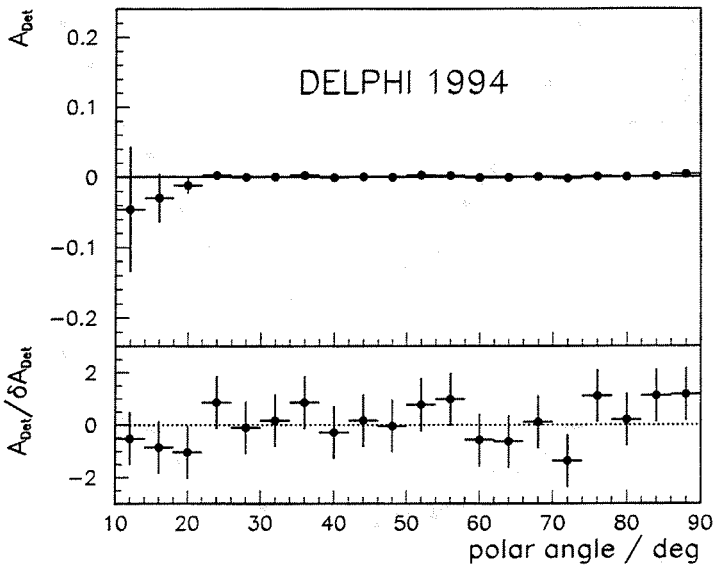

Figure 10: Detector Asymmetry A_{det} versus the polar angle as determined for the 1994 running period, both as an absolute quantity, and normalized by its statistical error, δA_{det}.

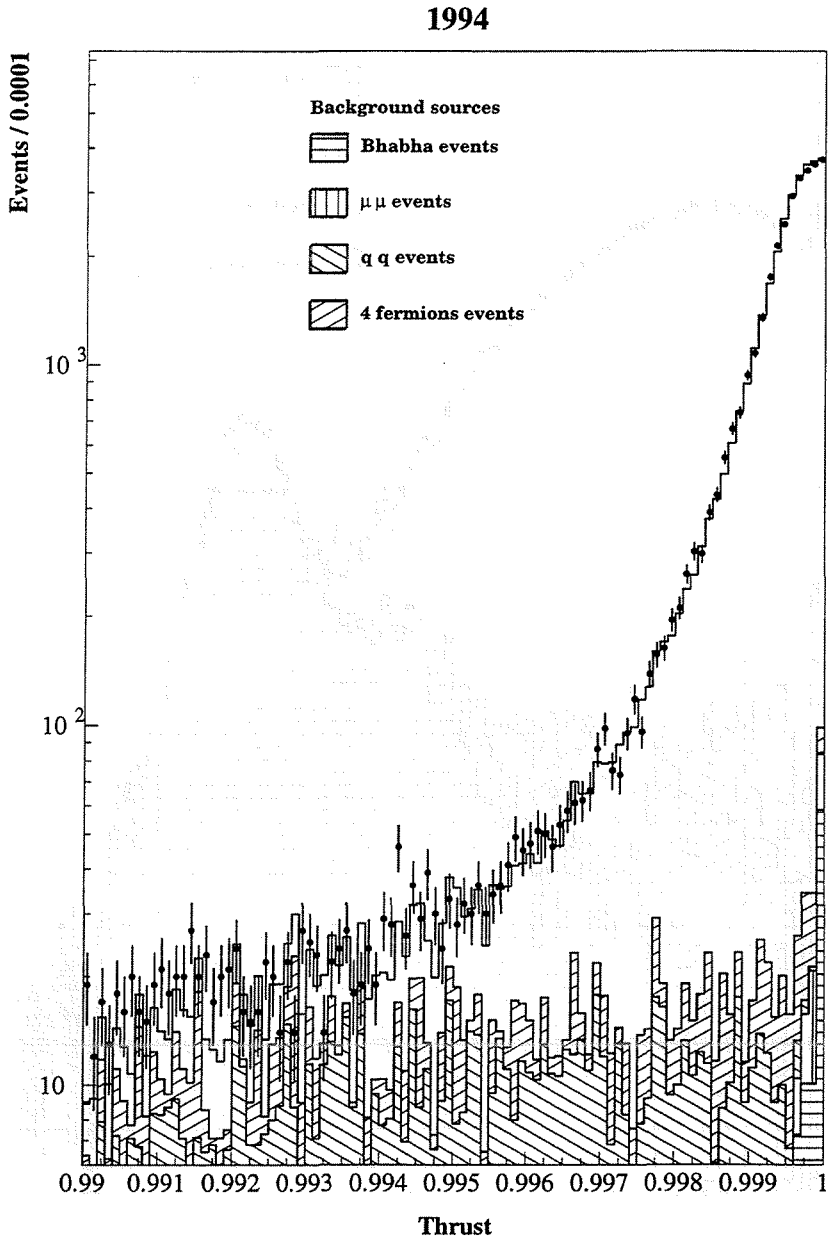

Figure 11: The distribution of the thrust variable in events selected as $\tau^+\tau^-$ in 1994. The points are for the data, the open area is for simulated $\tau^+\tau^-$ events and the cross-hatched areas represents the simulated background from all sources. Only events with Thrust $>$ 0.996 are retained. The plot shows that signal and backgrounds are well reproduced by the simulation.

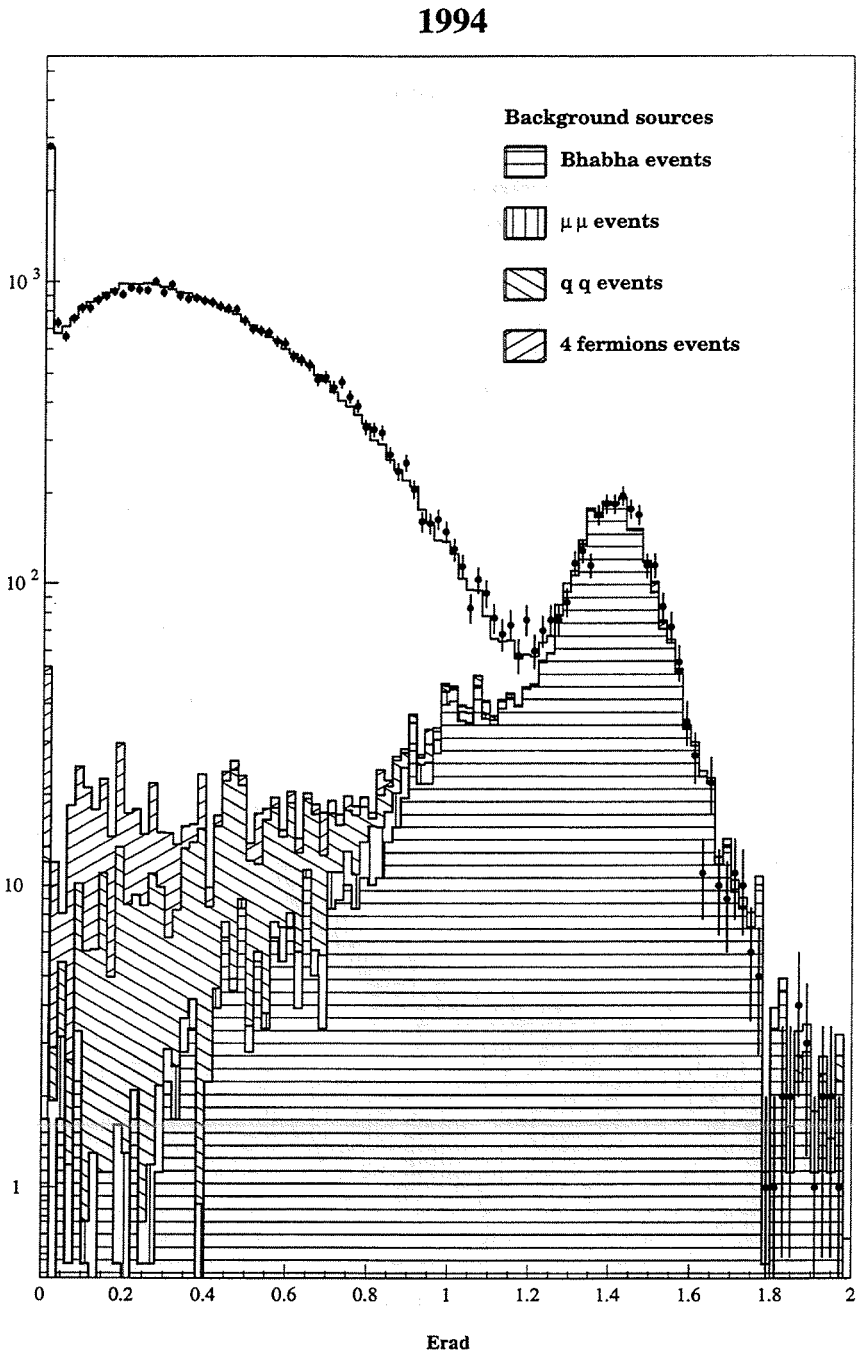

Figure 12: The distribution of the E_{rad} variable in events selected as $\tau^+\tau^-$ in 1994. The points are for the data, the open area is for simulated $\tau^+\tau^-$ events and the cross-hatched areas represent the simulated backgrounds from all sources. Only events with $E_{rad} < \sqrt{s}/2$ are retained. The plot shows that signal and backgrounds are well reproduced by the simulation.

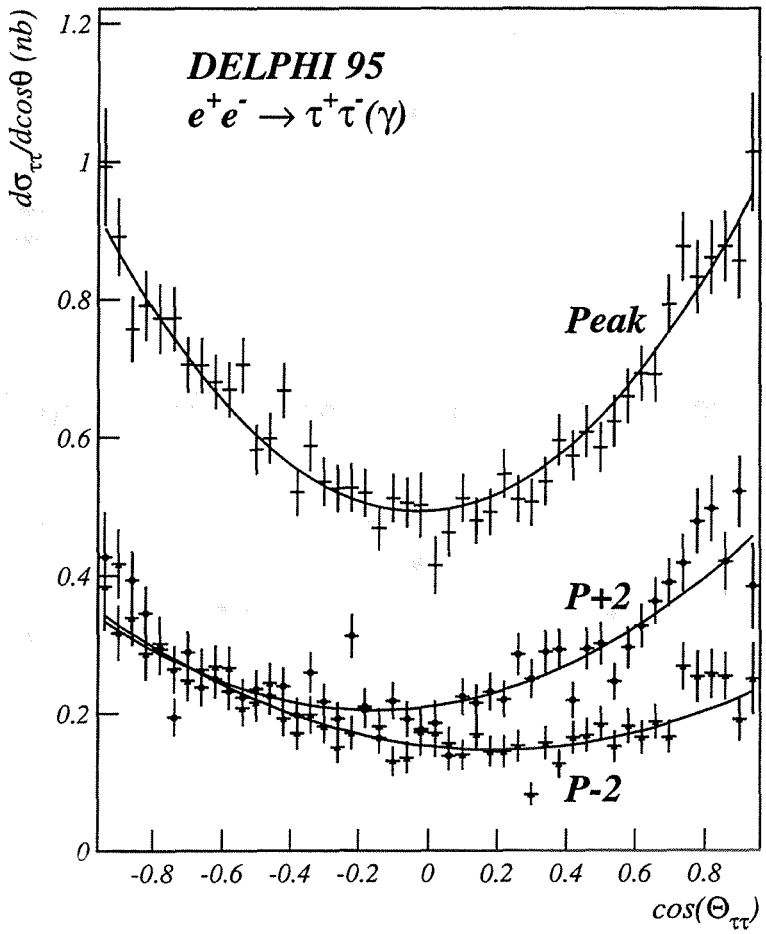

Figure 13: Differential cross-sections in the $\tau^+\tau^-$ channel as measured at the three energy values in 1995. The curves are fits to the lowest order form of the angular distribution.

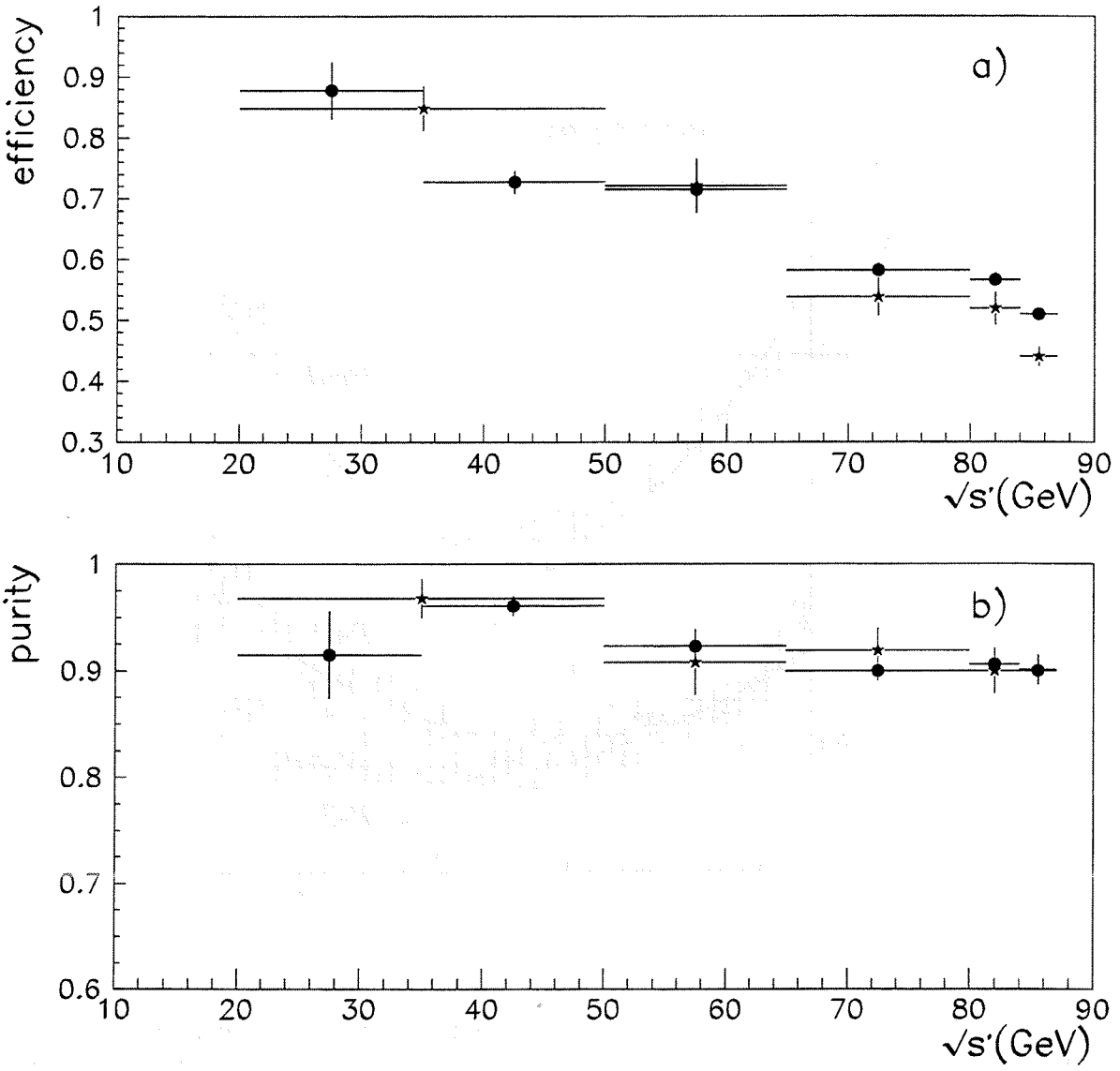

Figure 14: **(a)** Efficiency for the selection of ISR events and **(b)** purity of the ISR sample with regard to FSR events, based on simulated radiative muon events, for the data sample used in ref. [21] (*black dots*) and for the data taken in 1995 (*stars*)

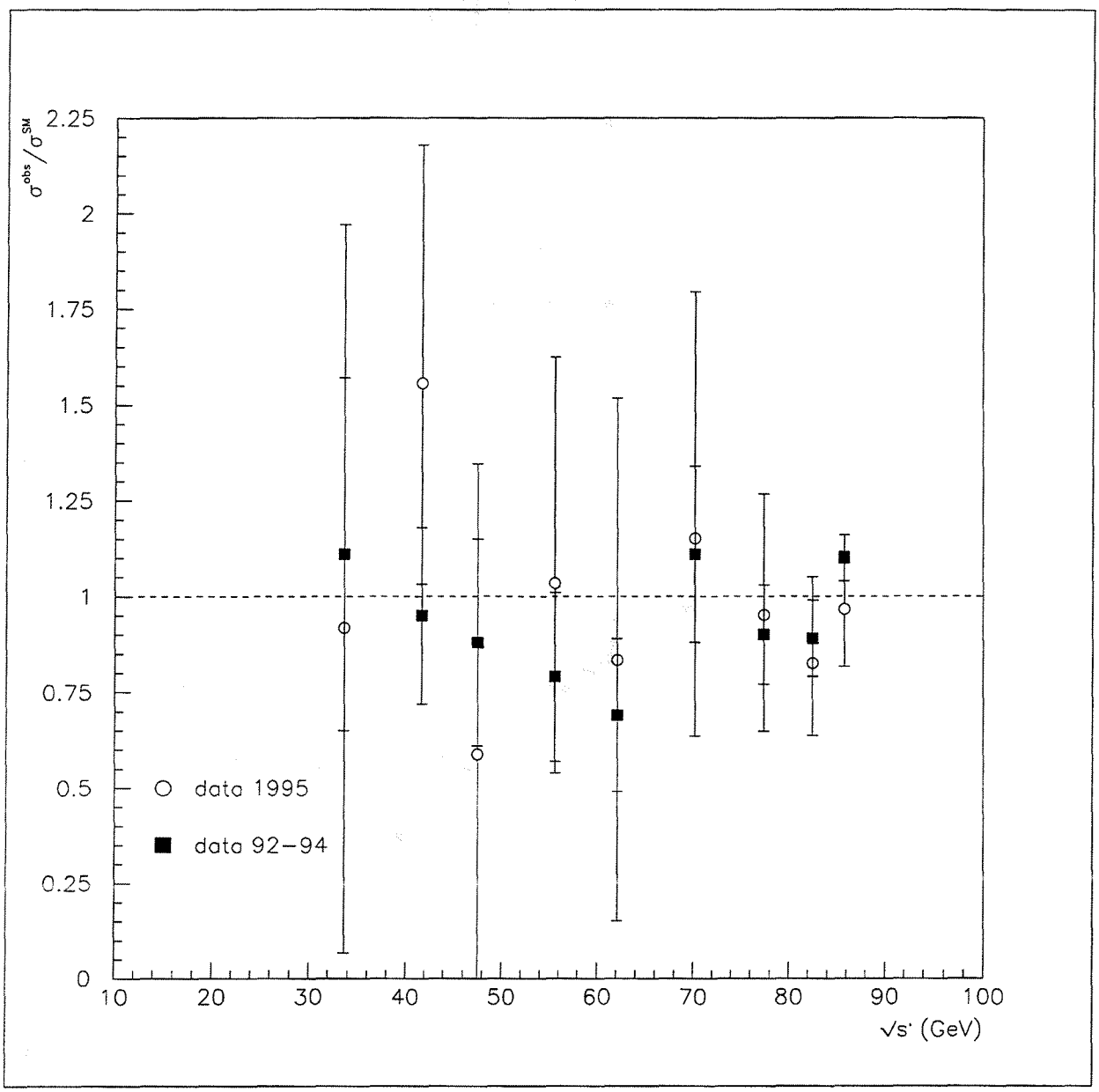

Figure 15: Ratio of measured to SM Improved Born $\mu^+\mu^-$ cross-section as a function of the effective annihilation energy.

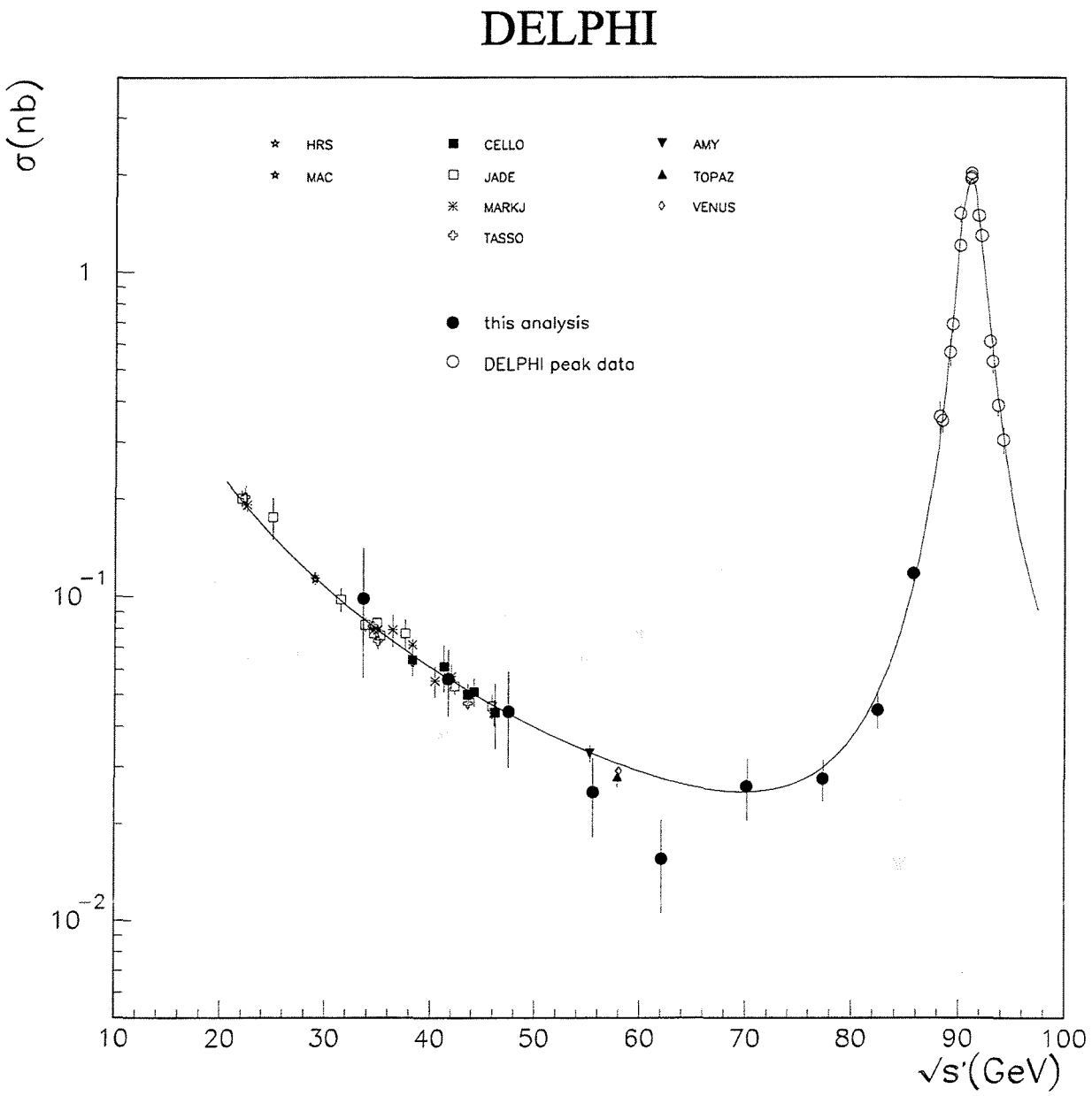

Figure 16: Improved Born $\mu^+\mu^-$ cross-sections measured in the analysis of DELPHI data from 1992 to 1995 (*black circles*), at the Z^0 peak (*open circles*), and at PEP, PETRA and TRISTAN. The *solid line* shows the SM prediction.

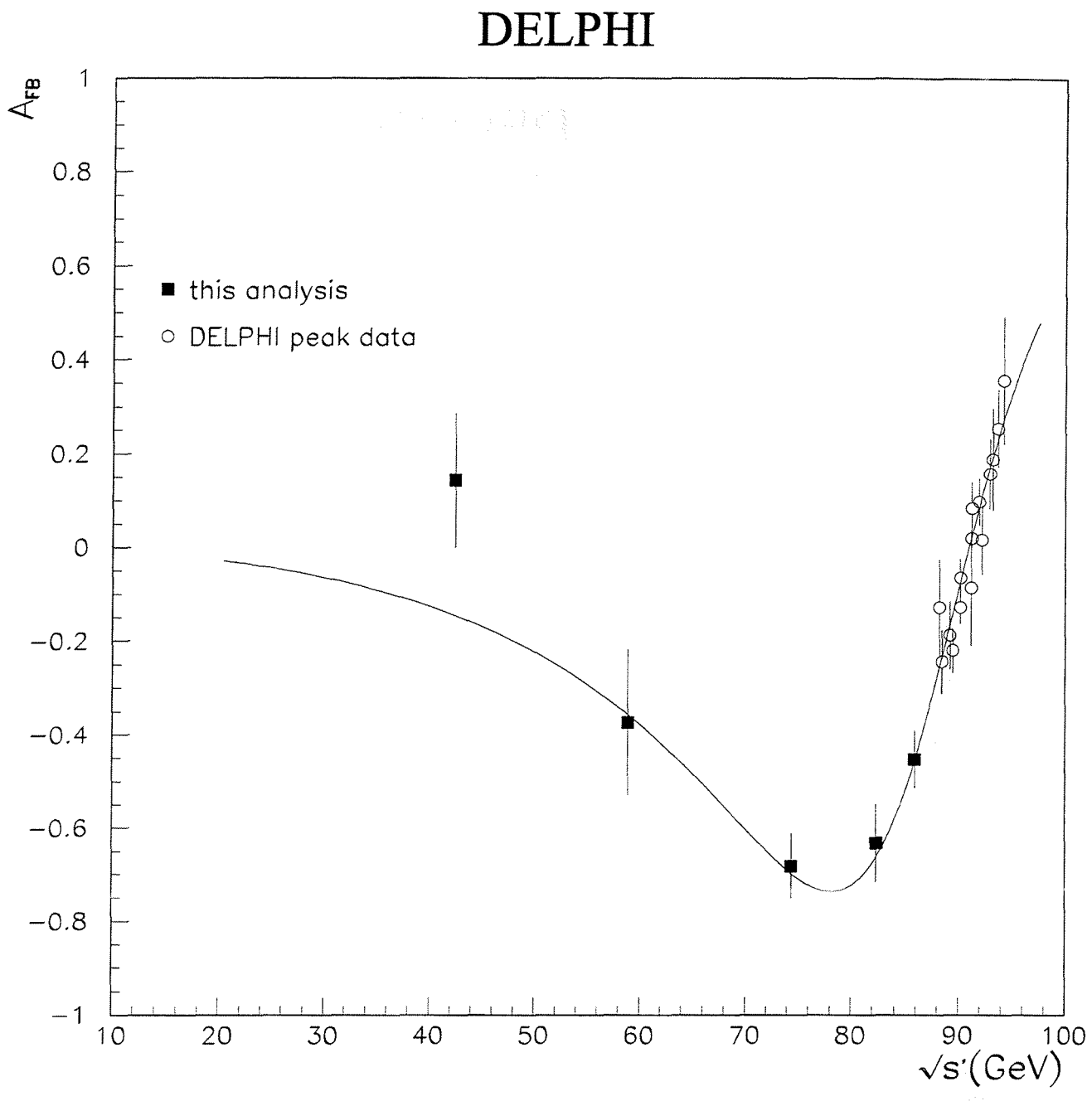

Figure 17: Improved Born $\mu^+\mu^-$ asymmetry as a function of the effective annihilation energy. The *black squares* show the measurements made by DELPHI below 87 GeV, using the likelihood fit method described in the text. The *open circles* show the measurements made by DELPHI at the Z^0 peak. The *solid line* shows the SM prediction.

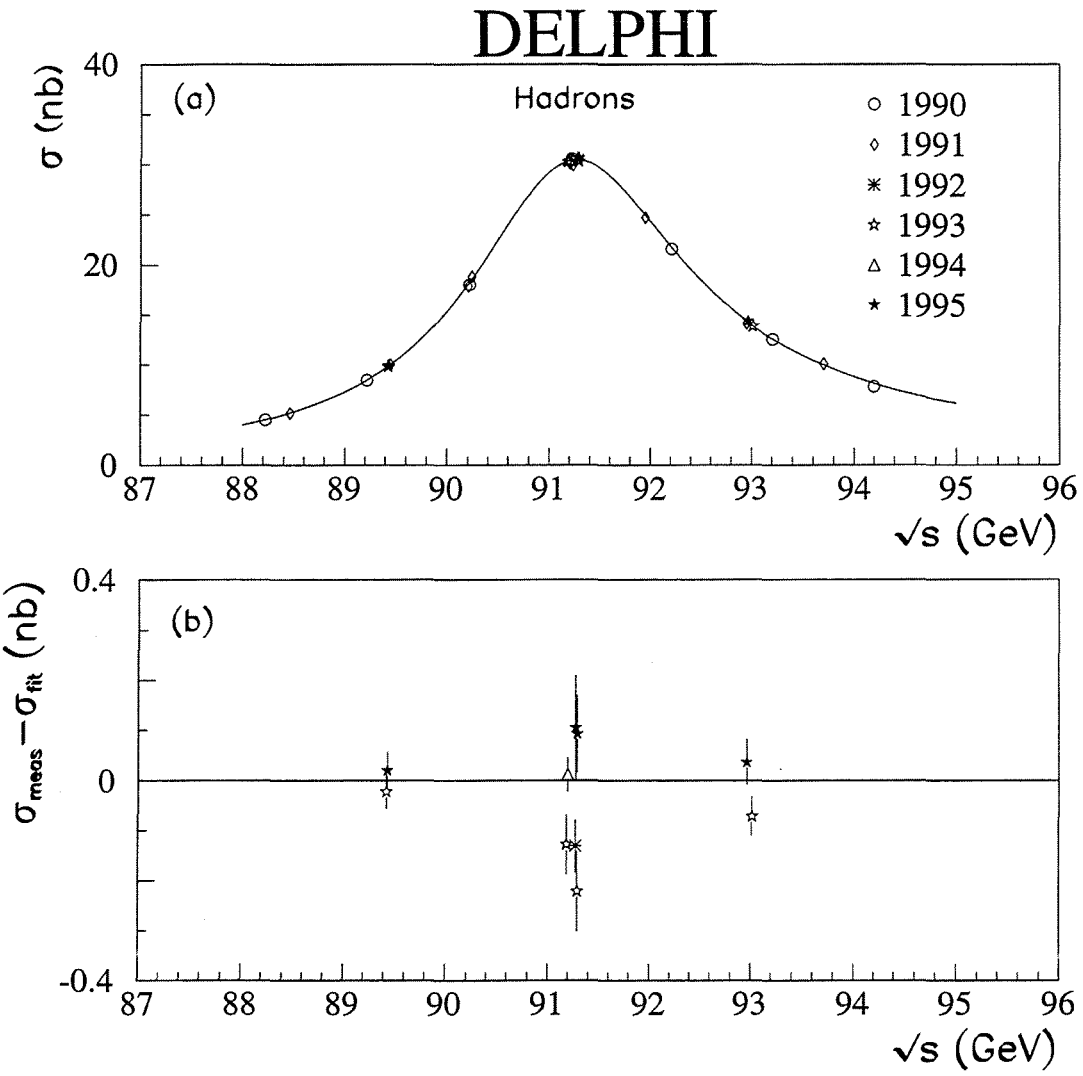

Figure 18: Hadronic cross-sections from 1990, 1991, 1992, 1993, 1994 and 1995 data. The errors shown are statistical only. In (a) the data are shown together with a curve representing the result of the 5-parameter fit described in Section 10. Plot (b) shows the difference of the measurements from the best fit values; for clarity only the data from 1992, 1993, 1994 and 1995 are shown.

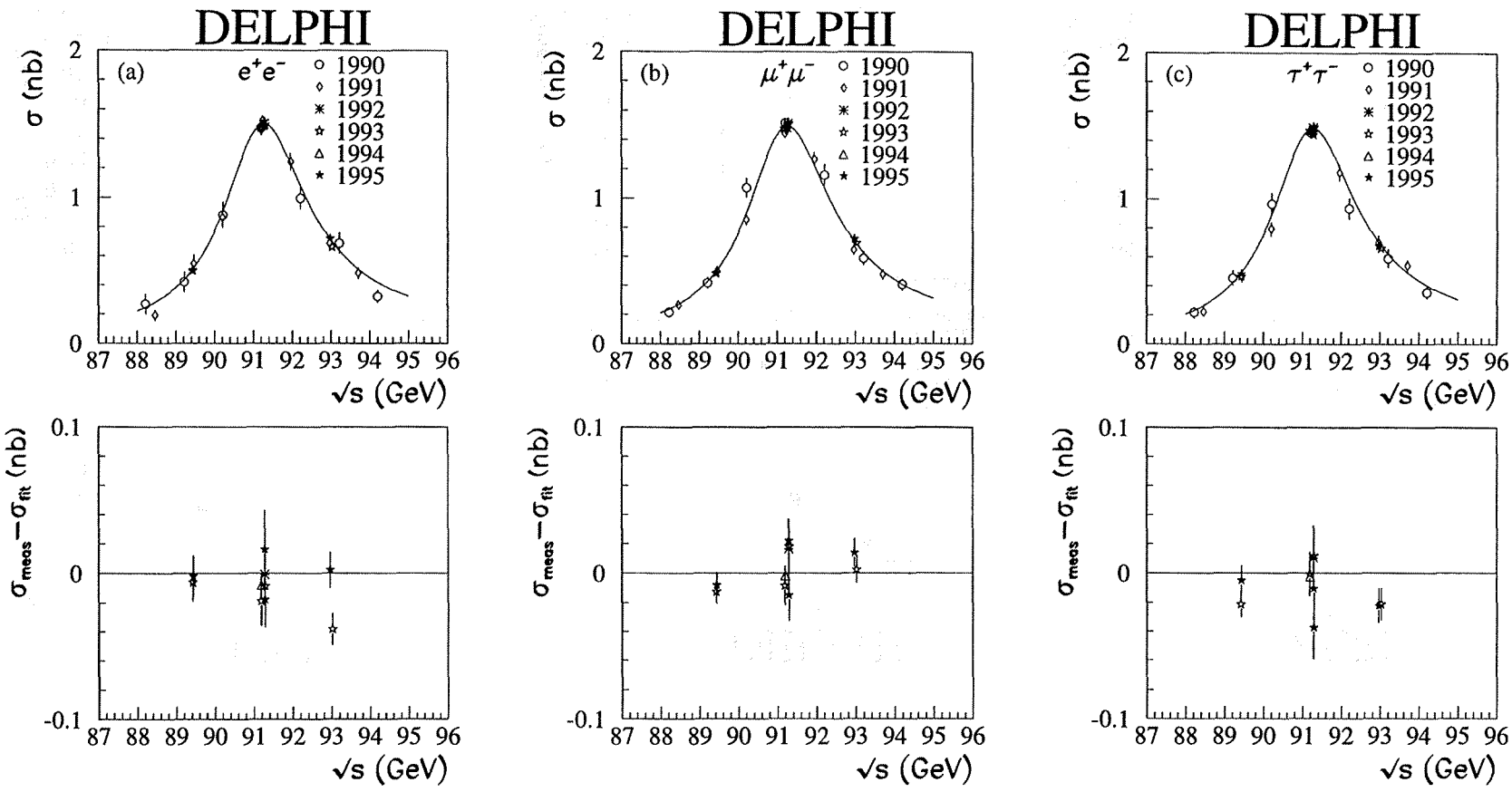

Figure 19: Cross-sections in the (a) e^+e^-, (b) $\mu^+\mu^-$ and (c) $\tau^+\tau^-$ channels. The cross-sections are extrapolated to the full solid angle and corrected for the acollinearity and momentum cuts. Only statistical errors are shown. The lower plots show the differences between the measured points and the best fit values; for clarity only the 1992, 1993, 1994 and 1995 data are shown. The curves represent the results of the 5-parameter fit described in Section 10.

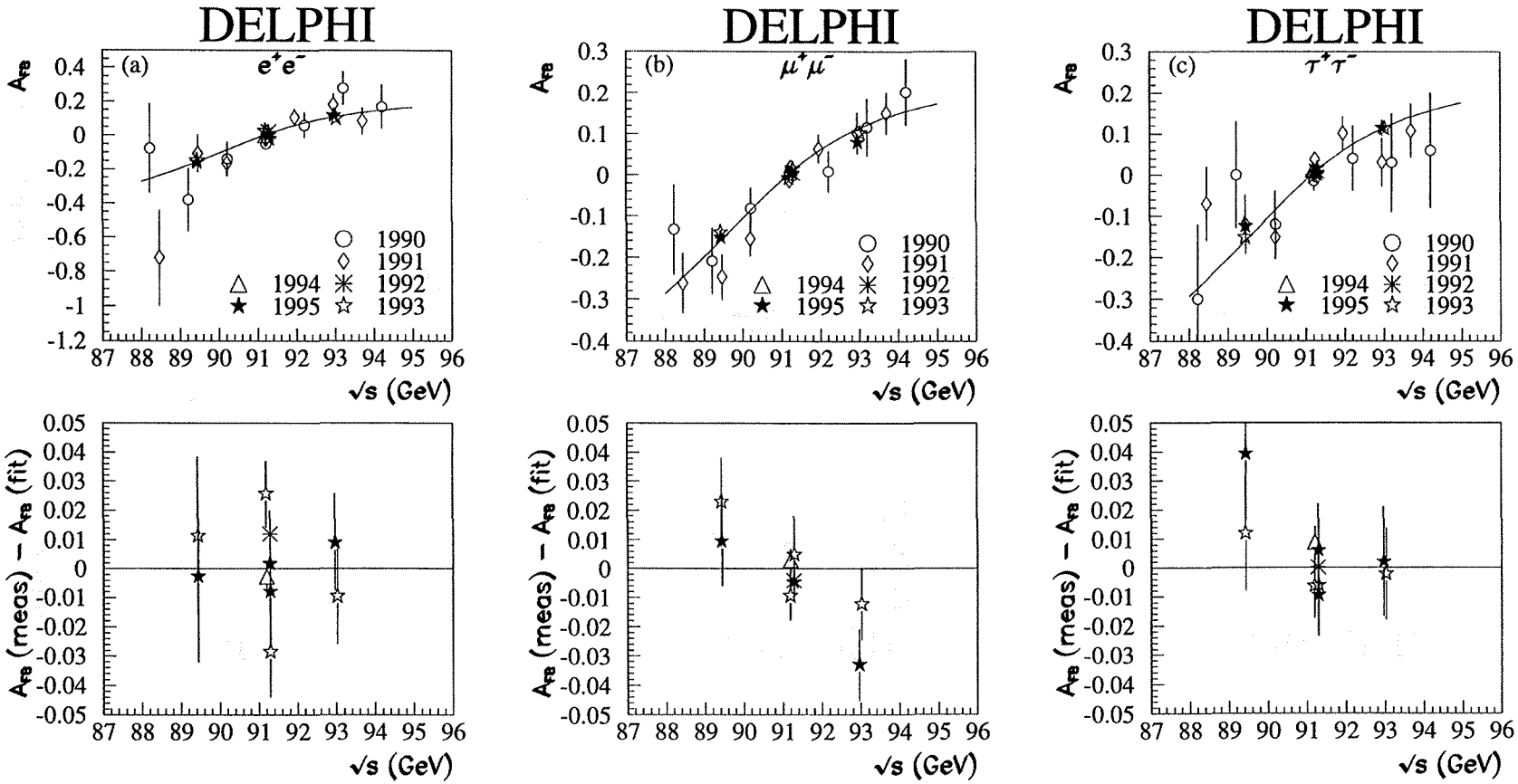

Figure 20: Forward–backward asymmetries in the (a) e^+e^-, (b) $\mu^+\mu^-$ and (c) $\tau^+\tau^-$ channels. The asymmetries are extrapolated to the full solid angle and corrected for the acollinearity and momentum cuts. The lower plots show the differences between the measured points and the best fit values; for clarity only the 1992, 1993, 1994 and 1995 data are shown. The curves represent the results of the 5–parameter fit described in Section 10.